Earth-Science Reviews 277 (2026) 105447

Contents lists available at ScienceDirect

Earth-Science Reviews

journal homepage: www.elsevier.com/locate/earscirev

Bedding-parallel fractures in shale: Formation mechanisms, geological significance, and implications for hydrocarbon accumulation—A review☆

Shu Jiang [a,b,c,*], Huanquan Sun [d], Jichao Fang [d], Hanyong Bao [e], Zhiguo Shu [e], Jiqing Li [e], Yiwen Ju [f]

[a] State Key Laboratory of Petroleum Resources and Engineering, College of Geosciences, China University of Petroleum, Beijing 102249, China
[b] Stake Key Laboratory of Deep Geothermal Resources, China University of Geosciences, Wuhan 430074, China
[c] Key Laboratory of Tectonics and Petroleum Resources, Ministry of Education and School of Earth Resources, China University of Geosciences, Wuhan 430074, China
[d] Stake Key Laboratory of Deep Geothermal Resources, Sinopec, Beijing 100728, China
[e] Jianghan Oilfield Company, Sinopec, Qianjiang 433124, China
[f] State Key Laboratory of Earth System Numerical Modeling and Application, College of Earth and Planetary Sciences, University of Chinese Academy of Sciences, Beijing, 101408, China

ARTICLE INFO

Keywords:
Bedding-parallel fracture
Fracture genesis
Filling cement geochemistry
Mechanical formation
Hydrocarbon accumulation
Shale reservoir

ABSTRACT

Shale commonly contains bedding-parallel fractures (BPFs) as a result of its well-laminated structure. There is great diversity in the type and origin of BPFs, yet a comprehensive synthesis of such fractures is lacking. This review consolidates current understanding of development and diagnostic features of BPFs in shale by integrating multiscale structural observations, fracture cement compositions and formation processes with advances in petrography, fluid inclusion analysis, isotope geochemistry, and fracture geochronology. The role of BPFs in hydrocarbon accumulation is explored through diffusion analysis and analog modeling of hydrocarbon migration.

Shale BPFs can be classified into four principal genetic types: hydrocarbon fluids overpressure, tectonic, diagenetic, and unloading BPFs. Hydrocarbon-generation BPFs are generated by fluid-over pressure during hydrocarbon maturation in relatively closed systems and are characterized by the coexistence of hydrocarbon and aqueous inclusions, similar geochemical and isotopic signatures to those of the host shale, and ages consistent with the timing of hydrocarbon generation. Tectonic BPFs are formed through reactivation of bedding weaknesses under regional compression or shear, commonly involving open-system basin or hydrothermal fluids. Diagnostic evidence of hydrothermal input includes homogenization temperatures for fluid inclusions that are higher than ambient stratigraphic conditions, positive Eu anomalies, isotopic compositions resembling those of regional magmatic–hydrothermal systems, and ages that coincide with the timing of magmatic activity. Where tectonic deformation occurs in the absence of magmatism, BPF cements inherit the characteristics of the host shale or adjacent stratigraphic fluids in an open system. Diagenetic BPFs are driven by differential compaction and mineralogical shrinkage during early burial or early diagenesis stage within a relatively closed system and are generally unaffected by external hydrothermal or deep fluids; consequently, they have similar fluid inclusions and geochemical signatures to the host shale. Unloading BPFs form during late-stage uplift and erosion, typically cemented by low-temperature meteoric or shallow formation waters. BPFs can extend laterally over large distances and have high imbibition efficiencies, forming essential pathways for oil and gas migration in shale. Shale with well-developed BPFs has a high permeability, and the coupling of BPFs with matrix pores during hydrocarbon charging creates interconnected pore–fracture systems that facilitate long-distance lateral transport. This process not only lowers the threshold pressure required for hydrocarbon accumulation, but also substantially improves reservoir permeability and fluid conductivity, ensuring the efficient enrichment and sustained production of the reservoir.

This review highlights the genetic-diagnostic framework for interpreting structural complexity and diverse origins of BPFs across diverse basins, as well as the variable geochemistry and inclusion characteristics of fracture cements, which provides a conceptual basis for improved prediction of fracture-controlled hydrocarbon

☆ This article is part of a Special issue entitled: 'ZhangLaubachFracture' published in Earth-Science Reviews.

* Corresponding author at: College of Geosciences, China University of Petroleum, Beijing 102249, China
E-mail address: sjiang@cup.edu.cn (S. Jiang).

https://doi.org/10.1016/j.earscirev.2026.105447
Received 20 October 2025; Received in revised form 17 February 2026; Accepted 28 February 2026
Available online 7 March 2026

enrichment and development performance. Overall, BPFs reduce hydrocarbon charging thresholds and enhance permeability, and play a pivotal role in shale hydrocarbon accumulation and long-term productivity.

Contents

1. Introduction

Recent advances in unconventional petroleum resources, particularly shale oil and gas, have reshaped the global energy landscape (Zou et al., 2013; Aguilera, 2014; Ma et al., 2021). Natural fractures are pivotal for hydrocarbon exploration and production (Gale et al., 2014; Torres et al., 2021; Laubach et al., 2023; Gong et al., 2025; Su et al., 2025). Furthermore, the same fracture systems are increasingly recognized as critical controls in related fields: they serve as preferential injection conduits or potential leakage pathways in CO_2 geological storage, and they define the effective permeability of enhanced geothermal systems (Mohammad et al., 2018). Although these fractures can substantially increase reservoir permeability and storage, their effects on hydrocarbon accumulation and preservation depend strongly on the type of fracture (Forstner and Laubach, 2022; Wang et al., 2023). High-angle fractures provide predominantly vertical migration paths from depth, whereas low-angle fractures enable lateral transport, although when isolated they can fail to connect bounding strata and thus act as efficient traps that help maintain seal integrity (Zhang et al., 2025). Scale further modulates outcomes: micro- to small-scale fractures facilitate proppant placement and increase the stimulated volume, whereas larger fractures can divert fluids, distort fracture networks, and even cause stimulation failure (Edirisinghe and Perera, 2024; Lv et al., 2025). Together, these insights underscore the need for robust identification and prediction of fracture types across scales (Nishiwaki and Lin, 2019; Gupta et al., 2020; Gale et al., 2022; Sun et al., 2025a, 2025b).

Bedding-parallel fractures (BPFs) are common in shale reservoirs and warrant detailed study (Sanderson et al., 2024; Lines et al., 2025). BPFs nucleate along laminations or mechanically weak partings, occur in planar, lenticular, or branching forms, and are commonly mineralized by calcite, quartz, or sulphate minerals (Liu et al., 2025; Wu et al., 2025b, 2025a). The lithology and depositional microfacies provide the material framework for the development of BPFs, and multiple mechanisms govern their initiation and growth, including tectonic compression (Hooker and Laubach, 2023); anomalous fluid overpressure (Gale et al., 2022; Lines et al., 2025); diagenetic processes, including compaction, pressure solution, and shrinkage (Laubach et al., 2010); and uplift and erosion (Peacock, 1997).

Shale typically contains a high density of BPFs with good lateral continuity, with BPFs preferentially tracking organic-rich laminae that lie in direct contact with the source rock, providing favorable loci for hydrocarbon storage and retention (Laubach et al., 2010; Li et al., 2025b, 2025a). The density, apertures, and connectivity of BPFs are the main controls on reservoir performance, and intervals enriched in BPFs commonly have elevated oil contents and higher production, suggesting that these intervals are key indicators of hydrocarbon enrichment (Zhang et al., 2025). Operationally, BPFs provide natural lateral pathways that guide volume fracturing, enhancing stimulation efficiency and production response. During treatment, BPFs may be reactivated by shear to form complex networks, but they can also induce stress shadowing, fracture deflection, or premature closure. The accurate delineation of their distribution and mechanical behavior is, therefore, essential for optimizing stimulation design and maximizing recovery.

Regional differences in BPFs are pronounced, and interpretations therefore vary accordingly. In North American shale plays, including the Bakken, Eagle Ford, and Marcellus plays, BPFs are pervasive and typically have shallow dips, high densities, and strong mechanical anisotropy. They can enhance reservoir performance markedly and influence hydraulic stimulation to a greater degree than steep fractures (Lee et al., 2015; Liu and Ostadhassan, 2017; Ferrill et al., 2022). In the Neuquén Basin in Argentina, BPFs in the Vaca Muerta Formation are far more abundant than their high-angle counterparts and are attributed mainly to diagenesis and tectonic activity. The common occurrence of hydrocarbon inclusions indicates that the BPFs formed under hydrocarbon-

induced overpressure, and they facilitated migration from source intervals to reservoirs (Mangenot et al., 2023; Zanella et al., 2024). In the Bowland and Cleveland basins in the UK, BPFs in the Bowland Shale are dominantly tectonic and provide key migration pathways that shape connectivity and accumulation (Imber et al., 2014; de Jonge-Anderson et al., 2021).

In the Sichuan Basin, BPFs are central to reservoir stimulation. In the Fuling area of the Wufeng–Longmaxi succession, the development of BPFs is strongly controlled by sedimentary laminations, proximity to fault zones, and the abundance of brittle minerals (e.g., quartz and biotite). Leveraging and modifying these BPFs during stimulation is critical to good reservoir performance (Li, 2022; Yan et al., 2022). In the Luzhou area, the depositional setting and diagenesis control BPF development. Interactions between natural and hydraulic fractures dictate the network geometry, with shallow lateral "fishbone" systems enhancing horizontal connectivity and focusing hydrocarbons into favorable compartments (Zhao et al., 2025). In the Ordos Basin, BPF occurrence in the Yanchang Formation is correlated with lamination intensity, total organic carbon, and pyrite content, although their role in hydrocarbon accumulation remains underexplored (Ding et al., 2024). In the Junggar Basin, the BPF intensity in the Lucaogou Formation increases with increasing brittle mineral and organic matter contents and decreases with increasing single-layer sand body thickness. These BPFs provide lateral pathways that improve shale-oil production (Liu et al., 2025; Song, 2019).

The quantitative characterization of BPFs is commonly based on integrated outcrop mapping, core description, petrography, conventional and image borehole logs, X-ray computed tomography (CT), and digital-rock analysis (Hooker et al., 2018; Hooker and Laubach, 2023; Meng et al., 2018; Afroogh et al., 2019; Bryndzia et al., 2024). To understand the origins of BPFs, researchers have combined multiscale observations with rock mechanical tests and numerical models, including triaxial fracturing experiments and finite or discrete element models, which reveal multistage genesis driven by diagenesis, tectonic stress, and subsequent diagenetic overprints (He and Duan, 2019; Chemenda, 2022; Laubach et al., 2023; Jin et al., 2024). Recent advances in high-precision geochemistry, fluid inclusion, and geochronology analyses of fracture cements (quartz, calcite, and dolomite) have pushed fracture studies toward a fully quantitative framework. Fluids regulate material transfer and energy redistribution in sedimentary basins and are sensitive indicators of tectonic, depositional, and diagenetic processes (Bjørlykke and Jahren, 2012; Laubach et al., 2019). In deep compressive settings, older fractures are commonly closed or mineral-filled, limiting fluid ingress (Gale et al., 2014; Gasparrini et al., 2014). Renewed tectonic stress can generate new fractures and reopen older ones, creating pathways for fluid flow and cement precipitation; the resulting cements record the chemistry of the precipitating fluids (Hooker et al., 2012; Agosta et al., 2016).

Geochemical tracers in cements can fingerprint fluid compositions, including the rare-earth elements (REEs) and C–O–Sr–Nd isotopic compositions, and comparisons with host shales and adjacent strata can constrain fluid sources (Bjørlykke and Jahren, 2012; Quandt et al., 2019; Zhang et al., 2024). Fluid inclusion homogenization temperatures and compositions record the pressure and temperature of cementation, which, when integrated with the burial history, constrains the timing of fracture opening and sealing (Hurai, 2010; Gasparrini et al., 2014). The absolute ages of the cements, estimated using U—Pb and Sm—Nd geochronology, can be used to further refine fracture timing (Roberts and Walker, 2016). Taken together, these approaches reveal fracture types and formation mechanisms and demonstrate how fractures govern hydrocarbon charge, retention, and overall reservoir performance.

Despite extensive work on BPFs in shale, pronounced regional variability persists in their occurrence and how they are characterized and understood. The approaches used, depth of study, and conclusions about the formation of BPFs and their impact on hydrocarbon accumulation vary widely, and a coherent synthesis is lacking. Here, we review the developmental characteristics and diagnostic criteria of BPFs, integrating multiscale observations with geophysical and machine-learning-assisted identification. We then examine four representative types (fluid overpressure, tectonic, diagenetic, and unloading BPFs), summarizing their formation mechanisms together with cement petrography, fluid inclusion signatures, chemical and isotopic geochemistry, and geochronology. Finally, we elucidate the mechanisms by which BPFs govern hydrocarbon charging, retention, and production. This synthesis provides an integrated framework for interpreting BPFs alongside the conceptual and quantitative basis needed for more efficient shale exploration and development. This review advances beyond existing syntheses by: (1) establishing a genetic-mechanism-driven classification that unifies fluid-dynamic origins (hydrocarbon-generation overpressure) with mechanical processes (tectonic, diagenetic, unloading), thereby resolving terminological inconsistencies in prior studies; (2) integrating multi-scale analytical workflows from nanoscale geochronology to basin-scale seismic anisotropy; and (3) quantifying the coupled fracture-matrix flow dynamics that govern hydrocarbon accumulation efficiency. Unlike previous reviews focusing on single mechanisms (e.g., tectonic fracturing) or specific basins, this framework provides universal diagnostic criteria applicable across diverse shale plays.

2. Methods for identifying BPFs in shale

2.1. Multiscale identification of BPFs

BPFs can be identified directly or through indirect inference. Direct approaches, including outcrop observation, core description, petrography, and scanning electron microscopy, form the foundation of BPF studies (Li et al., 2019; Zeng et al., 2022; Ding et al., 2023; Lu et al., 2024). These direct visualization methods are uniquely suited to establishing the geometric, textural, and paragenetic criteria that underpin genetic interpretation—particularly for distinguishing fibrous, blocky, and crack-seal fabrics diagnostic of overpressure, tectonic, and diagenetic origins (Su et al., 2022; Zhang et al., 2024, 2025).

Field observations show that BPFs occur preferentially in organic-rich shale intervals and are strongly lithologically controlled. They propagate along depositional laminae within individual beds or mechanically weak laminae or intersect the bedding at low angles, typically at dips of $<15^{\circ}$ in areas of stronger structural overprint, reflecting the combined influence of depositional and diagenetic processes with later deformation. BPFs commonly continue laterally for meters to tens of meters with nearly parallel or gently wavy traces, with spacings of a few to several tens of centimeters. Line densities range from ~2 to 15 m^{-1}, and BPFs are concentrated in organic-rich laminae, suggesting that the organic content and rock mechanical properties control their formation (Fig. 1a–c; Gasparrini et al., 2014). In outcrops, BPFs are filled predominantly by calcite, quartz, or gypsum, forming tabular to planar veins that are centimeters to decimeters wide (Rodrigues et al., 2009; Ryder et al., 2009, 2012; Ryder et al., 2008). Large veins commonly record multiple fluid episodes, with early bitumen or microcrystalline calcite overlain by fine- to medium-grain calcite, consistent with repeated stages of fracture opening and fluid flow (Fig. 1d–f). In structurally complex settings, horizontal compression coupled with fluid pressure produces more intricate geometries, including en-échelon arrays, offsets, and cross-cutting relationships (Fig. 1g–i). When mineral growth rates and fracture opening rates are mismatched, diverse fibrous fabrics develop in veins, including centripetal and antitaxial textures, and persistent stress may bend or offset crystals (Fig. 1j–n; Rodrigues et al., 2009; Gasparrini et al., 2014). Collectively, BPF's fracture morphology, spacing, and internal fabrics or vein textures are tightly controlled by the tectonic and geologic context, and the extent, geometry, fill sequence, and crystal growth style provide key field constraints on fracture genesis and the history of fluid activity.

At the core scale, BPFs in shale lie nearly parallel to laminations and

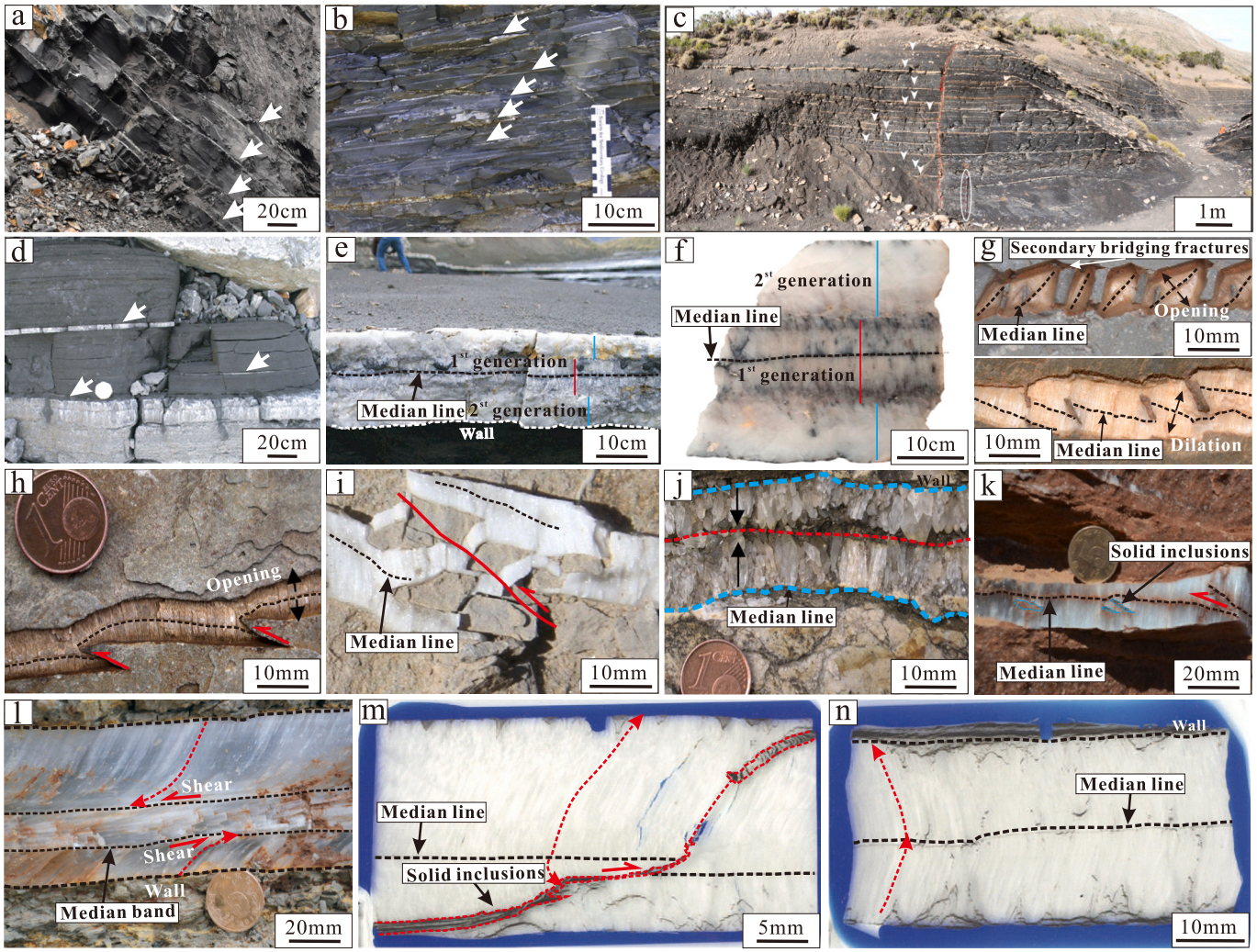

Fig. 1. Representative field photographs of BPFs in shale. (a) Organic-rich shale of the lower Silurian Longmaxi Formation with bedding-parallel slip surfaces cemented fully by calcite in the Wenchang Palace section, southern Sichuan Basin. The fractures extend laterally over long distances. (b) Photograph and line drawing of calcite-filled BPFs in the Barnett outcrop, San Saba County (Llano Uplift; Gasparrini et al., 2014). (c) "Beef"-rich intervals in the lower Huncal section (5–10 m). White arrows indicate beef, which is unevenly distributed (Ravier et al., 2020). (d) Bedding-parallel calcite "beef" layers of variable thickness in fissile shale in Dorset, Southwest England, UK. The calcite fibers are perpendicular or near-perpendicular to bedding, with widths of 0.5–55 cm (Cobbold et al., 2013). (e) Flat-lying multiphase gypsum-filled veins in Aptian evaporites, Benguela, Angola. The oldest gypsum vein contains black bitumen (photograph courtesy of Gabriel Castro, Petrobras; Cobbold et al., 2013). (f) Fibrous calcite "beef" in Cerro Mocho showing characteristic inner and outer zones and crosscutting small southwest-directed thrusts (Cruset et al., 2021). (g) Fibrous antitaxial en-échelon calcite veins with rotated brittle bridges embedded in the vein in Oppaminda Creek, Arkaroola, South Australia (Bons et al., 2012). (h) Antitaxial calcite vein with fibers growing outward from a median zone toward the wall rock in Oppaminda Creek, arranged en échelon (Bons et al., 2012). (i) Antitaxial fibrous gypsum vein in the Qingshuiying Formation, Ningnan Basin. The orientation of the fibers changes in the bend at the vein tip (Zhao and Li, 2022). (j) Syntaxial calcite vein with crystals growing from the wall rock toward the vein center in Biure, Spain (Bons et al., 2012). (k) Fibrous antitaxial gypsum vein in the Qingshuiying Formation, Ningnan Basin, showing asymmetric competitive growth. The median growth line is offset by shear (Zhao and Li, 2022). (l) Fibrous antitaxial gypsum vein with a distinct median zone and fibers along both margins bent by extensional shear in the Qingshuiying Formation, Ningnan Basin (Zhao and Li, 2022). (m) Fibrous bedding-parallel calcite vein with a sheared median line, small thrust faults, and markedly curved crystals in the Vaca Muerta Formation, Arroyo Mulichinco (Wang and Gale, 2023). (n) Symmetric antitaxial fibrous calcite vein with conspicuously curved crystal faces in the Vaca Muerta Formation, Arroyo Mulichinco (Wang and Gale, 2023).

occur as continuous linear or tabular veins and as discontinuous lenses. They commonly bend, bifurcate or taper along laminae, with dips of generally <10° (Fig. 2a–c). Most are filled with calcite, quartz, pyrite, or bitumen, and many show evidence of multiple cementation stages, with the mineralogy of the fill varying between basins in response to different fluid histories (Fig. 2c). Vertically, fracture occurrence is strongly heterogeneous and concentrated where the laminae are enriched in organic matter or mechanically weak (Fig. 2d, e). Fracture intensity is positively correlated with total organic carbon and pyrite contents, and is higher in siliceous laminae. Thinner laminae and higher contents of rigid volcanic fragments or organic matter facilitate episodic splitting along weak planes due to overpressure, resulting in higher fracture densities and larger apertures (Zeng et al., 2022). In structurally complex settings, BPFs form stepwise en-échelon arrays (Fig. 2f, g), are cut by later high-angle BPFs (Fig. 2h), or branch into pincer-like terminations (Fig. 2i), reflecting the complicated tectonic setting. Under repeated stress cycles, tectonic BPFs undergo multiple opening and sealing events that generate thick calcite veins (Fig. 2j). This crack–seal process starts when horizontal stresses create the first openings. After partial stress release, pressure solution in the host layer generates fluid that migrates into lower-pressure fractures and the vein fills are precipitated. Renewed stress accumulation reopens the fractures along vein walls, and new crystals grow outward from the earlier walls until sealing recurs (Ramsay, 1980). Repeated opening, sealing, and shear can result in

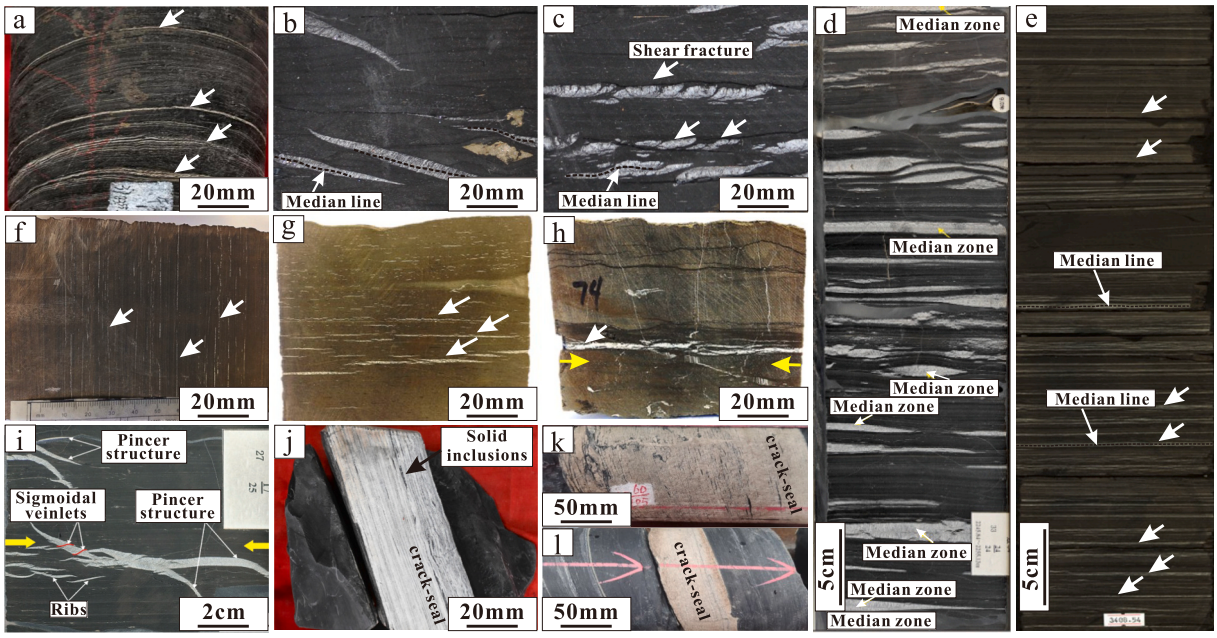

Fig. 2. Representative core photographs of BPFs in shale. (a) Organic-rich shale with BPFs that cut the entire core, from 3790.4 m depth in Well NX55, Paleogene Shahejie Member 3 (lower submember), Jiyang Depression, Bohai Bay Basin. (b) Veins with a median line at an oblique angle to both bedding and vein walls, from 3269 m depth in a core from the Jurassic Posidonienschiefer. Pyrite cement has a yellow hue, and veins occur in en-échelon arrays (Hooker et al., 2019). (c) Core face that is oblique to the veinlets and roughly parallel to the strike of the vein, from 2263 m depth in a core from the Jurassic Posidonienschiefer. Pyrite occurs at lower right. (d) Fibrous calcite veins with a markedly uneven vertical distribution and variable morphologies, from 2254.77 to 2255.13 m depth in Well X34 in the Upper Cretaceous Qingshankou Formation, northern Songliao Basin (Sun et al., 2023). (e) BPFs with fibrous calcite, predominantly horizontal tabular forms with interbedded calcite laminae, from 3407.54 to 3408.54 m depth in Well FY1 in the Shahejie Member 3 (lower submember), Jiyang Depression. (f) Dark gray shale with discontinuous BPFs in the Mahogany Zone of the Paleogene Green River Formation (Al Duhailan, 2014). (g) Yellow-brown mudstone and shale from the Green River Formation with discontinuous, stepped fibrous calcite veins (Duhailan, 2014). (h) Gray calcareous shale from the Upper Cretaceous Niobrara Formation with multiple BPFs in muddy bands. Younger high-angle to vertical shear fractures are constrained by older bedding-parallel sets. (i) Branching calcite vein with a pincer geometry, from 2202.23 m depth in Well X34. The ribs are aligned and the tips curl, and the vein is sheared into sigmoidal segments. (j) Thick bedding-parallel vein formed by repeated opening and sealing, from 4281.50 m depth in Well TY1, Wufeng–Longmaxi Formation, southern Sichuan Basin. The width of the fracture is 5 cm. (k) Calcite-filled fracture (18 cm wide) at 4281.50 m depth in Well TY1, Wufeng–Longmaxi Formation. (l) Calcite vein (4 cm wide) with basal calcareous laminae, from 4387.50 m depth in Well TY1, Wufeng–Longmaxi Formation. (For interpretation of the references to colour in this figure legend, the reader is referred to the web version of this article.)

bending of the vein, creating sutured seams and accommodating strain in the rock (Fig. 2k, l). Overall, core-scale BPFs are characterized by a low dip, high density, micron-scale apertures, substantial cement fill, and discontinuous lateral persistence, with development controlled by organic mineral assemblages and transient overpressure.

At the microscopic scale, BPFs in shale often occur as partially open, discontinuous microcracks localized along lamination interfaces or around rigid bioclastic grains (Fig. 3a, b). They are preferentially located in mechanically weak silty or bioclastic laminae, are short and prone to bifurcation and pinching, and have very small apertures, typically nanometers to micrometers in width. Apertures can vary by orders of magnitude along a single fracture, reaching several hundred micrometers at local maxima (Fig. 3c, d; Gale et al., 2007, 2014; Zeng et al., 2022). The residual open space serves as micro- to nanoscale flow pathways that increase the permeability. Early fractures are filled with calcite, quartz, gypsum, or bitumen, which often have a fibrous habit.

When the vein mineral is also a major constituent of the host rock, crystals commonly grow outward from wallrock grains to produce syntaxial veins. These veins result from rapid extension of the host shale, develop in fractures, and appear optically continuous with the wall rock. Unlike stretching veins, syntaxial veins have a single, stationary growth interface. If the growth interface is centered, minerals precipitate on both sides toward the median plane to form a symmetric syntaxial vein (Fig. 3e, f), and if located along one wall, growth is asymmetric (Fig. 3g, h). In contrast, antitaxial veins develop when the vein mineral is not a major phase in the host rock. In this case, fibers grow from a median zone toward the walls, with two contemporaneous growth fronts at the outer vein margins. The median commonly preserves wall-rock relics or early vein bands that formed during rapid initial growth (Hilgers and Urai, 2002; Bons, 2000; Bons and Montenari, 2005). The crystals in antitaxial veins are typically fibrous, bend along opening trajectories (Fig. 3i), and may show offset growth lines if horizontal shortening occurred during growth (Fig. 3j, k). Antitaxial veins are common in black mudstone and generally consist of calcite, although quartz and gypsum veins also occur (Fig. 3l, m; Elburg et al., 2002; Williams and Urai, 1989).

In addition to fibrous fabrics, bedding-parallel veins also exhibit crystal stretching, elongated blocky, and cone-in-cone textures. Stretching veins form by the episodic extension of preexisting grains, and crystals span the full vein width, with serrated boundaries and internal laminae parallel to the host shales recording repeated opening–sealing cycles (Fig. 3l). Blocky veins contain mosaics of equant and randomly oriented crystals. Similar textures may also result from the recrystallization of earlier veins (Bons, 2000). In elongate blocky veins, the crystals are moderately elongated (aspect ratios of ~10) with aligned long axes, reflecting competitive overgrowth by epitaxial extension from wallrock minerals or early nuclei with no new nucleation (Fig. 3m). Cone-in-cone structures consist of nested coaxial cones resembling a Russian doll motif (Fig. 3n). The cone apices have a consistent polarity, typically pointing stratigraphically upward.

To identify and characterize micro- to nanoscale BPFs more precisely, shale reservoir studies increasingly employ a suite of high-resolution analytical methods. The integrated use of argon-ion polishing, backscattered electron imaging (BSE), energy-dispersive

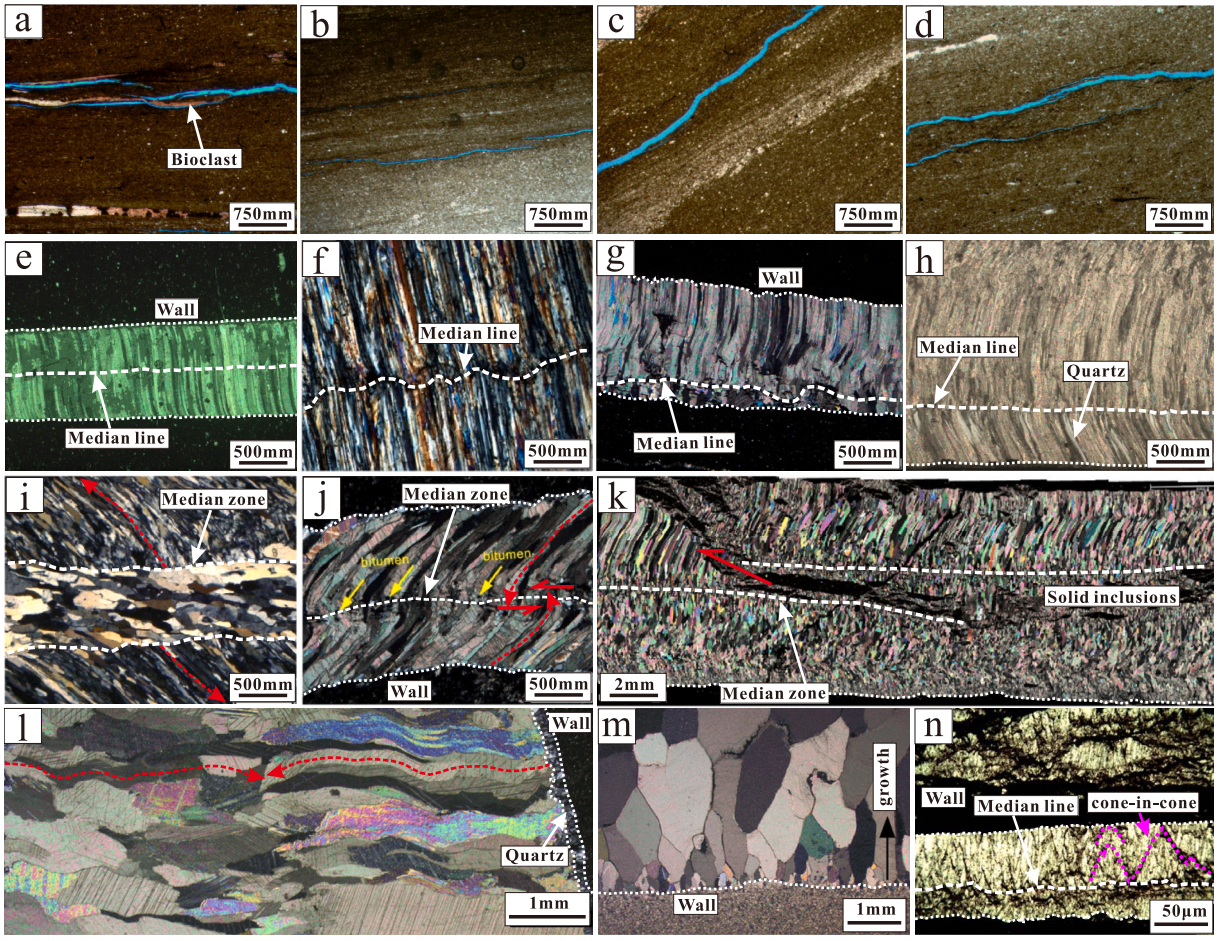

Fig. 3. Microscopic characteristics of BPFs. (a) Clay-rich shale with bioclastic debris containing a BPF that wraps around platy bioclasts, from 2235.62 m depth in Well FY3–2, Da'anzhai Member, Lower Jurrasic Ziliujing Formation, eastern Sichuan Basin. (b) Laminated muddy siltstone with discontinuous fractures along lamination boundaries, from 2237.12 m depth in Well FY3–2. (c) Laminated silty mudstone with fractures that track lamination interfaces continuously, from 2230.42 m depth in Well FY3–2. (d) Silty mudstone with two laterally continuous BPFs, from 2233.12 m depth in Well FY3–2. (e) Symmetric antitaxial fibrous calcite vein with fibers growing outward from a median zone, from 3065 m depth in Well YY6 in the Wufeng–Longmaxi Formation, southern Sichuan. (f) Brown muddy shale with an uncrystallized median zone in the Upper Paleogene Qingshuiying Formation, Ningnan Basin. Straight, smooth gypsum fibers indicate symmetric centripetal growth (Zhao et al., 2020). (g) Asymmetric antitaxial fibrous calcite vein with curved crystal faces, from 3377.18 m depth in Well YY54–1 in the Wufeng–Longmaxi Formation. (h) Asymmetric antitaxial fibrous calcite vein from 3586 m depth in Well DY6–1, in the Wufeng–Longmaxi Formation, showing two cementation stages: an early calcite and quartz stage followed by a later calcite-only stage. (i) Brown muddy shale from the Qingshuiying Formation, Ningnan Basin, with a median zone filled with blocky gypsum that grows preferentially parallel to the vein walls and is flanked by antitaxial fibrous gypsum on both sides (Zhao and Li, 2022). (j) Curved antitaxial fibrous calcite vein with multiple inclusion bands and solid bitumen in the median zone, from the lower Cambrian Donghe Formation in the frontal zone of the Dabashan thrust belt, northeastern Sichuan (Zhao and Li, 2022). (k) Gray-black shale with antitaxial fibrous calcite, from the Loncopué section of the Vaca Muerta Formation, Argentina. The median growth line is offset by shear, and small thrusts are present. (l) Photomicrographs of antitaxial fibrous calcite with coarse, curved fibers and a thin inward-growing quartz rim on vein margins, from Oppaminda Creek, Arkaroola, South Australia (Bons et al., 2012). (m) Syntaxial calcite vein from Pure, Spain, showing strong competitive growth in the propagation direction. (n) Organic-rich shale with an asymmetric, centripetal cone-in-cone calcite vein, from 3303.5 m depth in Well L67 in Shahejie Member 3, Jiyang Depression, Bohai Bay Basin (Bons et al., 2012). (For interpretation of the references to colour in this figure legend, the reader is referred to the web version of this article.)

spectroscopy (EDS), field-emission–scanning electron microscopy (FE–SEM), transmission electron microscopy (TEM), focused ion beam (FIB) milling, confocal laser scanning microscopy (CLSM), nuclear magnetic resonance (NMR), and three-dimensional nondestructive microfocus and nano-CT imaging enable fine-scale detection, compositional analysis, and quantitative evaluation of micro- to nanoscale BPFs (Buckley et al., 2008; Ding et al., 2013; Garum et al., 2020; Barker, 1990; Zhou et al., 2024). Together, these techniques substantially improve the clarity and accuracy of observations and advance our understanding of the genesis, spatial architecture, and flow capacity of BPFs.

At the micro-CT scale, BPFs have strong lateral continuity and relatively simple three-dimensional geometries, most commonly tabular or gentle undulatory forms (Fig. 4a–e). In structurally active domains, coeval high-angle fractures intersect and overprint these features to produce distorted composite networks (Fig. 4f). Propagation paths are strongly controlled by lithologic heterogeneities: dense mineral laminae, including calcareous or siliceous bands, and low-density layers rich in organic matter or clay act as mechanical weaknesses that guide extension, whereas rigid material, including pyrite nodules and calcareous concretions, impedes fracture growth and promotes tapering and termination (Fig. 4g–j). At the microscale, alignment to bedding and preferred orientations become more evident, underscoring the influence of primary depositional fabrics on failure.

A critical issue in CT-based fracture analysis is the reliable discrimination of natural BPFs from coring-induced horizontal fractures. The following diagnostic criteria are recommended: (1) Natural BPFs typically exhibit partial to complete mineral cementation (calcite, quartz, pyrite) observable at micro-CT resolution as higher-density linings or fillings; induced fractures lack cement and show clean, matching walls (Lai et al., 2022; Dze et al., 2026). (2) Natural BPFs often follow specific

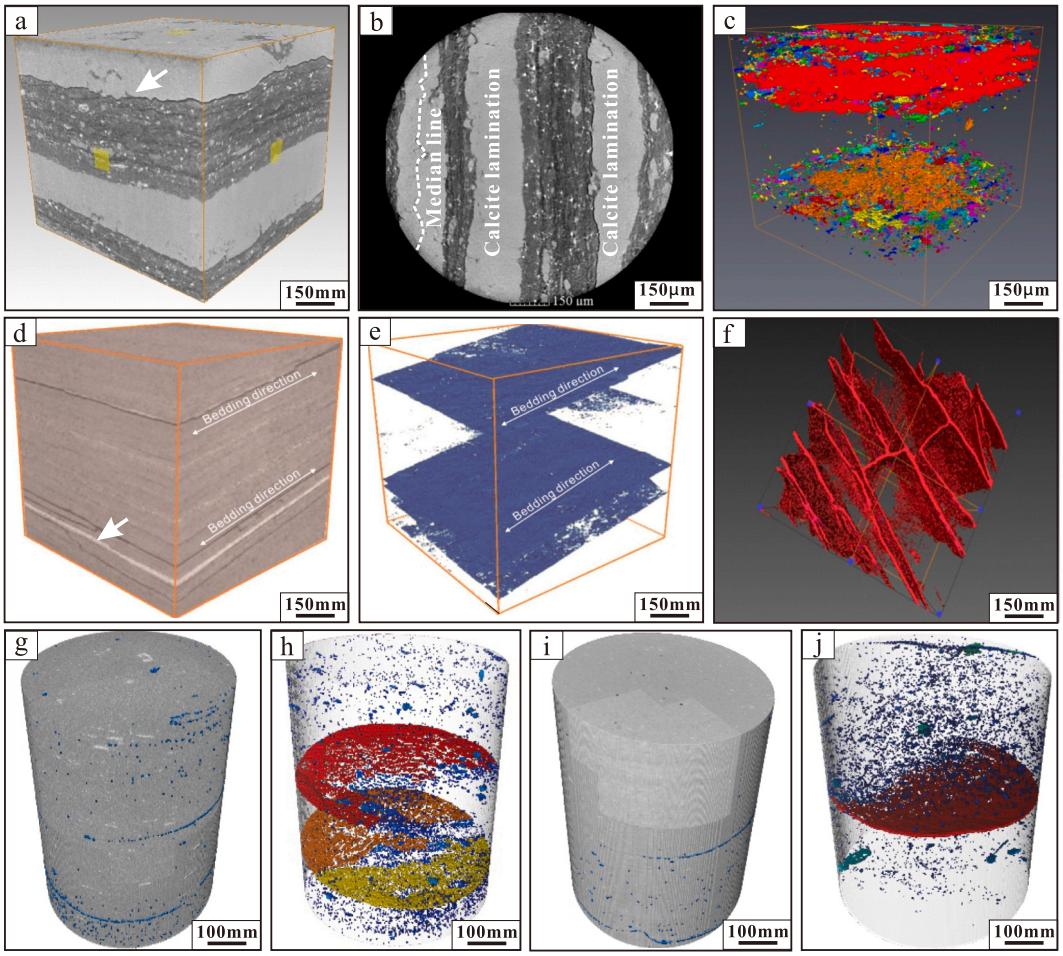

Fig. 4. Computed tomography (CT) characteristics of BPFs. (a) 3D CT image showing pronounced laminations, from 3297.24 m depth in Well NY1 in Shahejie Member 3 (lower submember), Jiyang Depression, Bohai Bay Basin. (b) Plan view CT image of alternating fibrous calcite veins and calcite laminae, from 3297.24 m depth in Well NY1. (c) Reconstructed 3D pore network model from 3297.24 m depth in Well NY1, showing markedly stronger along-bedding connectivity in fractures than in the matrix. (d) 3D CT image of multiple calcite-filled and unfilled BPFs, from 3798.3 m depth in Well W206 in the Wufeng–Longmaxi Formation, southern Sichuan Basin. (e) Digital rock reconstruction showing a long unfilled BPF with smooth walls and strong continuity, from 3798.3 m depth in Well W206. (f) 3D digital rock model showing unfilled BPFs that intersect high-angle to vertical shear fractures to form a three-dimensional network, from 3268.5 m depth in Well F120 in Shahejie Member 3, Jiyang Depression. (g) Segmented pore image produced from CT data, from 1879.56 m depth in Well YS6 in the Lianggaoshan Formation, northeastern Sichuan Basin (He et al., 2024). (h) Reconstructed pore network showing two bedding-parallel fractures, from 1879.56 m depth in Well YS6 (He et al., 2024). (i) Segmented pore image produced from CT data, from 1975.23 m depth in Well YS6 (He et al., 2024). (j) Unfilled bedding-parallel fracture with an aperture and connectivity that clearly exceed those of the surrounding matrix pores (He et al., 2024), from 1975.23 m depth in Well YS6.

laminae rich in organic matter or brittle minerals, and their apertures vary smoothly along strike; induced fractures cut indiscriminately across lithological boundaries and have uniform aperture (Rybalcenko, 2017). (3) In 3D reconstructions, natural BPFs display systematic terminations against rigid grains (pyrite nodules, carbonate concretions) and may be cross-cut by younger tectonic fractures; induced fractures propagate through grains without deflection (Fu et al., 2025). Thus, natural BPFs are part of a genetically related network, whereas induced fractures are isolated and randomly oriented. Integration of CT with SEM-EDS on companion samples can confirm the presence of authigenic cements, providing definitive evidence for a natural origin.

Quantitative analyses reveal substantial variability in aperture size, with widths of mostly 15–30 μm and tortuosity values of ~34.24–46.57, indicating sinuous flow paths. In two-dimensional sections and three-dimensional reconstructions, areal or volumetric porosity attributable to fractures can be as high as 40%, highlighting their central role in hydrocarbon storage. Critically, BPFs often link isolated macropores in the matrix and intersect other structural fractures to form an efficient flow network. This connectivity integrates otherwise discrete clusters of organic material-hosted pores, increases the absolute permeability, and provides efficient pathways for hydrocarbon accumulation and transport.

2.2. Geophysical identification of BPFs

Fractures can be identified indirectly from well logs and seismic data. Well logs play a central role in identifying and quantifying BPFs in shale, and are commonly divided into conventional and imaging techniques. Conventional well logs, including caliper, dual laterolog, micro-resistivity, acoustic transit time, spontaneous potential, and gamma-ray spectroscopy logs, exploit anomalies produced when fractures modify the pore structure, fluid distribution, and electrical properties of the rock. After mud invasion, open fractures typically fill with conductive mud and yield low-resistivity excursions, whereas closed or mineral-filled fractures often register as sharp high-resistivity peaks (Fig. S1). Microresistivity tools are especially sensitive, showing pronounced low-resistivity spikes at open fractures and the opposite response at closed fractures. Sonic logs exhibit reduced P- and S-wave velocities where wavefronts encounter fracture swarms oriented sub-perpendicular to the borehole. Density logs commonly display low-density anomalies over

fractures or vugs, and neutron–density crossplots show elevated apparent porosity where fractures are abundant (Nelson et al., 2000; Lai et al., 2018a, 2018b). In summary, BPFs are characterized on conventional logs by low resistivity, low density, slower acoustic velocities, and higher neutron and density porosities (Fig. S1). However, the characteristic "low resistivity, low density, slow sonic" signature applies strictly to effective bedding-parallel fractures that remain hydraulically conductive; sealed fractures exhibit the opposite or no clear anomalies. This distinction must be respected to avoid misinterpretation in fracture characterization (Laongsakul and Dürrast, 2011). The resolution of well logs is limited, however, and responses depend on mud properties, the electrical behavior of the formation, and borehole conditions. Small or fully closed BPFs may be weakly expressed, reducing the accuracy of interpretations (Laongsakul and Dürrast, 2011). Borehole image logs provide the highest resolution for orienting individual filled or open fractures and quantifying their aperture and density; seismic methods, especially azimuthal anisotropy and frequency-dependent attributes, are indispensable for mapping regional-scale fracture corridors where BPFs occur as dense swarms below seismic resolution (Lai et al., 2022).

In contrast, borehole images provide higher precision and resolution for BPF characterization and are an effective complement to conventional logs. Resistivity images are two-dimensional wall images acquired using electrode arrays, and fracture geometry can be seen directly. BPFs typically appear as continuous parallel anomalies, due to the differences in conductivity between conductive open mud-filled fractures and resistive cemented or closed fractures. Reflections and scattering produce alternating bright and dark bands at fracture locations in acoustic images, which delineate the geometry and spatial distribution of the fractures (Gou et al., 2020). Imaging tools can resolve millimeter-scale features, and the dip, azimuth, length, line density, and connectivity of fractures can be extracted with high reliability, providing essential inputs for quantitative description and mechanical modeling. This approach is comparatively costly, however, and performance is sensitive to borehole conditions. Enlarged holes, wall collapse, and heavy mud caking degrade image quality and reduce the accuracy of interpretations.

A common challenge in resistivity image interpretation is distinguishing calcite-filled BPFs from primary calcite-rich laminae. Several diagnostic features aid this distinction. First, fracture-fill calcite usually appears as continuous or segmented high-resistivity bands with sharply defined, often planar boundaries; sedimentary calcite laminae exhibit gradational contacts and diffuse internal textures (Fang et al., 2016). Second, In dynamically normalized images, filled fractures often display a central low-resistivity streak (residual micro-porosity or fluid inclusion bands) not seen in pure laminae (Wang et al., 2025). Third, when multiple image logs are available in the same well, filled BPFs show consistent dip azimuth parallel to regional stress indicators, whereas sedimentary laminae follow depositional dip (Wu et al., 2025b, 2025a). While these diagnostic criteria provide a robust framework for differentiation, their practical application remains contingent upon image resolution, borehole conditions, and the degree of diagenetic overprint—factors that continue to motivate ongoing methodological refinement and the integration of emerging high-definition logging technologies.

In summary, conventional logs are economic, rapid, and have broad applicability, but their ability to resolve fine details is limited. Imaging logs have high resolution, providing intuitive visualization and quantitative measurements, making them central to the identification and quantitative description of BPFs.

Seismic methods can be used to infer fracture distributions from three-dimensional wave propagation. Discontinuity indicators, including copolarization coefficients, curvature, fault likelihood, and surface tracking, delineate stratigraphic breaks that may host fractures. BPFs in shale are thin, shallowly dipping, laterally persistent bundles with small individual apertures and variable cementation, which yield weak responses to conventional seismic methods based on fault divergence or macroscopic reflector breaks (Ba et al., 2017; Guo and Gurevich, 2020; Gou et al., 2020). Consequently, seismic methods are most effective at the regional scale for detecting thick fracture intervals, and resolving BPFs generally requires high-quality 3D data. With a typical vertical resolution of at least ~10 m, conventional surveys cannot capture micron- to millimeter-scale features and primarily image zones of high fracture intensity. Standard prestack attributes are also insensitive to BPF sets and often lack clear azimuthal signatures. Three approaches have proven useful for addressing weak reflections and weak azimuths in the Changning–Weiyuan, Barnett, Marcellus, and Vaca Muerta basins, as follows. (1) Azimuthal prestack inversion (AVOaz) exploits elliptical variations in P-wave or normal moveout velocities with azimuth to predict the orientation and density of BPFs (Shang et al., 2021). (2) Frequency-dependent anisotropy and dispersion due to coupling between laminae, microfractures, and wavelengths can be used to map millimeter-scale fracture swarms, as shown in the Longmaxi and Barnett basins (Delle Piane et al., 2014; Gou et al., 2020). (3) High-resolution volumetric attributes, including curvature, coherence, and spectral-decomposition attenuation gradients can reveal banded low-coherence or high-curvature anomalies parallel to bedding, and enabled the delineation of fracture-rich corridors in the Marcellus Basin and in key production areas of the Sichuan Basin (Zhang et al., 2024; Fan et al., 2024b; Liu et al., 2024b,a). Despite these advances, performance is constrained by the cost of wide-azimuth acquisition, limited bandwidth, attribute non-uniqueness, and sparse calibration wells (Niu et al., 2024). Future workflows should integrate azimuthal prestack anisotropy, frequency-dependent anisotropy, and target volumetric attributes, and use cross-validation to improve the predictive accuracy for BPFs.

2.3. AI-based identification of BPFs

Identifying BPFs is pivotal for the efficient development of shale petroleum resources, yet manual interpretation is labor intensive and often inconsistent. Recent studies have applied artificial intelligence to well logs and core images, enabling automated detection and classification. Supervised and self-supervised learning pipelines built on convolutional neural networks, U-Net-like segmentation, and transformer backbones, together with classical machine-learning approaches, including support vector-machine and random-forest approaches, deliver markedly higher throughput and accuracy than conventional workflows. Deployed at scale, these models can standardize interpretation, reduce bias, and provide reproducible fracture maps that directly inform stimulation design and production forecasts. AI-based workflows, particularly deep learning segmentation of core photos, CT volumes, and image logs, excel at high-throughput, reproducible detection of subtle, small-aperture microfractures that are easily overlooked by human analysts, and are increasingly capable of distinguishing fracture types from textural and contextual features.

Traditional machine-learning approaches typically classify or regress fractures from log curves or derived attributes. Common models include support vector machines (SVMs), decision trees and random forests (RFs), artificial neural networks (ANNs), multilayer perceptrons (MLPs), and extreme learning machines (ELMs) (Deng et al., 2023; Dong et al., 2023; Ismail et al., 2023). SVMs separate fractured intervals from unfractured intervals by locating an optimal hyperplane in high-dimensional feature space. Decision trees partition log parameters using thresholds to distinguish fractured from intact sections, and RF ensembles improve robustness through majority voting (Lai et al., 2021; Ismail et al., 2023). ANNs learn fracture-relevant features via multilayer nonlinear mapping. These methods generally require feature engineering or dimensionality reduction, use numerical log data (e.g., resistivity, acoustic slowness, and density) as inputs, and, after training, yield discriminative predictors of BPFs or other fracture types.

Illustrative applications include the fracture signature function (FSF) derived solely from conventional well logs, which, coupled with a feedforward neural network, identifies natural fractures in shale without

FMIs or cores and performs well under class imbalance (Ismail et al., 2023). Deng et al. (2023) combined conventional and high-resolution logs and used a particle swarm-optimized ELM to improve the identification of thin interbeds, achieving 10%–30% higher accuracy than baseline methods. Azizi and Reza (2021) combined lithology and image logs from eight wells, trained decision trees, RFs, SVMs, and deep learning classifiers, and integrated outputs through ordered weighted averaging to increase detection accuracy. Overall, classical ML models are relatively simple, fast to train, and effective for small to medium datasets. They depend on hand-crafted features, have limited capacity to encode complex spatial contexts, assume some prior stationarity when generalizing to new data, and can be sensitive to hyperparameter choices (Lai et al., 2021).

Deep learning enables end-to-end feature learning and can ingest raw log curves, images, and seismic attributes. Representative architectures include convolutional neural networks (CNNs), recurrent neural networks (RNNs) such as long short-term memory (LSTM), transformer models (transformer and DETR), and object detectors such as YOLO and Faster R-CNN. CNNs excel on images, extracting spatial features from CT scans, core photographs, and borehole images and multilog data converted to images to delineate bedding orientation and fracture traces (Wu et al., 2024). RNNs capture sequential dependencies in depth-ordered logs, allowing the detection of fracture-induced anomalies. Object detectors, a computer vision technique, can localize and classify targets after log panels or resistivity images are cast as 2D inputs, enabling the automatic tagging of fractured intervals (Dong et al., 2023). DETR reframes detection as set prediction, producing N candidates that are matched to the ground truth via the Hungarian algorithm, which improves the recognition of thin features, including BPFs and fracture bands (Nasim et al., 2025).

The application of these methods is already showing clear gains. Ao et al. (2023) combined U-Net with attention to identify fractures in borehole images, recovering complex networks with high reliability. Dong et al. (2024) introduced FISY, which creates log images using a sliding window and applies YOLO-X and is more accurate than SMOTE with SVM or RF baselines. Nasim et al. (2025) developed GeoBFDT, a transformer-based framework that jointly identifies bedding and fractures on FMI and CMI resistivity images. Deep machine learning models learn discriminative patterns automatically, scale to large image datasets, and are more efficient and accurate than classical machine learning approaches. The remaining challenges include heterogeneous and sometimes unreliable labels, limited generalizability across basins, and

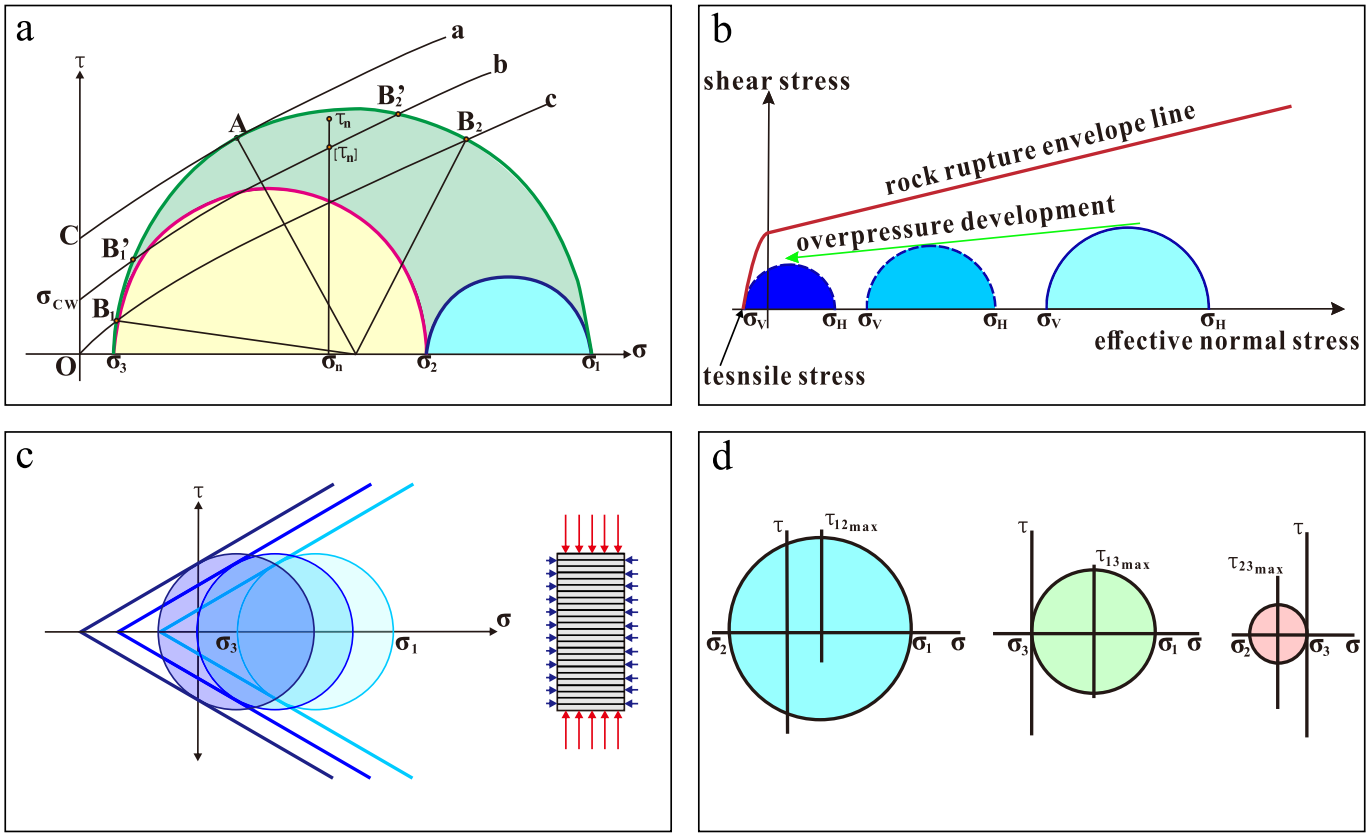

Fig. 5. (a) Triaxial Mohr diagram for the weak-plane reactivation criterion. Line 'a' represents the failure envelope for homogeneous intact rock, which is consistent with the Mohr–Coulomb criterion. Line 'b' denotes the weak-plane failure envelope, which is defined by the slope (μ_w) and intercept (C_w). Line 'c' is the fault reactivation line. (b) Mohr diagram for diagenetic BPFs. The contraction-stress envelope represents the tensile strength of the rock (σ_T, intercept on the horizontal axis). The circle is centered on the mean stress point, but diagenetic contraction reduces the effective minimum principal stress (σ_3), which may even become negative, shifting the circle leftward. The bedding plane orientations are indicated, and the contraction stress (σ_s) is expressed as the extension of the Mohr circle into the negative σ_n domain. When the circle is tangential to the tensile envelope in the $\sigma_n < 0$ region, tensile fractures are predicted to form. (c) Formation of hydrocarbon overpressure BPFs. The initial Mohr circle, centered at $[(\sigma_1 + \sigma_3)/2, 0]$, reflects a stress state dominated by compression. With increasing pore pressure (P_p), the effective stress decreases, and the circle shifts leftward to $[(\sigma'_1 + \sigma'_3)/2, 0]$, where $\sigma' = \sigma - P_p$, accompanied by a reduction in the radius. The failure envelope consists of the Griffith envelope in the negative σ_n domain and the Coulomb line in the positive σ_n domain. When elevated pore pressure drives σ'_3 negative, the Mohr circle becomes tangential to the Griffith envelope, marking the onset of tensile fracturing ($\sigma_n \approx -\sigma_T$). The diagram also shows the quantitative effect of an increase in pore pressure (ΔP_p) on fracture initiation. (d) Formation of unloading BPFs. Initially, the overburden stress (G) is high and the Mohr circle is centered in the positive σ_n domain. Following unloading, a reduction in G shifts the circle leftward with little change in the radius. The Griffith envelope is tangential to the Mohr circle when σ_n is negative, indicating the onset of tensile fracturing. The diagram shows the magnitude of unloading (ΔG) and residual stress (σ_r), illustrating the trajectory of the circle. Fracture development occurs when the circle becomes tangential to the envelope.

modest multimodal fusion. With continued advances in transformers, attention mechanisms, and self-supervision, coupled with larger high-quality training sets, AI-based fracture mapping is poised to achieve more accurate detection and quantitative characterization of shale reservoirs.

Nevertheless, several bottlenecks remain. First, Small-sample learning: high-quality labeled datasets (cores, image logs) are scarce and expensive to acquire, limiting supervised training (Sun et al., 2025a, 2025b). Second, Cross-basin generalization: models trained on one basin often fail when transferred to another due to differences in lithology, diagenesis, and stress regimes. Third, Multimodal data fusion: integrating diverse inputs (logs, images, seismic, core descriptions) effectively is still an open challenge (Mishra et al., 2022). Future advances may leverage few-shot/self-supervised learning to reduce annotation dependence, physics-informed neural networks to enforce geological consistency, and transformer-based multimodal architectures that jointly process numerical logs and high-resolution images.

3. Mechanical formation mechanisms of BPFs

Based on the dominant driving mechanisms, shale BPFs are classified into four genetic types: (1) Tectonic BPFs – formed by reactivation of pre-existing weak planes under regional compressive or shear stress; fluids sourced from open-system basin brines or, when magmatism is coeval, from hydrothermal systems (Cobbold et al., 2013; Su et al., 2022; Zhang et al., 2024, 2025). (2) Fluid-overpressure BPFs – generated by internal pore-pressure buildup during organic matter cracking in a closed to semi-closed system; cements precipitate from expelled formation fluids, not external fluids (Hoyt and Hooker, 2020; Liu et al., 2022). (3) Diagenetic BPFs – induced by differential volumetric contraction during compaction, primarily dehydration of clay minerals and densification of organic matter; occur in relatively closed systems at shallow-intermediate burial (Liu et al., 2022; Fu et al., 2023). (4) Unloading BPFs – created by reduction of overburden stress during uplift and erosion, often reactivating earlier sealed fractures; filled by low-temperature meteoric or shallow formation waters (Nelson, 2001). This classification integrates dynamic fluid sources with mechanical failure processes, providing a genetic-mechanism-driven framework that differs from descriptive classifications based solely on geometric attributes.

3.1. Tectonic BPFs

Tectonic BPFs arise when regional stresses reactivate preexisting weak planes in shale, including lamination or interlayer slip surfaces. The compositional and grain size heterogeneity produced during deposition and diagenesis yields bands of reduced shear strength and cohesion along these planes, which have lower internal friction than the surrounding rock. These weak zones concentrate stress and are preferential sites for failure (Anderson, 1981; Gale et al., 2014). Under compressive or shear stress, a weak plane experiences a combination of shear stress (τ_n) and normal stress (σ_n; Zoback, 2010; Zoback and Kohli, 2019). Shear failure occurs when τ_n exceeds the shear strength (τ_c), producing fractures that are mechanically concordant with bedding rather than creating new surfaces in the host rock (Fossen, 2016; Fossen and Rotevatn, 2016). The stresses on a plane at an angle θ with σ_1 ($\theta + \alpha = 90^\circ$ if α is measured relative to σ_3) are controlled by the magnitude and orientation of the principal stresses (σ_1, σ_2, and σ_3; Griffith, 1921). For a plane in the σ_1–σ_3 principal plane (Fig. 5a), the resolved stresses can be written as follows:

$$\sigma_n = \frac{\sigma_1 + \sigma_3}{2} + \frac{\sigma_1 - \sigma_3}{2}\cos(2\theta)$$

$$\tau_n = \frac{\sigma_1 - \sigma_3}{2}\sin(2\theta)$$

Failure initiates and propagates when the resolved shear stress on the weak plane exceeds its shear strength. If a plane is weaker than the host rock ($\tau_c < C_0$) and has a low internal friction coefficient (μ_w), it will fail preferentially, promoting BPF formation.

To quantify the propensity of tectonic stress to rupture a weak plane, we define the weak-plane failure coefficient as follows:

$$f_{aw} = \frac{\tau_n}{[\tau_n]}$$

where τ_n is the resolved shear stress on the bedding plane (MPa), and $[\tau_n]$ is the corresponding failure shear stress under the same normal stress (MPa). When $f_{aw} > 1$, the shear stress exceeds the failure threshold and fractures can may preferentially nucleate and propagate along the bedding-parallel weak surfaces. When $f_{aw} < 1$, the shear stress is insufficient for failure, and no fractures are expected to develop. In summary, this mechanical framework shows how regional tectonic stresses are concentrated in preexisting weak layers, promoting preferential rupture along bedding and the formation of BPFs, providing a quantitative basis for predicting the spatial distribution of tectonic fractures.

Under a triaxial principal stress state ($\sigma_1 \geq \sigma_2 \geq \sigma_3$; Fig. 5a), the normal and shear stresses acting on the bedding plane can be expressed as follows:

$$\sigma_n = \left(\sigma_1 \sin^2\theta + \sigma_2 \cos^2\theta \cos^2\alpha + \sigma_3 \cos^2\theta \sin^2\alpha\right)$$

$$\tau_n = \sqrt{\sigma^2 - \sigma_n^2}$$

where θ is the angle between the bedding plane and the maximum principal stress σ_1 (°) and α is the angle between the bedding plane and σ_3 within the σ_2–σ_3 plane (°). If the shear strength of the bedding plane is σ_{Cw} and the friction coefficient is μ_w, the critical shear stress for fracture initiation can be expressed as follows:

$$[\tau_n] = \sigma_{Cw} + \mu_W \times \sigma_n$$

Accordingly, the fracture coefficient of any weak plane can be expressed as

$$f_{aw} = \frac{\sqrt{\sigma^2 - \sigma_n^2}}{\sigma_{Cw} + \mu_W \times \sigma_n}$$

Using this equation, the development of tectonically induced BPFs can be evaluated quantitatively for a given stress state and bedding-plane orientation, and the failure site and criterion can be visualized on a Mohr diagram. When the stress state, orientation of the weak plane, shear strength, and friction coefficient are known, the fracture coefficient can be calculated. A value of ≥1 indicates fractures will develop. In the special case where $\sigma_{Cw} = \sigma_C$ (homogeneous rock), the equation reduces to the Coulomb criterion, $\tau_n = \sigma_C + \tan\varphi \times \sigma_n$, where φ is the internal friction angle. This demonstrates that tectonic BPFs arise as manifestations of preexisting weak planes. The equation provides a systematic solution for the failure of weak planes under tectonic stress and offers a robust basis for predicting the distribution of BPFs.

Furthermore, if the stress state, shear strength, friction coefficient, and orientation of preexisting weak zones are known, the corresponding fracture coefficient can be calculated directly.

When $\sigma_{Cw} = 0$ and μ_w is replaced by the friction factor (f_F), the activity coefficient of preexisting faults (f_{aF}) can be written as

$$f_{aF} = \frac{\sqrt{\sigma^2 - \sigma_n^2}}{f_F \times \sigma_n}$$

The equation above equates f_{aF} with f_{aw}. Collectively, these values are referred to as the activity coefficient of preexisting structures (f_{aS}).

When $\sigma_{Cw} = \sigma_C$ (equivalent to a homogeneous medium), the shaded region in Fig. 5 collapses to a single point (A), where the section forms an angle $\theta = 45^\circ - \varphi/2$ with σ_1 and is perpendicular to σ_3 ($\alpha = 90^\circ$).

Figure XX shows that only point A yields an activity coefficient of 1, whereas at all other points the activity coefficient is <1. Substituting the conditions for point A ($\alpha = 90°$, $\theta = 45° - \varphi/2$) and for a homogeneous case ($\sigma_{Cw} = C$, $\mu_w = \tan\varphi$) gives

$$f_{aw} = \frac{\sqrt{\left(\sigma_1^2\sin^2\theta + \sigma_3^2\cos^2\theta\right) - \left(\sigma_1\sin^2\theta + \sigma_3\cos^2\theta\right)^2}}{C + \tan\varphi \times \left(\sigma_1\sin^2\theta + \sigma_3\cos^2\theta\right)} = 1$$

Further simplification yields

$$\tau_n = C + \tan\varphi \times \sigma_n$$

Where

$$\tau_n = \sqrt{\left(\sigma_1^2\sin^2\theta + \sigma_3^2\cos^2\theta\right) - \left(\sigma_1\sin^2\theta + \sigma_3\cos^2\theta\right)^2}$$

$$\sigma_n = \sigma_1\sin^2\theta + \sigma_3\cos^2\theta$$

The Coulomb–Mohr criterion for homogeneous media clearly represents a special case of the failure criterion. The equation above provides a solution for rock failure in geological bodies containing preexisting weak planes, offering critical insights into the origin of BPFs and clarifying the mechanisms governing their formation under tectonic stress.

3.2. Hydrocarbon fluids overpressure BPFs

Hydrocarbon-generated overpressure BPFs are secondary fractures that develop during basin evolution when anomalously high-pressure fluids generated by the decomposition of organic matter (e.g., kerogen cracking) accumulate in closed or semi-closed systems. The resulting increase in pore pressure (P_p) drives fracture initiation and propagation along bedding planes. These fractures develop widely in deeply buried shales, mudstones, and tight sandstones, where they increase the permeability and fluid transport substantially, forming a critical geological mechanism for hydrocarbon enrichment and high-yield wells.

In closed systems, including organic-rich mudstone and tight sandstone intervals, increasing burial depth and temperature promote the generation of large volumes of fluid (oil, gas, and water) from the decomposition of organic matter. If fluid expulsion is inhibited, the pore pressure continues to rise (Kravchenko et al., 2014; Lander and Laubach, 2015). Once the pore pressure becomes sufficiently high, the effective stress (σ') in the rock decreases significantly. According to the effective stress principle (Fig. 5b), the effect of pore pressure on the effective stress (σ'_n) can be expressed as

$$\sigma'_n = \sigma_n - P_p$$

Using the modified Coulomb criterion, f_{aw} can be written as

$$f_{aw} = \tau_n/(\sigma_{cw} + \mu_W \times \sigma'_n)$$

Alternatively, using the Griffith fracture criterion when $\sigma'_n < 0$, f_{aw} can be expressed as

$$f_{aw} = |\sigma'_n|/\sigma_T$$

In extensional settings, hydrocarbon generation overpressure occurs when $P_p > \sigma_3 + \sigma_T$, at which point $\sigma'_3 < 0$ and tensile fractures develop (Fig. 5b). By further refining this equation, the magnitude of hydrocarbon overpressure (ΔP_p) can be estimated as follows:

$$\Delta P_p = \left(V_g \cdot R \cdot T\right)/(\varphi \cdot \beta)$$

where V_g is the volume of generated hydrocarbons (m^3), R is the molar gas constant (dimensionless), T is the temperature (°C), ϕ is the porosity (%), and β is the compressibility coefficient (dimensionless).

This equation can be used to predict transitions in fracture type; e.g., when the pore pressure (P_p) increases by 10 MPa, the Mohr circle shifts leftward, and the probability of tensile fracturing increases. Therefore, hydrocarbon-generated overpressure is a key driver of BPFs, particularly in shale gas reservoirs.

The formation of overpressure BPFs can be divided into three stages. Stage 1 involves the build-up of pore pressure, where the cracking of organic matter generates large volumes of fluid that cannot be expelled, leading to a progressive increase in pore pressure. Stage 2 is a reduction in the effective stress. Elevated pore pressure reduces the effective stress sharply. The minimum principal stress can potentially become negative, placing the system in a tensile or extensional-shear regime. Stage 3 is the activation and propagation of fractures. Once the Mohr circle becomes tangential to the failure envelope, fractures initiate along bedding planes and subsequently propagate under continued hydrocarbon overpressure and regional tectonic stress.

These fractures develop widely in shale gas, tight oil and gas reservoirs, and deeply buried source rocks. They typically occur as dense clusters of fractures aligned with bedding planes, forming microfracture networks that increase the effective porosity and permeability substantially, enhancing hydrocarbon migration and accumulation.

In summary, the formation of overpressure BPFs is driven by the generation of anomalously high pore pressure during hydrocarbon generation, which reduces the effective stress and triggers tensile or extensional-shear failure along weak bedding planes. This mechanism provides a robust mechanical basis for predicting fracture development and enrichment patterns in shale and tight hydrocarbon reservoirs.

3.3. Diagenetic BPFs

Diagenetic BPFs are induced mainly by differential shrinkage during sedimentary diagenesis. They represent a secondary fracture type that develops along bedding planes as a result of volumetric contraction and stress concentration during compaction, pressure solution, and mineral transformation (Morley et al., 1990; Liu et al., 2017a, 2017b). During diagenesis, variations in grain size, mineral composition, and hydration state generate pronounced mechanical heterogeneities across bedding planes (Zahid et al., 2016). Critically, the volumetric contraction that drives fracture opening is primarily associated with clay-mineral dehydration (e.g., smectite-to-illite transformation), the thermal maturation of organic matter (kerogen to oil/gas), and the collapse of hydrated interlayers (Luo et al., 2021). In contrast, rigid grains such as quartz, feldspar, and carbonate typically undergo negligible thermal or chemical shrinkage under diagenetic conditions (Du et al., 2021).

During diagenetic compaction, the overburden stress (G) increases progressively as the geothermal gradient increases, enhancing pore water expulsion and mineral recrystallization and driving bulk volumetric contraction of the rock (Peacock et al., 2000; Ren et al., 2019). Because mineral compositions and physicochemical shrinkage differ above and below bedding planes, differential contraction develops along these interfaces, generating localized tensile stress (σ_s). When σ_s exceeds the tensile strength of the rock (σ_T), tensile BPFs initiate along mechanically weak bedding surfaces.

These fractures are common in siltstone, tuff, and silty mudstone reservoirs. They are typically discontinuous or curved features along bedding planes and, in some cases, have feather-like branches. BPF densities range from a few to several tens per meter, with individual apertures of generally <60 μm. Although they are narrow and limited in length, their high density enhances the microscale permeability of the host rock substantially.

From a mechanical perspective, the formation of diagenetic BPFs can be divided into two stages. During the residual stress accumulation stage, differences in mineral composition and grain size above and below bedding planes cause uneven shrinkage during compaction and diagenesis, generating a residual tensile stress field (σ_r) parallel to the bedding plane (Hooker et al., 2018). During the fracture propagation stage, the residual tensile stress increases and eventually reaches or exceeds the tensile strength of the rock, initiating tensile failure along

mechanically weak bedding planes and driving fracture propagation (Fig. 5c).

The shrinkage stress is assumed to be given by

$$\sigma_s = k \cdot (\Delta V/V) \cdot E$$

where k is the shrinkage coefficient (controlled by mineralogical differences, typically 0.1–0.5), $\Delta V/V$ is the volumetric shrinkage ratio, and E is the elastic modulus of the rock (MPa).

Fracture formation follows the Griffith criterion; i.e., fractures develop when the driving stress (σ_d) exceeds the tensile strength:

$$\sigma_d = \sigma_s + \sigma_r - G$$

$$f_{aw} = \sigma_d/\sigma_T$$

where σ_r is the residual stress due to the diagenetic history (MPa) and G is the overburden pressure (MPa). When $f_{aw} \geq 1$, diagenetic bedding fractures are expected to form.

Extending the equation above, the spacing (d) of diagenetic bedding fractures can be estimated as follows (Fig. 5c):

$$d = k_t \cdot (T/\sigma_s)$$

where k_t is the diagenetic factor, which reflects bedding type and ranges from 0 to 1 (0.5 for parallel bedding and 1.0 for cross bedding).

Diagenetic contraction typically occurs at depth, generating stress parallel to the bedding planes and producing fractures aligned with them. On a Mohr diagram, this process is expressed as a leftward shift of the circle under tensile stress, with tensile fractures forming once the rock's tensile strength is exceeded. The formation of diagenetic BPFs reflects the concentration of tensile stress along mechanically weak bedding surfaces, driven by differential shrinkage during compaction and mineral transformation. This mechanism provides a robust mechanical basis for interpreting microfracture density in reservoirs and its influence on fluid flow.

3.4. Unloading BPFs

Unloading BPFs form primarily during uplift and erosion, when the reduction in overburden pressure releases residual stress and generates a driving stress (Wang et al., 2021). When σ_d exceeds the tensile strength of the rock, tensile fractures develop preferentially along bedding planes. This mechanism is common in outcrops or shallow interval, with the fracture scale controlled by the magnitude of unloading (Laubach et al., 2010).

The overburden pressure decreases during uplift, whereas residual stresses retained from earlier tectonic or diagenetic processes and hydrostatic pressure (P) remain unchanged, resulting in net tensile stress (Olson et al., 2009). The driving stress, defined as $\sigma_d = \sigma_r + P - G$, promotes fracture propagation along bedding planes. As unloading reduces the minimum principal stress (σ_3; Fig. 5d), the Mohr circle shifts leftward, and tensile fractures initiate when the circle becomes tangential to the Griffith envelope in the negative σ_n domain (Zeng et al., 2023).

This mechanism follows the Griffith criterion, highlighting the dominance of tensile failure during unloading:

$$\sigma_d = \sigma_r + P_p - G$$

When the driving stress exceeds the tensile strength of the rock, tensile failure occurs along mechanically weak bedding planes, forming extensional fractures. These fractures are widely developed in outcrops, shallow reservoirs, and regions of large-scale uplift and erosion, with their scale, density, and intensity controlled by the magnitude (ΔG) and rate of unloading (Fig. 5d).

From a mechanical perspective, unloading reduces σ_3 progressively, and the rock mass enters a tensile regime once σ_3 becomes negative. On a Mohr diagram, unloading shifts the circle leftward, and tensile fractures initiate when it becomes tangential to the Griffith envelope in the negative σ_n domain. Uplift and erosion reduce overburden stress, increase the relative importance of pore pressure, and release residual stress, producing a tensile stress state. Unloading BPFs develop when $\sigma_d \geq \sigma_T$ and stress release drives tensile failure along bedding planes. The formation of unloading BPFs can be divided into three stages. Stage 1 is uplift and unloading, when progressive uplift and erosion reduce the overburden stress. During stage 2, residual stress and hydrostatic pressure dominate and remain relatively stable over short timescales, generating a net tensile driving stress. During stage 3, fractures initiate and propagate. Once σ_d exceeds the tensile strength of the rock, fractures initiate along bedding planes and propagate outward.

To quantitatively assess the driving capacity of stress release for fracture development, we introduce the unloading fracture activation coefficient:

$$f_{aw} = \sigma_d/\sigma_T$$

When $f_{aw} \geq 1$, BPFs are expected to develop. The residual stress can be estimated from historical stress models as follows:

$$\sigma_r = (1-\mu) \cdot \sigma_t/E$$

where μ is Poisson's ratio and σ_t is the maximum paleostress (MPa).

By further refining the equation, the spacing of unloading-induced fractures (L) can be related to the magnitude of unloading as follows:

$$L = K_u \cdot (1-\mu) \cdot \left(\frac{\sigma_T}{\sigma_d}\right)$$

where K_u is the unloading coefficient (0.2–1.0).

In areas of uplift and erosion, when ΔG reaches 20 MPa, σ_d increases, leading to a corresponding increase in the fracture density. This mechanism explains the origin of surface BPFs and has practical value for reservoir modeling.

Unloading BPFs are important in reservoir engineering and predicting natural fractures. Their formation increases reservoir permeability, provides pathways for hydrocarbon migration, and facilitates the extension of hydraulic fracture networks during the formation of shale gas, coalbed methane, and deep tight reservoirs.

In summary, unloading BPFs originate during uplift and erosion, when the reduction in overburden stress generates a net tensile driving stress that exceeds the tensile strength of the rock, leading to tensile failure along mechanically weak bedding planes. This mechanism provides a robust mechanical basis for analyzing and predicting fracture distributions under uplift and erosion regimes.

Therefore, to fully decipher the origin of a given BPF set, mechanical analysis must be complemented by geochemical and geochronological interrogation of the fracture cements. We need to examine the petrographic, fluid-inclusion, isotopic, and chronological signatures that fingerprint the fluid regime and absolute timing of cementation, thereby converting a generic “tectonic” or “overpressure” mechanism into a specific, testable geological history.

4. Cements in BPFs

4.1. Tectonic BPFs

Cements in tectonic BPFs are not only blocky, but often are fibrous or elongated (Bons et al., 2012; Quandt et al., 2021; Zhao and Li, 2022). Fibrous veins typically form in closed or semi-closed fracture systems where fracture opening and mineral growth occur synchronously, consistent with a crack–seal mechanism (Hilgers et al., 1997; Wiltschko and Morse, 2001; Virgo et al., 2016). Under a stable stress field, particularly with a low σ_3, fractures open incrementally and are immediately invaded by fluid. Minerals precipitate along the walls to produce fibers oriented approximately normal to the vein walls (Elburg

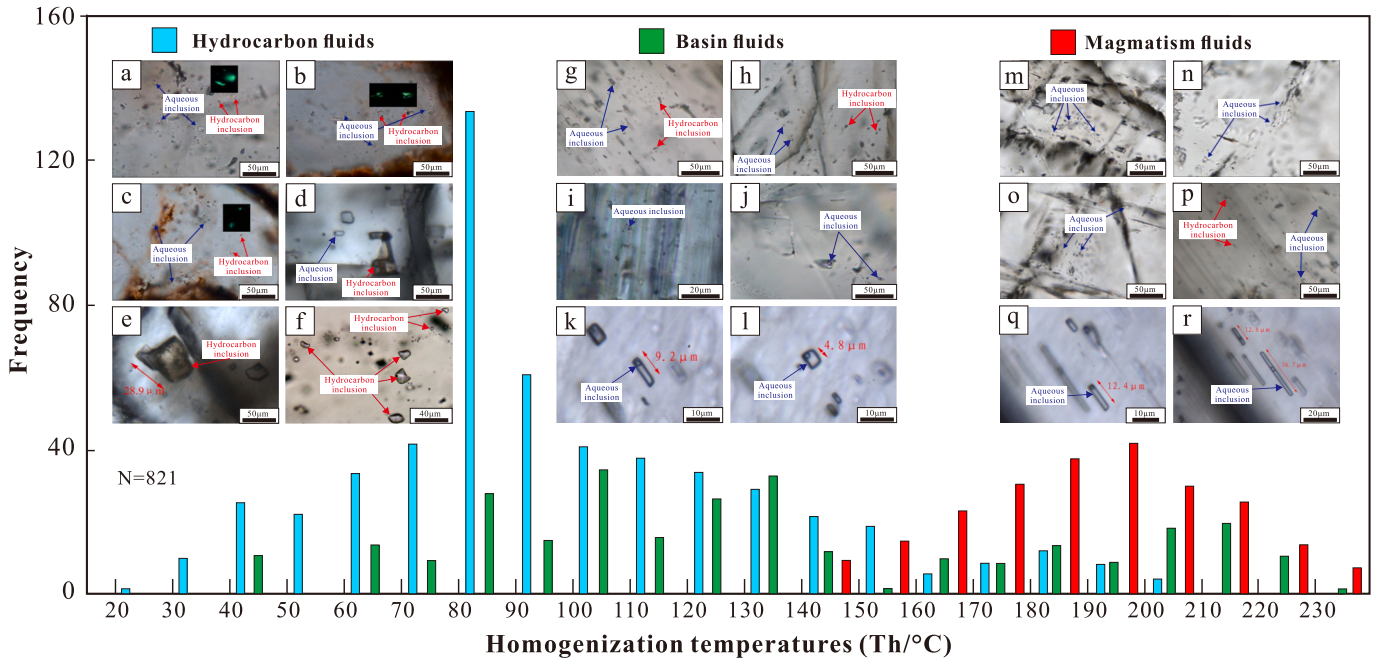

Fig. 6. Histogram of homogenization temperatures (T_h) for calcite cement in BPFs. (a–r) Fluid inclusions in BPF cements. (a–f) Hydrocarbon-generation-related BPF cements with coexisting aqueous and hydrocarbon inclusions. (g–l) BPF cements dominated by aqueous inclusions, indicating basin-fluid infill associated with tectonic activity. (m–r) BPF cements dominated by aqueous inclusions, indicating infill by high-temperature fluids generated during tectonic activity. Data from Jochum et al. (1995), Wang (2016), Li (2018), Lu et al. (2021), Wu et al. (2022), Luo et al. (2021), Su et al. (2022), Wang et al. (2022), Zhang et al. (2022), and Sun et al. (2023), together with unpublished data.

et al., 2002; Zhang et al., 2015). Repeated cycles of opening and sealing yield well-ordered fibrous veins with the long axes of the crystals aligning with the opening direction, preserving a microstructural record of the stress history (Urai et al., 1991; Hilgers et al., 1997; Bons et al.,

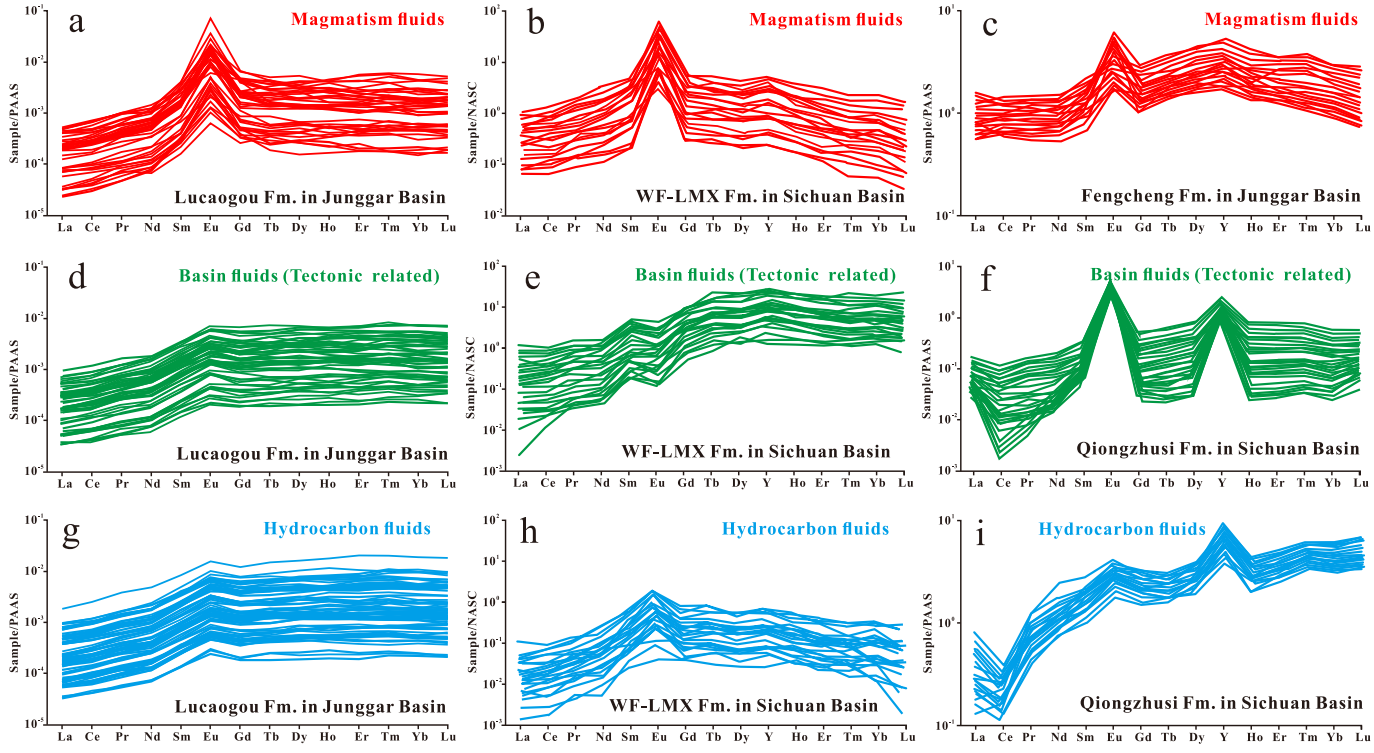

Fig. 7. Rare earth element patterns of fracture-filling cements in BPFs with different origins. Hydrothermal fluids from (a) the Lucaogou Formation, Junggar Basin; (b) the Wufeng–Longmaxi Formation, Sichuan Basin; and (c) the Fengcheng Formation, Junggar Basin. Basin fluids from (d) the Lucaogou Formation, Junggar Basin; (e) the Wufeng–Longmaxi Formation, Sichuan Basin; and (f) the Qiongzhusi Formation, Sichuan Basin. Hydrocarbon-derived fluids from (g) the Lucaogou Formation, Junggar Basin; (h) the Wufeng–Longmaxi Formation, Sichuan Basin; and (i) the Qiongzhusi Formation, Sichuan Basin. Data from Luo et al. (2021), Yuan (2022), Fan et al. (2023), and Zhang et al. (2025), together with unpublished data.

2012; Virgo et al., 2016).

Elongated ribbon-like fills commonly reflect discontinuous opening and variable fluid activity (Quandt et al., 2021; Zhao and Li, 2022). In settings with complex stress perturbations or near fault boundaries, localized stress concentrations, lithologic heterogeneities, or preexisting weaknesses promote partial non-throughgoing dilation (Gaboury and Daigneault, 2000; Zhang et al., 2015). Fluids are then introduced in pulses, and minerals precipitate only in favorable microenvironments, forming lenses or banded bodies with irregular shapes and large variations in thickness (Oliver and Bons, 2001; Zhao and Li, 2022). These veins commonly contain blocky or granular crystals with poorly developed preferred growth directions, indicating complex hydrodynamic conditions and rapid unstable crystallization (Elburg et al., 2002). Some fibrous veins exhibit S- or C-type geometries, recording syn-crystalline shortening and shear (Hilgers et al., 1997; Zhao and Li, 2022).

When tectonic activity does not trigger magmatism or when magmatic–hydrothermal fluids fail to penetrate BPFs, fracture cements are sourced predominantly from basin fluids (Gleeson et al., 2003; Su et al., 2022; Yu et al., 2023). In these cases, chemical and isotopic compositions, together with fluid inclusion signatures, reflect open-system basin fluid characteristics (Fig. 6g–l; Haller et al., 2010; Yu et al., 2023). The fluids may be derived locally from the host rocks bordering the fractures (Wang et al., 2015; Su et al., 2022), or tectonic pumping and enhanced connectivity can introduce fluids from overlying or underlying strata (Suchy et al., 2002; Gleeson et al., 2003; Fusswinkel et al., 2014). Consequently, both the geochemical compositions of the cements and inclusion assemblages inherit the diagnostic signatures of the basin-derived fluids (Fig. 6; Dix and Robinson, 2003; Su et al., 2022).

A second end-member occurs where tectonic activity is coupled with magmatism, allowing hydrothermal fluids to infiltrate BPFs network and impart a distinct hydrothermal signature to the cements (Warmada et al., 2007; Morishita and Takeno, 2010; Li et al., 2025b, 2025a). In these settings, fluid inclusions commonly record homogenization temperatures (T_h) that are higher than the expected formation temperatures of the enclosing strata (Fig. 6m–r), consistent with an external, high-enthalpy fluid source (Warmada et al., 2007; Fan et al., 2012). A positive Eu anomaly is a key geochemical indicator (Li et al., 2025b, 2025a). Under reducing high-temperature conditions, Eu^{3+} is partially reduced to Eu^{2+}. As the larger ionic radius of Eu^{2+} limits its incorporation into rock-forming minerals, the retention of Eu in the fluid phase is favored. During cooling and carbonate precipitation, Eu^{2+} reoxidizes to Eu^{3+}, whose ionic radius closely matches that of Ca^{2+}, enabling substitution into calcite and producing a positive Eu anomaly in hydrothermal carbonates (Fig. 7a–c; Warmada et al., 2007; Sahoo et al., 2022; Li et al.,

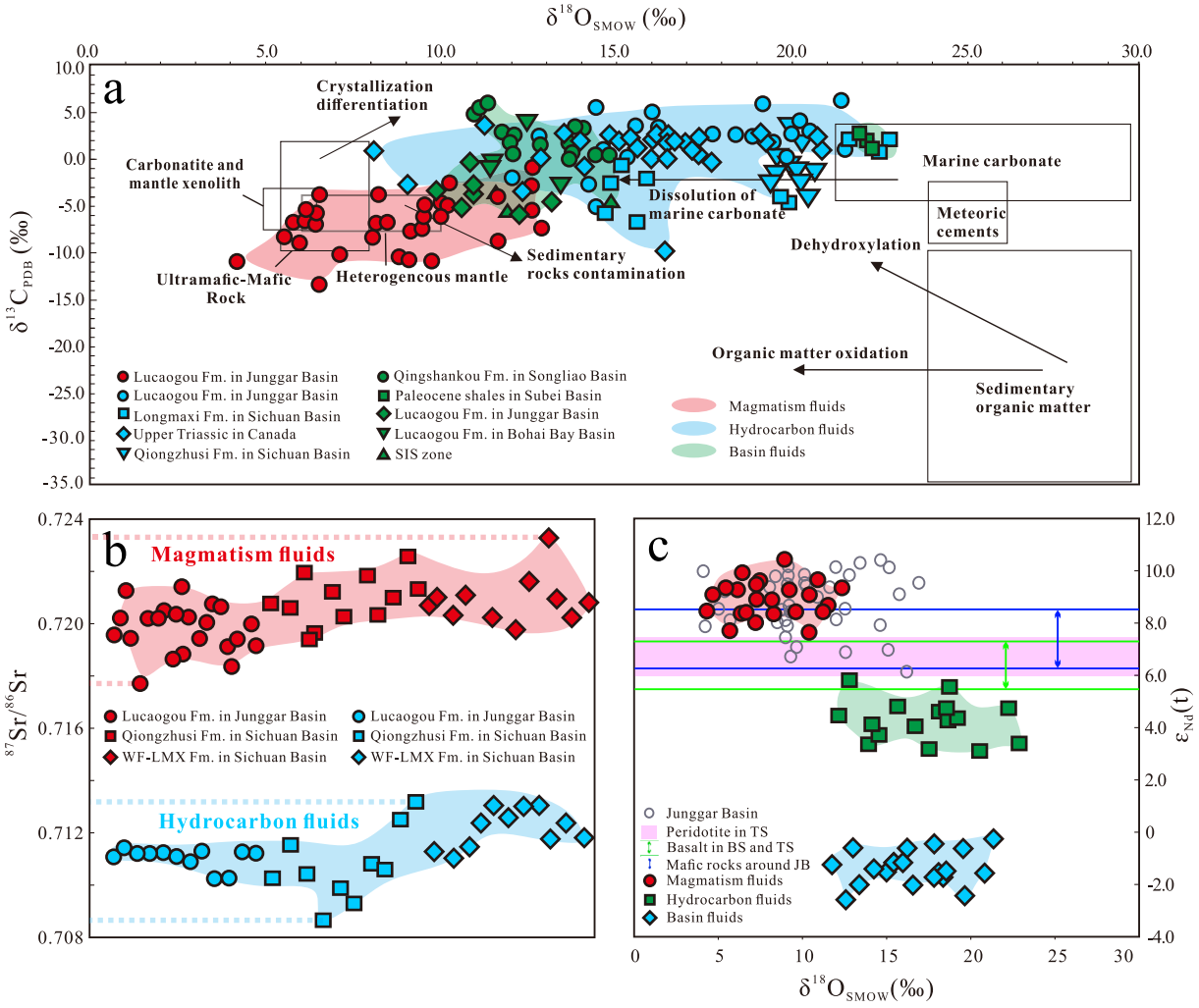

Fig. 8. C–O–Sr–Nd isotopic compositions of fracture-filling cements in bedding-parallel fractures. (a) C—O isotopic compositions, (b) $^{87}Sr/^{86}Sr$ ratios, and (c) O—Nd compositions of shale fracture cements from different basins. Data for the Lucaogou Formation, Junggar Basin, are from Zhang et al. (2025); for the Qingshankou Formation, Songliao Basin, are from Zhang et al. (2023); for the Paleogene shales of the Subei Basin are from Su et al. (2022); for the Paleogene shales of the Bohai Bay Basin are from Jin et al. (2007); for the Longmaxi Formation, Sichuan Basin, are from Wu et al. (2021); for the Qiongzhusi Formation, Sichuan Basin, are unpublished; and for Upper Triassic shales in Canada are from Al-Aasm et al. (1995).

2025b, 2025a).

Isotopic compositions are sensitive tracers of hydrothermal input (Yang et al., 2013). Carbon isotopes in volcanic–hydrothermal or deep magmatic fluids commonly yield broad ranges of $\delta^{13}C$ values (Moussa et al., 2019). Oxygen isotopic compositions reflect both fluid sources and crystallization temperatures: elevated temperatures typically result in lower $\delta^{18}O$ values (Hall et al., 1989; Morohashi et al., 2008). Thus, $\delta^{18}O$ values of fracture cement that are markedly lower than those of the host rock indicate precipitation from high-temperature hydrothermal fluids or from deep-sourced fluids mixed with formation water (Fig. 8a; Horton et al., 2003; Ren et al., 2021). These signatures are documented in calcite cements from BPFs in the Lucaogou Formation in the Junggar Basin (linked to Permian post-collisional magmatism), the Wufeng–Longmaxi succession in the Sichuan Basin (associated with the Emeishan large igneous province), and the Bohai Bay Basin (related to Cenozoic subduction magmatism), all of which yield $\delta^{18}O$ values lower than those of adjacent host rocks (Fig. 8a). More generally, $\delta^{18}O$ values can be used to estimate the initial isotopic composition of diagenetic or hydrothermal fluids and constrain fluid temperatures and evolution paths (Banner and Hanson, 1990; Taylor, 1974).

Strontium isotopic compositions are conservative in hydrothermal systems and exhibit minimal fractionation, so fluids from different sources, including seawater, formation water, magmatic and hydrothermal fluids, and crustal fluids, carry distinct signatures (Nadeau et al., 2018; Quandt et al., 2019; Chandra et al., 2024). Anomalous shifts in the $^{87}Sr/^{86}Sr$ ratios of cements, therefore, provide key evidence for external hydrothermal input (Zhao et al., 2015). In closed diagenetic settings, the Sr isotopic compositions of the cements typically track coeval seawater or the host carbonate, reflecting formation water buffered by slow exchange with the wall rock (Katz and Bullen, 1996; Fanlo et al., 1998; Clauer et al., 2017). Systematic departures from this background, such as abrupt increases or decreases accompanied by enrichment in trace elements or REEs (Fig. 8b), indicate hydrothermal incursion (Savelieva et al., 2008; Wind et al., 2023). Two end-member signals are common. First, high $^{87}Sr/^{86}Sr$ ratios point to crust-derived fluids that interact with Rb-rich lithologies, such as granites or metapelites (Fig. 8b), which drive the $^{87}Sr/^{86}Sr$ ratios of the cement above that of seawater (Zhao et al., 2015; Wind et al., 2023; Chandra et al., 2024). Second, low $^{87}Sr/^{86}Sr$ ratios indicate mantle-derived or magmatic inputs, particularly where fluids equilibrate with basaltic or ultramafic rocks (Hoernle, 1998; Quandt et al., 2019; Schwarzenbach et al., 2021).

Neodymium isotopic compositions are well suited for resolving subtle deep-sourced inputs in complex, multistage hydrothermal systems (Uysal et al., 2007; Barker et al., 2009). Although Nd contents in carbonates are low and often require solution enrichment or laser ablation–multicollector–inductively coupled plasma–mass spectrometry for precise determination, robust $\varepsilon Nd(t)$ values are highly diagnostic (Barker et al., 2009; Henjes-Kunst et al., 2014). Crust-derived fluids, particularly those that have interacted with ancient continental crust, typically yield negative $\varepsilon Nd(t)$ values and low $^{143}Nd/^{144}Nd$ ratios, whereas mantle-derived fluids or fluids related to mafic or ultramafic rocks retain more primitive signatures with higher $^{143}Nd/^{144}Nd$ ratios (Bell et al., 1989; Voicu et al., 2000). Joint Sr—Nd isotopic compositions are especially powerful for reconstructing fracture-fluid histories and sources (Uysal et al., 2007; Barker et al., 2009; Laubach et al., 2010). In tectonic fracture systems, low $\varepsilon Nd(t)$ values in cements together with radiogenic Sr isotopic compositions ($^{87}Sr/^{86}Sr > 0.718$) indicate extensive interactions with upper-crustal Al- and Si-rich lithologies during fluid migration (Fig. 7a; Uysal et al., 2007; Barker et al., 2009). This is similar to the isotopic compositions of deep magmatic fluids. These signatures are common where fractures tap deep crustal conduits, fault zones, or basement rocks, highlighting their role in channeling mass transfer from deep to shallow levels (Laubach et al., 2010, 2019). Conversely, calcite with $\varepsilon Nd(t)$ values near those of the mantle (e.g., $\varepsilon Nd(t) > -2$) suggest direct contributions from magmatic–hydrothermal or mantle-degassing fluids (Bell et al., 1989; Voicu et al., 2000; Louvel et al., 2022). This pattern is widespread along the margins of igneous provinces, vent systems, and fracture zones influenced by intrusions (Barker et al., 2009; Louvel et al., 2022). Illustrative cases include bedding-parallel calcite cements in the Lucaogou Formation in the Junggar Basin and in the Wufeng–Longmaxi succession in the Sichuan Basin, both of which are related to Permian magmatism and have relatively high $\varepsilon Nd(t)$ values (>7), consistent with regional igneous rocks (Fig. 8c). These $\varepsilon Nd(t)$ values commonly coexist with low $^{87}Sr/^{86}Sr$ ratios, low $\delta^{13}C$ and $\delta^{18}O$ values, positive Eu anomalies, and high-temperature fluid inclusions, which together are indicative of deep hydrothermal inputs (Drake et al., 2015; Louvel et al., 2022).

4.2. Fluid overpressure BPFs

During hydrocarbon generation, early generated oil occupies pore space and increases the pore-fluid pressure (Tingay et al., 2013; Fall et al., 2015). Continued generation drives the pressures higher until it exceeds the tensile strength of weak laminae in shale, initiating BPFs that are then charged with hydrocarbons (Becker et al., 2010; Fall et al., 2015; Williams et al., 2017). The petrography of veins differs between the oil and gas windows. Bedding-parallel fibrous cement-filled fractures can be attributed to crystal growth rates that outpace the vertical propagation of the fracture, consistent with crack–seal growth during the main stage of liquid-hydrocarbon generation, when lithostatic pressures are reached only episodically and sublithostatic fluid overpressures generally prevail (Osborne and Swarbrick, 1997; Bons, 2001; Laubach et al., 2004; Lash and Engelder, 2005; Gasparrini et al., 2014). In contrast, blocky-filled BPFs commonly form during peak gas generation, when oil cracking to gas produces volumetric expansion by a factor of ~500, rapidly opening fractures. Under these conditions, superlithostatic pressures in CH_4-saturated fluids can persist and widen fracture faster than cements can precipitate (Barker, 1990; Wang et al., 2023).

Analyzing fluid inclusions in fracture cements is a primary diagnostic method for overpressure-driven hydrocarbon-related BPFs (Laubach et al., 2004; Gasparrini et al., 2014). During crystallization, cements trap coeval fluids. The presence of liquid or gaseous hydrocarbons (e.g., oil or methane; Fig. 6a–c) demonstrates that hydrocarbon-charged fluids entered the fracture system and participated in mineral precipitation (Fisher and Brantley, 1992; Jochum et al., 1995). Two or three phases are typically visible in hydrocarbon inclusions under transmitted light: pale yellow to brown liquid oil and prominent vapor bubbles. Under fluorescence microscopy, they emit blue, green, or orange fluorescence depending on their composition and maturity, providing a robust indication of hydrocarbon charging (George et al., 2001; Ping et al., 2019; He et al., 2022). The homogenization temperature (T_h) provides thermal constraints on timing. Homogenization temperatures concentrated around 60–130 °C together with liquid hydrocarbons (Fig. 6) indicate cement growth in the oil window, whereas CH_4-only inclusions (Fig. 6d–f) and T_h greater than ~180 °C point to late cracking and gas-dominant charging (Liu et al., 2009; Chi et al., 2020; Wang et al., 2022; Nandakumar et al., 2024). Thus, stage-specific T_h distributions resolve the sequence of hydrocarbon charging and distinguish fracture cements precipitated in the oil window from those precipitated in the gas window (Gasparrini et al., 2014; Nandakumar et al., 2024). Critically, capture pressures recorded by inclusions in overpressure-related veins exceed hydrostatic pressure and can approach or surpass the lithostatic pressure, as documented for calcite cements in BPFs in the Lucaogou and Wufeng–Longmaxi formations in the Sichuan Basin (Fig. 9; Li et al., 2023b, 2023a; Zhang et al., 2025).

The geochemical signatures of fracture cements also reveal overpressure-driven hydrocarbon-related BPFs. These fractures typically form in closed systems, where immobile formation fluids enable diffusive transfer of dissolved ions from the host shales into the fracture (Hooker et al., 2015; Wang et al., 2020; Gao et al., 2019). Under these

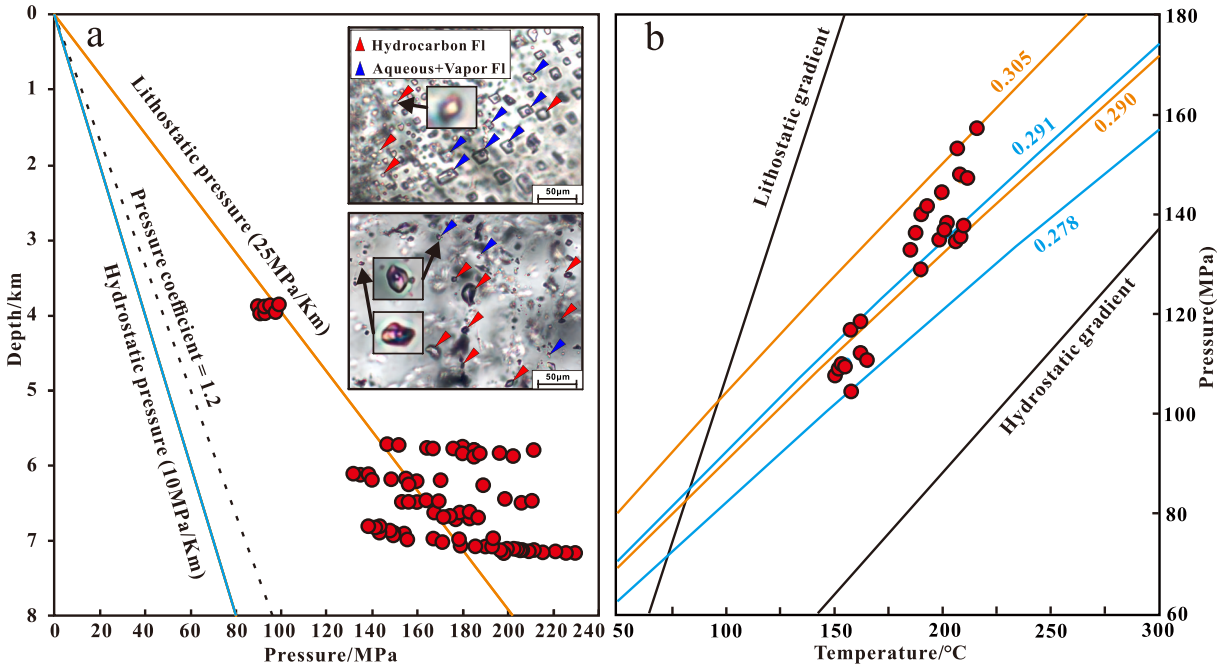

Fig. 9. Reconstruction of paleotemperature and paleopressure from vein cements in BPFs with different genetic origins. (a) Depth-dependent distribution of paleopressures from fracture veins. (b) Relationships between paleotemperature and paleopressure for different fracture types. Data from Wu et al. (2021), Wang et al. (2023), Liu et al. (2024b, 2024a), and unpublished data.

conditions, isotopic exchange between solutes and water leads to little long-term compositional difference between the host rock and cement (Fall et al., 2015; Fan et al., 2024a). Consequently, the major and trace element contents and C—O isotope ratios of cements commonly resemble those of the surrounding shale (Figs. 7g–i, 8a; Schaltegger et al., 1994; Schneider et al., 2002; Phan et al., 2018; Gao et al., 2020). Carbon isotopes are particularly informative, as the $\delta^{13}C$ values of calcite primarily reflect the source of the dissolved inorganic carbon (Fig. 8a). Systematic negative shifts relative to the host shales (e.g., $\delta^{13}C < -5‰$) imply inputs of CO_2 generated by the thermal decomposition of organic matter, indicating the influence of degassing mature source rocks or admixtures of carbon-bearing gases (e.g., CH_4 and CO_2; Mozley and Hoernle, 1990; Ayuso et al., 2004; Peyaud et al., 2006). An additional discriminator is cement age, as the precipitation of cement typically coincides with hydrocarbon generation (Banner et al., 1988; Schaltegger et al., 1994; Gao et al., 2020).

4.3. Diagenetic BPFs

Diagenetic shrinkage-related BPF cements record early fracture activity during the evolution of sedimentary rocks, driven by clay dewatering, the pyrolysis of organic matter, and volumetric contraction, which produce intrinsic fracture systems (Laubach et al., 2010, 2019; Meng et al., 2021). The formation of diagenetic BPFs does not require external tectonic stress and typically precedes, or is contemporaneous with, the early stages of porosity evolution during diagenesis (Loucks et al., 2009; Laubach et al., 2010; Gale et al., 2014).

The cements in diagenetic shrinkage fractures are dominated by calcite, with minor dolomite, quartz, mixed-layer illite–smectite, or authigenic clays in some samples (Uysal et al., 2007; Barker et al., 2009). The calcite is typically low-Mg, fine-grained, and well crystallized but irregular in shape. Quartz commonly occurs as microcrystalline to cryptocrystalline gel-like infill intergrown with calcite (Barker et al., 2009). In places, mixed-layer illite–smectite shows preferential alignment in the BPFs, indicating tight coupling between the evolution of clay minerals in the host rock and the fracture history during diagenesis (Uysal et al., 2007; Henjes-Kunst et al., 2014). Because cementation occurs early, cement fabrics generally lack high-temperature overprints, with sharp boundaries preserved and no hydrothermal signatures (Barker et al., 2009; Henjes-Kunst et al., 2014). These cements typify nontectonic fracture systems in shale and provide important pathways or diffusion conduits for microscale fluid migration (Drake et al., 2015; Laubach et al., 2019; Meng et al., 2021).

Diagenetic shrinkage-related bedding-parallel cements typically retain a geochemical signature close to that of sediments (Laubach et al., 2010, 2019; Meng et al., 2021). Calcite cements commonly have $\delta^{13}C$ values of approximately −3‰ to +2‰ and $\delta^{18}O$ values of approximately −10‰ to −4‰ on the V-PDB scale (Fig. 8a), consistent with precipitation in a relatively closed system governed by diagenetic formation water at low temperatures (Uysal et al., 2007; Barker et al., 2009). These isotopic compositions are similar to those of shallow basin fluids, and indicate the reprecipitation of carbonate dissolved in intraformational waters with no overprinting from external hydrothermal or deep fluids (Laubach et al., 2010, 2019). The Sr isotopic compositions of the cements generally match those of coeval seawater or the host mudstone and shale (e.g., $^{87}Sr/^{86}Sr = \sim 0.707–0.709$), suggesting that Sr is sourced from wallrock leaching mediated by diagenetic water and there is little to no magmatic or crustal input (Veizer, 1989; Uysal et al., 2007; Barker et al., 2009). REE patterns typically have negligible or slightly negative Eu anomalies (Fig. 7d, e; Barker et al., 2009; Louvel et al., 2022). In some cases, plagioclase contamination may give rise to positive Eu anomalies (Fig. 7f). This assemblage matches sedimentary to diagenetic carbonate systems and points to low-temperature, weakly reducing recirculated diagenetic waters with limited hydrothermal or oxidative modification (Barker et al., 2009; Rieger et al., 2022). Small one-phase liquid or two-phase liquid–vapor inclusions may occur in well-preserved calcite with T_h usually <70–100 °C (Fig. 6), indicating shallow burial or early stage diagenesis. The inclusions are small and dense, consistent with stable entrapment conditions (Gasparrini et al., 2014; Henjes-Kunst et al., 2014; Zhang et al., 2022).

In summary, the isotopic and chemical compositions of diagenetic shrinkage cements provide a robust basis for distinguishing diagenetic conditions from hydrothermal overprints (Barker et al., 2009; Laubach et al., 2019). In reservoirs with multistage fracture systems, separating

shrinkage fractures from later tectonic fractures is essential for reconstructing the evolution of the reservoir, clarifying the origins of the fractures, and building reliable fracture network architecture models (Gale et al., 2014; Meng et al., 2021).

4.4. Unloading BPFs

Unloading BPFs form during basin uplift and erosion when overburden removal lowers the confining pressure, prompting elastic rebound and stress readjustment that opens tensile cracks along bedding or other mechanically weak planes (Engelder, 1985; Gale et al., 2014; Laubach et al., 2019). These fractures typically develop late in the evolution of a basin. The cements record the influx of and precipitation from shallow fluids during unloading, and their mineralogical and genetic attributes distinguish them from both diagenetic and tectonic fractures (Barker et al., 2009; Gasparrini et al., 2014; Henjes-Kunst et al., 2014).

At the outcrop and core scales, unloading BPFs are typically horizontal to subhorizontal, parallel to bedding, and laterally persistent but narrow; many are partially cemented or remain slightly open (Engelder, 1985; Gale et al., 2014). The cements are dominated by calcite and dolomite, and commonly have fibers that grow perpendicular to the fracture walls, consistent with tensile opening followed by filling (Laubach et al., 2004; Hooker et al., 2012; Chenrai et al., 2022). Multiple cementation episodes are common: early fine fibrous calcite may be overgrown by later blocky calcite or microcrystalline quartz, resulting from repeated cycles of fracture opening, fluid influx, and partial sealing (Barker et al., 2009; Gasparrini et al., 2014; Henjes-Kunst et al., 2014).

Geochemical data indicate the presence of low-temperature shallow-sourced cements (Drake et al., 2014; Han et al., 2019; Chen et al., 2022). The $\delta^{13}C$ values of calcite are mostly between −3‰ and + 2‰ (V-PDB), consistent with mixtures of oxidized organic carbon and meteoric inputs, whereas the $\delta^{18}O$ values are typically negative (−10‰ to −16‰), indicating low-temperature precipitation from the surface or shallow percolating waters following uplift and exposure (Prosser et al., 1993; Smith et al., 2014; Nardini et al., 2019). Fluid inclusions yield T_h of ~60–100 °C, with some <50 °C, confirming near-surface cementation during late-stage cooling (Slobodník et al., 2006; Liu et al., 2017a, 2017b). REE patterns typically show enrichment in light REEs and a weak negative Eu anomaly (Fig. 7e), consistent with water–rock interaction in mildly redox or transitional settings (Cai et al., 2008; Grabezhev, 2010). The $^{87}Sr/^{86}Sr$ ratios of the cements are slightly higher than those of the host rocks, implying stronger exchange with terrigenous detritus or weathered regolith along flow paths (Carpenter et al., 1991; Gomes Jr et al., 2022).

Compared with hydrothermal veins, unloading BPFs lack high-temperature mineral assemblages, including abundant white mica, chlorite, and pyrite, and unloading BPFs do not yield anomalous REE enrichment or diagnostic hydrothermal fluid inclusions. These features suggests formation in a low-temperature regime with weak fluid flux (Liu et al., 2017a, 2017b; Han et al., 2019). Bitumen residues or oil staining in some fractures (Fig. 6a) indicate that hydrocarbons can seep along these planes even during unloading, providing evidence for late charging and microscale migration in unconventional reservoirs (Lash and Engelder, 2005; Gale et al., 2014; Gasparrini et al., 2014).

Across many petroliferous basins, extensive work on fluid inclusions, geochemistry, and the geochronology of cements has tightly constrained the origins of hydrocarbon generated overpressure-related BPFs and their tectonic counterparts. In contrast, cements in diagenetic shrinkage and unloading BPFs remain comparatively understudied. Interpretations of their origin are often semiqualitative and supported by limited quantitative datasets, leaving uncertainties in the timing, fluid sources, and mechanistic drivers that are critical for predictive models of fracture development and reservoir behavior.

4.5. Reliability and limitations of petrographic genetic discrimination

The preceding sections have documented distinct petrographic fabrics—fibrous, blocky, elongated-blocky, crack-seal, cone-in-cone—that are strongly correlated with specific BPF origins. However, relying solely on optical or SEM petrography for genetic diagnosis carries inherent risks.

First, convergent evolution of textures: Antitaxial fibrous veins can form under both hydrocarbon-overpressure (low opening rate, continuous growth) and tectonic-shear (syntectonic fiber bending) conditions; without fluid inclusion or geochemical data, these are easily confused (Su et al., 2022; Zhang et al., 2025). Second, overprinting and recrystallization: Early diagenetic blocky calcite may be recrystallized during later hydrothermal activity, obliterating primary textures and inheriting new geochemical signatures while preserving a misleading “blocky” appearance (Li et al., 2023b, 2023a). Third, subjective interpretation: The distinction between syntaxial, antitaxial, and stretching veins can be ambiguous in poorly oriented thin sections. Therefore, a tiered diagnostic workflow is recommended.

Tier 1: Petrography (core, thin section, CL) identifies candidate genetic types based on vein geometry, crystal habit, and paragenetic relationships. This step is fast, inexpensive, and applicable to every sampled vein.

Tier 2: Targeted microthermometry (fluid inclusions) and in-situ geochemistry (δ18O, $\delta^{13}C$, REE, Sr—Nd isotopes) are performed on a representative subset of veins that represent each petrographic end-member. These analyses resolve the fluid source, temperature, and redox state, providing a robust genetic assignment that can be extrapolated to petrographically similar veins within the same basin.

Tier 3: U—Pb or Sm—Nd dating of a further subset directly links fracture opening to basin events (hydrocarbon generation, magmatism, uplift).

In practice, this approach balances scientific rigor with practical feasibility; it has been successfully applied in the Junggar, Sichuan, and Bohai Bay basins to map the spatial and temporal distribution of different BPF families at the reservoir scale.

5. Role of bedding parallel fractures in hydrocarbon accumulation

5.1. Influence of bedding parallel fractures on hydrocarbon flow and lateral transport

BPFs are readily opened and laterally extensive, and they constitute important pathways for shale oil and gas flow. Spontaneous imbibition experiments show that the water-uptake depth along bedding planes is ~1.0 cm, shorter than the ~1.5 cm observed along tectonic fractures (Fig. 10). Despite this, the reaction zone along bedding planes experiences more complete imbibition than the reaction zone along tectonic fractures, leading to greater overall imbibition. Thus, BPFs do not have inherently lower imbibition capacities than tectonic fractures, and under suitable conditions their water uptake and stimulation efficacy can exceed those of tectonic fractures. When the lower bounds on oil–-water displacement properties can be neglected and the effects of gravity dominate, large pores on bedding planes may be less responsive; however, pervasive microfractures and pores can still imbibe efficiently and enhance the net effect of stimulation (Fig. 10d–f).

Beyond imbibition, BPFs strongly influence hydrocarbon flow and lateral transport. Their alignment with depositional layering creates relatively uniform conduits that promote even migration and distribution at the microscale while offering low-resistance pathways for lateral flux within and between adjacent laminae, increasing reservoir sweep efficiency. Although the imbibition depth along bedding planes is slightly smaller than that of tectonic fractures, the more uniform and complete response along bedding planes can improve well performance substantially and play an important role in multiscale reservoir

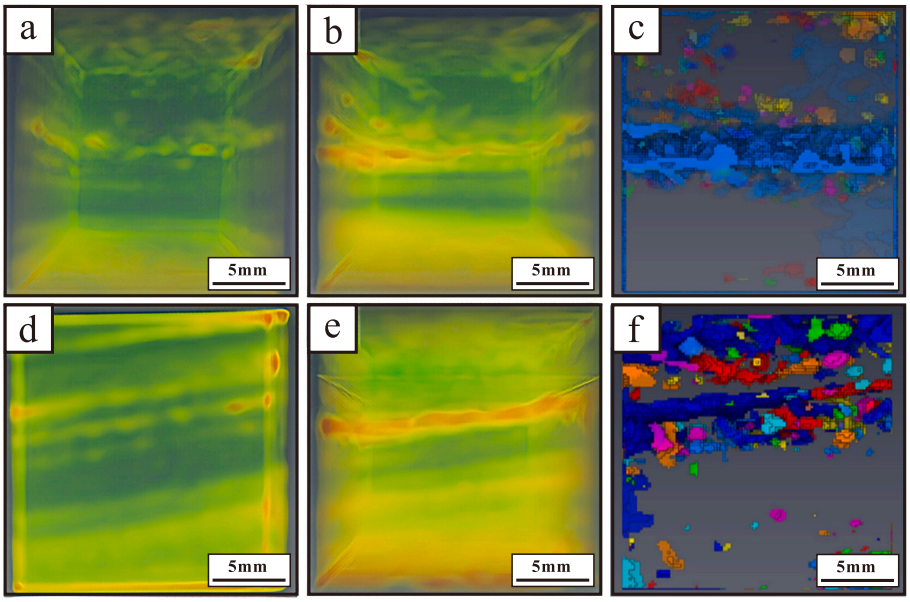

Fig. 10. CT images of spontaneous imbibition in tectonic fractures and BPFs (Luo et al., 2020). (a) CT image of a tectonic fracture prior to imbibition. (b, c) CT image of the same fracture after imbibition. (d) CT image of a BPF prior to imbibition. (e, f) CT image of a BPF after imbibition.

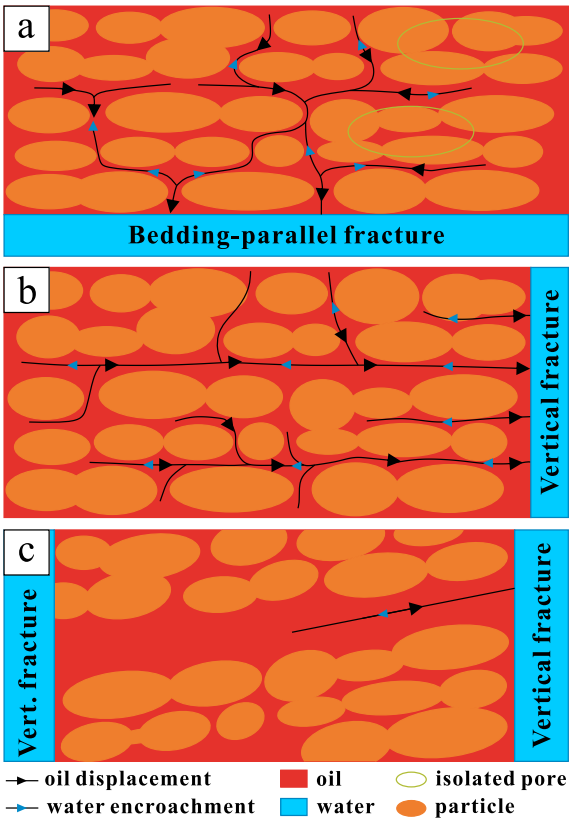

Fig. 11. Imbibition patterns in BPFs and tectonic fractures (Luo et al., 2020).

stimulation.

Shale reservoirs possess small pore-throat systems that generate high capillary pressures. The ratio of capillary to gravitational forces in these reservoirs is large and the system is effectively closed, so oil cannot diffuse outward. Imbibition, therefore, proceeds counter to gravity and is governed primarily by capillary action. During bedding-parallel flow, water enters the matrix through pore throats oriented perpendicular to bedding and displaces the remaining oil (Fig. 11a). The pore throats are narrow, ingress and egress paths are long and tortuous, and compaction and cementation locally flatten or obliterate vertical conduits, creating closed segments and dead-end pores that cannot be accessed by imbibing water.

When tectonic fractures are present, water advances along bedding-parallel paths and replaces oil in laterally connected pores, and the principal reaction channels are relatively straight horizontal pores and microfractures (Fig. 11). Dead-end volumes that are not swept during bedding-parallel imbibition can be accessed during tectonic fracture-dominated imbibition. In the presence of wider microfractures or BPFs (Fig. 11), capillary forces in a tectonic fracture leading upward may be insufficient to overcome gravity, thereby suppressing imbibition; in contrast, downwards capillary action and gravity act in the same direction, and water displaces oil in microfractures and BPFs.

Overall, bedding-parallel flow paths are more tortuous, but their narrower throats yield higher capillary pressures, so the imbibition times are broadly similar to those along tectonic fractures. Because BPF systems contain a larger fraction of dead-end pores, their ultimate imbibition efficiency is typically lower than that of tectonic fractures.

In summary, the contributions of BPFs to hydrocarbon flow, lateral transport, and stimulation efficiency cannot be judged solely from imbibition depth or fracture aperture. Robust assessment should integrate the completeness of imbibition, pore-scale attributes, and the geometry and connectivity of the microfracture network.

5.2. *Influence of BPFs on hydrocarbon migration and accumulation*

Analog modeling provides a powerful means to elucidate hydrocarbon charge and trapping. By reproducing migration in a controlled setting, experiments can reveal mechanisms that are otherwise difficult to infer in situ. Building on a configuration where bedding-parallel and high-angle fractures coexist, Zhang et al. (2025) investigated their coupled roles during shale oil accumulation and compared trapping outcomes across fracture domains.

In the experiments, a packed model was charged with kerosene as an oil analog and advanced through three stages. Stage 1 simulated the oil generation window. Kerosene entered the matrix and saturated pores without immediate leakage into fractures, mirroring in situ generation whereby oil first fills local storage. Stage 2 simulated migration.

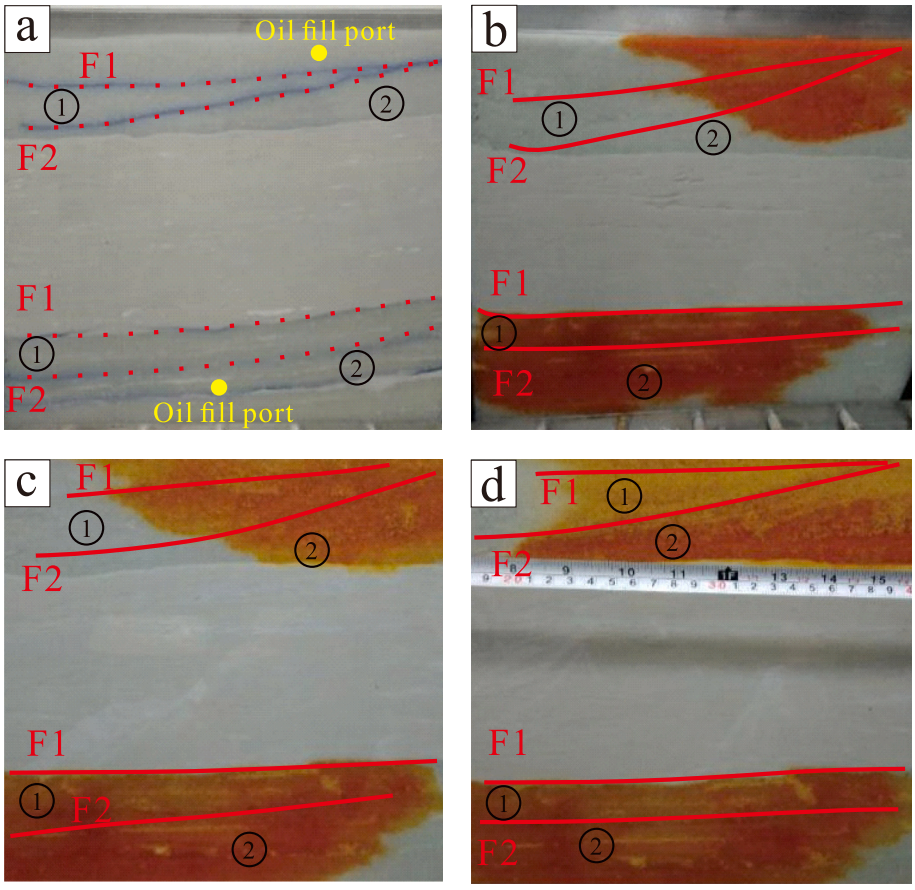

Fig. 12. Photographs of the analog experiments (Song et al., 2019).

Continued injection drove both diffusive charge into the matrix and preferential charge along bedding-parallel and high-angle fractures, with the latter pathway being markedly more efficient. Stage 3 captured secondary diffusion from kerosene-filled fractures into the adjacent tight matrix once the fracture network was saturated.

The results demonstrate the contrasting functions of the two fracture sets and the substantial impact on charging efficiency and oil saturation (Fig. 12). In domain I, where both fracture families are present, the high-angle fractures provide vertical conduits and BPFs supply lateral pathways and abundant storage, resulting in the highest charging efficiency and final oil saturation. In domain II, where only high-angle fractures exist, the oil fills the vertical conduits and then diffuses into the surrounding tight matrix. Saturation is highest near the fractures and declines with distance, and the overall saturation is lower than that of domain I. In domain III, which has only BPFs, the absence of vertical connectivity limits supply to slow, diffuse matrix charging before oil reaches the fracture-rich intervals. Collectively, high-angle fractures extend through the vertical reach, whereas dense bedding-parallel networks facilitate lateral transport and storage. Their effective coupling substantially enhances charging efficiency and the oil saturation of the reservoir.

During hydrocarbon migration and trapping, BPFs act as key heterogeneities and primary conduits (Wei et al., 2023). Unlike tectonic fractures, they are typically aligned with bedding, more pervasive, and connect intimately with primary pore systems. Lateral migration is, therefore, best described as a coupled relay along the fracture–pore network: fractures provide low-resistance pathways and pores buffer the flux and host local accumulations. During the trapping stage, this coupling becomes a joint accumulation mechanism, where fractures focus rapid convergence and charging, and pores provide the ultimate storage space (Zeng et al., 2022).

Laboratory flow experiments on tight sandstone cores with different laminations indicate the strength of this coupling (Liang et al., 2022). These experiments compared samples with well-developed BPFs, samples with laminae but no fractures, and homogeneous tight samples, with injections oriented parallel to the BPFs, at random azimuths in the homogeneous material and perpendicular to the lamination. Where BPFs were absent, oil moved only through the pore network, yielding high threshold pressure gradients and low transport efficiency. In the coupled fracture–pore system, BPFs became preferential flow paths, sharply lowering the resistance and reducing the threshold gradient. For similar porosities, the presence of BPFs increased the effective permeability by roughly a factor of 5–10 (Fig. 13), underscoring their role in enhancing flow.

Further analysis reveals that in tight lithologies such as shale, nonlinear flow along BPFs reduces the threshold pressure and enables an early transition to linear flow. This accelerates migration and extends transport distances (Liu et al., 2021). Under the main charging fluid potential, hydrocarbons preferentially enter the coupled fracture–pore network, propagate laterally along well-connected pathways, and accumulate over long distances to form effective tight reservoirs (Fig. 14).

The utility of our genetic classification and diagnostic toolkit can be illustrated by comparing two well-studied lacustrine-marine shale systems. In the Sichuan Basin (Wufeng–Longmaxi Formation), BPFs are predominantly tectonic-hydrothermal (Permian Emeishan plume-related) overprinted by late-stage unloading fractures; their high-angle intersections create complex 3D networks that dominate both stimulation and production (Liu et al., 2020). In the Junggar Basin (Lucaogou Formation), BPFs are mainly hydrocarbon-overpressure and diagenetic shrinkage types, with subordinate tectonic-hydrothermal veins linked to Permian post-collisional magmatism (Zhang et al., 2025). This

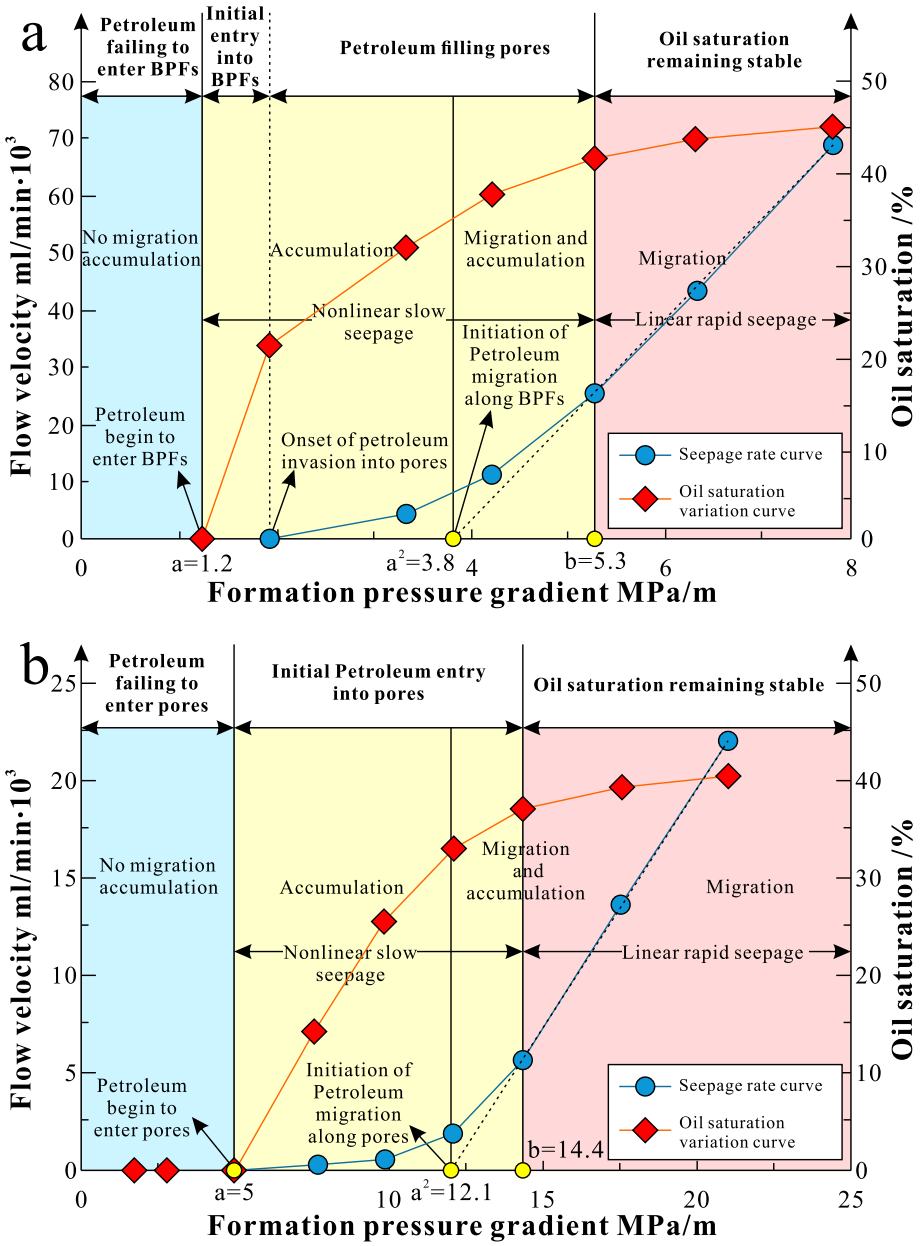

Fig. 13. Simulations of hydrocarbon migration along BPFs and through matrix pores (Li et al., 2024). (a) Hydrocarbon migration along BPFs. (b) Hydrocarbon migration through matrix pores.

comparison confirms that the principles derived from our integrated analysis are transferable across disparate geological settings, and that the four-fold genetic classification captures the essential spectrum of BPF origins globally.

Taken together, BPFs lower the entry barrier for charge into tight reservoirs and, through coupling with the pore system, greatly improve the flow capacity and transport efficiency. This highlights the composite nature of the fracture–pore systems in tight reservoirs and provides a theoretical and experimental basis for prediction in tight oil and gas plays.

5.3. Spatial and temporal configuration of BPFs and high-angle fractures: Implications for sweet spot distribution

In most shale reservoirs, BPFs and high-angle (vertical to subvertical) fractures coexist, forming a hierarchical fracture system. Their spatial and temporal configuration critically controls hydrocarbon migration and accumulation efficiency, and hence the distribution of "sweet spots" (Li et al., 2025b, 2025a; Du et al., 2025).

Where BPFs are densely developed and intersect with through-going high-angle fractures, a three-dimensional connected network is created that permits rapid vertical drainage from deep overpressured compartments and simultaneous lateral distribution across the reservoir. This configuration yields the highest oil/gas saturation and productivity. In contrast, where high-angle fractures are absent, BPFs form isolated, subhorizontal lenses that charge only by slow matrix diffusion; oil saturation is moderate and declines rapidly away from the fracture tips. Where high-angle fractures exist but BPFs are poorly developed, vertical migration dominates but lateral sweep is inefficient, resulting in narrow, chimney-like enriched zones (Ma et al., 2025).

The sequence of fracture opening is equally important. If BPFs form early (during oil window) and are subsequently connected by later high-angle fractures (formed during basin inversion or Himalayan tectonism), the earlier-formed BPFs serve as prefilled storage that is rapidly accessed

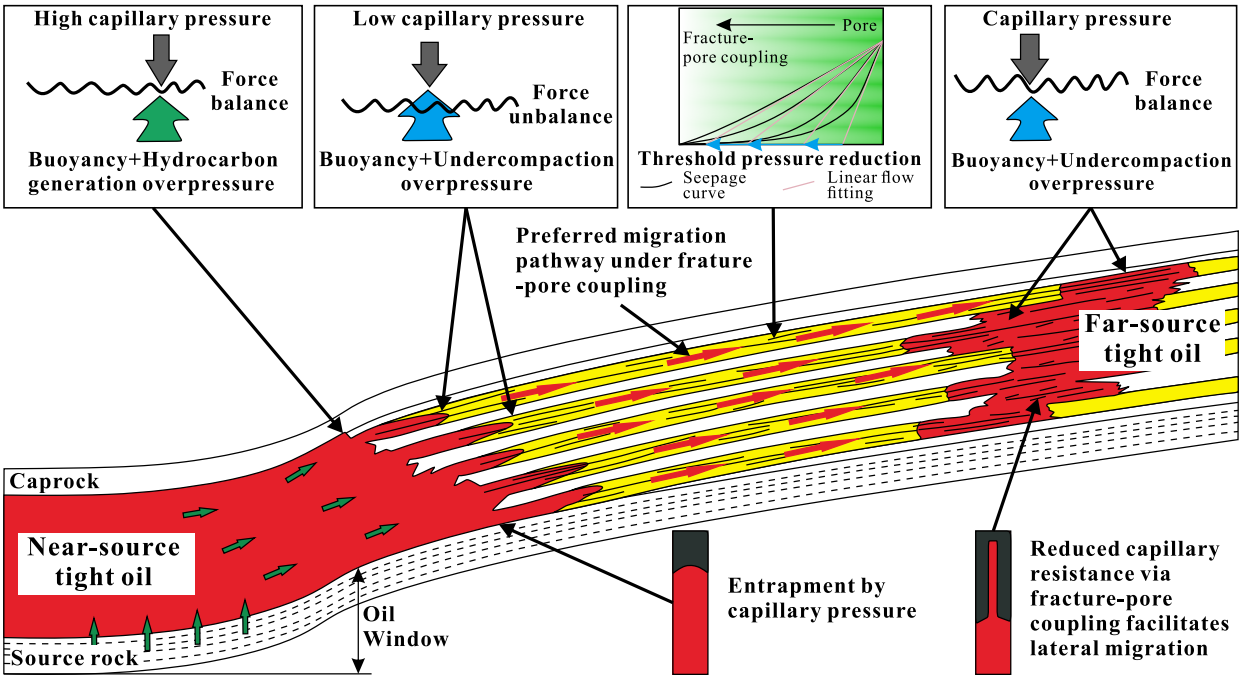

Fig. 14. Dynamic model of the influence of BPFs on lateral hydrocarbon migration and accumulation (Jia et al., 2025).

by later fractures, promoting sustained high production. Conversely, if high-angle fractures open before BPF development, they may drain hydrocarbons prematurely or become sealed by late-stage cements, reducing ultimate reserves (Zhang et al., 2024).

Sweet spot prediction therefore requires not only mapping fracture intensity, but also discriminating fracture types, quantifying their connectivity, and establishing their relative timing through integrated core-log-geochronology correlation. The genetic classification and analytical framework presented in this review provide the essential tools for such predictions.

It must be emphasized that bedding-parallel fractures alone, despite their high lateral permeability, are incapable of delivering large-scale shale hydrocarbon accumulations unless they are connected to the source kitchen or overpressure compartment by vertical or oblique fracture conduits. Analog experiments (Zhang et al., 2025) and field production data consistently show that the highest productivity wells are those intersecting both dense BPF swarms and open, through-going high-angle fractures. The latter serve as “hydrocarbon elevators” that drain overpressured intervals hundreds of meters below the reservoir and feed the laterally extensive BPF network. Without such vertical connections, BPFs merely redistribute hydrocarbons already present within the same lamina and cannot sustain flow rates.

6. Conclusions

Bedding-parallel fractures (BPFs) are among the most widespread and influential fracture systems in shale reservoirs, reflecting the strong mechanical stratification and evolving fluid–stress history of sedimentary basins. This review highlights their structural complexity, diverse origins, and fundamental importance for hydrocarbon migration, accumulation, and production.

(1) Four genetically distinct bedding-parallel fractures (BPFs) in shale are recognized: hydrocarbon fluids overpressure, tectonic, diagenetic, and unloading fractures. Hydrocarbon fluid overpressure BPFs can be identified by cemented fluids derived from hydrocarbon expulsion and are characterized by the coexistence of hydrocarbon and aqueous inclusions, chemical and isotopic compositions that are indistinguishable from those of the host shale, and ages consistent with the timing of hydrocarbon generation. Tectonic BPFs are sealed by hydrothermal or basin fluids in open systems. The hydrothermal source of the fluids is indicated by homogenization temperatures that are higher than the stratigraphic temperatures, pronounced positive Eu anomalies, and C–O–Sr isotopic compositions similar to those of magmatic–hydrothermal fluids, with cement ages coinciding with regional magmatic events. Where tectonic activity occurred in the absence of magmatism, fracture cements instead inherited the signatures of fluids from the host rock or adjacent strata under open-system conditions. In contrast, diagenetic BPFs are sealed by fluids generated during shallow burial or early diagenesis under relatively closed conditions and generally lack overprints from external hydrothermal or deep fluids; therefore, they yield similar compositions to the host-shale fluids. Unloading BPFs that formed during late-stage uplift are filled by meteoric or shallow fluids, characterized by low temperatures and weak fluid activity.

(2) Fracture-filling cements provide critical diagnostic constraints on fracture origin and timing. Petrographic fabrics, fluid inclusion assemblages, REE distributions, stable and radiogenic isotope signatures, and U–Pb/Sm–Nd ages collectively fingerprint fluid sources and basin processes. These approaches transform qualitative fracture descriptions into quantitative, testable evolutionary histories.

(3) BPFs exert first-order controls on shale reservoir permeability and hydrocarbon enrichment. Fractures can extend laterally over large distances and yield high imbibition efficiencies, acting as preferential conduits for shale oil and gas migration. Shales with well-developed fractures have higher permeabilities, and when coupled with matrix porosity during accumulation, the resulting interconnected pore–fracture architectures enable long-distance lateral transport. Consequently, BPFs not only lower the threshold pressure required for hydrocarbon charging but also substantially increase reservoir transmissivity and storage efficiency through coupling with the pore system, underpinning the high enrichment and productivity of these reservoirs.

(4) By establishing a genetic-mechanism-driven classification framework and integrating multi-scale identification methodologies, this synthesis provides actionable guidance for predicting BPF distribution and optimizing stimulation strategies in unconventional petroleum systems worldwide. Future research should prioritize integrated multiscale and multiphysics workflows. Progress will depend on combining high-resolution imaging, geochemical dating, AI-assisted fracture detection, and basin-scale mechanical–fluid modeling to predict fracture distribution, connectivity, and dynamic behavior during stimulation and production.

Declaration of competing interest

The authors declare that they have no known competing financial interests or personal relationships that could have appeared to influence the work reported in this paper.

Acknowledgments

This study was supported financially by the National Natural Science Foundation of China (42130803) and the National Key Research and Development Program of China (2022YFF0801202, 2022YFF0801200).

Appendix A. Supplementary data

Supplementary data to this article can be found online at https://doi.org/10.1016/j.earscirev.2026.105447.

Data availability

No data was used for the research described in the article.

References

Afroogh, A., Rahimi, B., Moussavi-Harami, R., Seraj, M., Wang, Q.Q., Hooker, J.N., 2019. Open fracture clustering: integrating subsurface and outcrop analogues, Asmari Formation, SW Iran. J. Struct. Geol. 125, 166–173.

Agosta, F., Luetkemeyer, P.B., Lamarche, J., Crider, J.G., Lacombe, O., 2016. Introduction to the special issue: "the role of fluids in faulting and fracturing in carbonates and other upper crustal rocks". Tectonophysics 690, 1–3.

Aguilera, R., 2014. Flow units: from conventional to tight-gas to shale-gas to tight-oil to shale-oil reservoirs. SPE Reserv. Eval. Eng. 17 (2), 190–208.

Al-Aasm, I.S., Coniglio, M., Desrochers, A., 1995. Formation of complex fibrous calcite veins in Upper Triassic strata of Wrangellia Terrain, British Columbia, Canada. Sediment. Geol. 100 (1–4), 83–95. https://doi.org/10.1016/0037-0738(95)00104-2.

Al Duhailan, M., 2014. Petroleum-expulsion fracturing in organic-rich shales: Genesis and impact on unconventional pervasive petroleum systems. Ph.D. dissertation. Colorado School of Mines, Golden, Colorado.

Anderson, G., 1981. Effects of friction on hydraulic fracture growth near unbonded interfaces in rocks. Soc. Pet. Eng. J. 21 (1), 21–29.

Ao, Y., Jia, B., Sun, C., Liu, F., 2023. Fracture characteristics and energy evolution analysis of pre-cracked granite under uniaxial compression based on a 3D-clump model. Theor. Appl. Fract. Mech. 124, 103756.

Ayuso, R.A., Kelley, K.D., Leach, D.L., Young, L.E., Slack, J.F., Wandless, J.F., Lyon, A.M., Dillingham, J.L., 2004. Origin of the red dog Zn-Pb-Ag deposits, Brooks Range, Alaska: evidence from regional Pb and Sr isotope sources. Econ. Geol. 99 (7), 1533–1553.

Azizi, H., Reza, H., 2021. Applied machine learning methods for detecting fractured zones by using petrophysical logs. Intell Control Autom 12 (2), 44–64.

Ba, J., Xu, W., Fu, L.Y., Carcione, J.M., Zhang, L., 2017. Rock anelasticity due to patchy saturation and fabric heterogeneity: A double double-porosity model of wave propagation. J. Geophys. Res. Solid Earth. 122 (3), 1949–1976.

Banner, J.L., Hanson, G.N., 1990. Calculation of simultaneous isotopic and trace element variations during water-rock interaction with applications to carbonate diagenesis. Geochim. Cosmochim. Acta 54 (11), 3123–3137.

Banner, J.L., Hanson, G.N., Meyers, W.J., 1988. Rare earth element and Nd isotopic variations in regionally extensive dolomites from the Burlington-Keokuk Formation (Mississippian); implications for REE mobility during carbonate diagenesis. J. Sediment. Res. 58 (3), 415–432.

Barker, C., 1990. Calculated volume and pressure changes during the thermal cracking of oil to gas in reservoirs. AAPG Bull 74 (8), 1254–1261.

Barker, S.L., Bennett, V.C., Cox, S.F., Norman, M.D., Gagan, M.K., 2009. Sm-Nd, Sr, C and O isotope systematics in hydrothermal calcite–fluorite veins: implications for fluid-rock reaction and geochronology. Chem. Geol. 268 (1–2), 58–66.

Becker, S.P., Eichhubl, P., Bodnar, R.J., 2010. A 48 m.y. history of fracture opening, temperature, and fluid pressure: cretaceous Travis Peak Formation, East Texas basin. Geol. Soc. Am. Bull. 122 (7–8), 1081–1093.

Bell, K., Anglin, C.D., Franklin, J.M., 1989. Sm-Nd and Rb-Sr isotope systematics of scheelites: possible implications for the age and genesis of vein-hosted gold deposits. Geology 17 (6), 500–504.

Bjørlykke, K., Jahren, J., 2012. Open or closed geochemical systems during diagenesis in sedimentary basins: constraints on mass transfer during diagenesis and the prediction of porosity in sandstone and carbonate reservoirs. AAPG Bull. 96 (12), 2193–2214.

Bons, P.D., 2000. The formation of veins and their microstructures. J. Virtual Explor. 2, 4.

Bons, P.D., 2001. The formation of large quartz veins by rapid ascent of fluids in mobile hydrofractures. Tectonophysics 336 (1–4), 1–17.

Bons, P.D., Montenari, M., 2005. The formation of antitaxial calcite veins with well-developed fibres, Oppaminda Creek, South Australia. J. Struct. Geol. 7 (2), 231–248.

Bons, P.D., Elburg, M.A., Gomez-Rivas, E., 2012. A review of the formation of tectonic veins and their microstructures. J. Struct. Geol. 43, 33–62.

Bryndzia, L.T., Macaulay, C.I., Litvinchuk, A.P., Monteleone, B.D., 2024. Origin of bedding-parallel calcite "beef" layers in the Upper Jurassic Haynesville shale, northwestern Louisiana. AAPG Bull. 108 (2), 379–400.

Buckley, S.J., Howell, J., Enge, H., Kurz, T., 2008. Terrestrial laser scanning in geology: data acquisition, processing and accuracy considerations. J. Geol. Soc. 165 (3), 625–638.

Cai, C., Li, K., Li, H., Zhang, B., 2008. Evidence for cross formational hot brine flow from integrated 87Sr/86Sr, REE and fluid inclusions of the Ordovician veins in Central Tarim, China. Appl. Geochem. 23 (8), 2226–2235.

Carpenter, S.J., Lohmann, K.C., Holden, P., Walter, L.M., Huston, T.J., Halliday, A.N., 1991. δ18O values, 87Sr86Sr and Sr/Mg ratios of late Devonian abiotic marine calcite: implications for the composition of ancient seawater. Geochim. Cosmochim. Acta 55 (7).

Chandra, J., Upadhyay, D., Patel, A.K., Mishra, B., 2024. Involvement of syn-, Para-and post-magmatic hydrothermal fluids in the alteration of the Kamthai carbonatite complex (India): insights from in-situ measured 87Sr/86Sr isotope and trace element composition of calcite. Geochemistry 84 (4), 126216.

Chemenda, A.I., 2022. Bed thickness-dependent fracturing and inter-bed coupling define the nonlinear fracture spacing-bed thickness relationship in layered rocks: Numerical modeling. J. Struct. Geol. 165, 104741.

Chen, Z., Yang, Y., Dong, C., Li, N., Wang, P., Zhang, S., Dang, W., Liao, Y., 2022. Genesis of Cambrian Dolomites in the Bachu Area, Tarim Basin, NW China: constraints from petrology, geochemistry, and fluid inclusions. Minerals 12 (9), 1157.

Chenrai, P., Assawincharoenkij, T., Warren, J., Sa-nguankaew, S., Meepring, S., Laitrakull, K., Cartwright, I., 2022. The occurrence of bedding-parallel fibrous calcite veins in permian siliciclastic and carbonate rocks in Central Thailand. Front. Earth Sci. 9, 781782.

Chi, G., Diamond, L.W., Lu, H., Lai, J., Chu, H., 2020. Common problems and pitfalls in fluid inclusion study: a review and discussion. Minerals 11 (1), 7.

Clauer, N., Techer, I., Nussbaum, C., Laurich, B., 2017. Geochemical signature of paleofluids in microstructures from Main Fault in the Opalinus Clay of the Mont Terri rock laboratory, Switzerland. Swiss J. Geosci. 110, 105–128.

Cobbold, P.R., Zanella, A., Rodrigues, N., Loseth, H., 2013. Bedding-parallel fibrous veins (beef and cone-in-cone): worldwide occurrence and possible significance in terms of fluid overpressure, hydrocarbon generation and mineralization. Mar. Pet. Geol. 43, 1–20.

Cruset, D., Vergés, J., Rodrigues, N., Belenguer, J., Pascual-Cebrian, E., Almar, Y., Pérez-Cáceres, I., Macchiavelli, C., Travé, A., Beranoaguirre, A., Albert, R., Gerdes, A., Messager, G., 2021. U-Pb dating of carbonate veins constraining timing of beef growth and oil generation within Vaca Muerta Formation and compression history in the Neuquén Basin along the Andean fold and thrust belt. Mar. Pet. Geol. 132, 105204.

Delle Piane, C., Sarout, J., Madonna, C., Saenger, E.H., Dewhurst, D.N., Raven, M., 2014. Frequency-dependent seismic attenuation in shales: Experimental results and theoretical analysis. Geophys. J. Int. 198 (1), 504–515.

Deng, W., Liang, J., Yang, Z., Kuang, Z., Yan, P., Meng, M., Zhang, Z., 2023. Fluid migration patterns in shallow horizontal sand bodies pierced by vertical gas seepage in the Qiongdongnan Basin, South China Sea. J. Asian Earth Sci. 256, 105796.

Ding, J., Clark, A.C., Vanorio, T., 2023. Integrating laboratory acoustic measurements, deep neural networks, and micro-CT imaging for characterizing rock brittle deformation. Front. Earth Sci. 11, 1052431.

Ding, W., Zhu, D., Cai, J., Gong, M., Chen, F., 2013. Analysis of the developmental characteristics and major regulating factors of fractures in marine–continental transitional shale-gas reservoirs: a case study of the Carboniferous–Permian strata in the southeastern Ordos Basin, central China. Mar. Pet. Geol. 45, 121–133.

Ding, W.L., Wang, Y., Wang, S.H., Liu, T.F., Zhang, Z.Y., Gou, T., Zhang, M.Y., He, X., 2024. Research progress and insight on non-tectonic fractures in shale reservoirs. Earth Sci. Front. 31 (1), 297–314.

Dix, G.R., Robinson, G.W., 2003. The geochemical record of hydrothermal mineralization and tectonism inboard of the Appalachian Orogen: the Ottawa Embayment. Chem. Geol. 197 (1–4), 29–53.

Dong, D., Yang, J., Hu, Q., Cui, S., Sun, F., Zhang, J., Cui, X., 2023. Pore structure characteristics of low-rank coal reservoirs with different ash yields and their implications for recoverability of coalbed methane—a case study from the Erlian Basin, northeastern China. Front. Earth Sci. 17 (1), 18–29.

Dong, H., Luo, B., Dang, C., Xu, S., Wang, F., Chi, P., 2024. Quantitative characterization of the carbonate rock microstructure considering topological features: a case study from the Gaoshiti–Moxi block of the Sichuan Basin. Front. Earth Sci. 12, 1375637.
Drake, H., Heim, C., Hogmalm, K.J., Hansen, B.T., 2014. Fracture zone-scale variation of trace elements and stable isotopes in calcite in a crystalline rock setting. Appl. Geochem. 23, 11–24.
Drake, H., Åström, M.E., Heim, C., Broman, C., Åström, J., Whitehouse, M., Lvarsson, M., Siljeström, S., Sjövall, P., 2015. Extreme 13C depletion of carbonates formed during oxidation of biogenic methane in fractured granite. Nat. Commun. 6 (1), 7020.
Du, J.Z., Cai, J.G., Long, S.X., Gao, B., Feng, D.J., Peng, Z.Y., Zeng, X., 2021. The control of diagenesis and mineral assemblages on brittleness of mudstones. Front. Earth Sci. 9, 758046.
Du, X.Y., Jin, Z.J., Zeng, L.B., Liu, G.P., Li, S.X., Ostadhassan, M., Liang, X.P., Wang, G.P., Lu, G.Q., 2025. Characteristics, controlling factors and mechanisms of natural fractures formation in lacustrine shale oil reservoirs: the Chang 7 member in Ordos Basin, China. Pet. Sci. 22 (4), 1391–1406.
Dze, S.A., Phillips, T., Najafi-Silab, R., Perez, S., Bultreys, T., Novak, V., Schlepütz, C.M., Cnudde, V., Doster, F., Singh, K., Bisdom, K., Busch, A., 2026. Analysis and comparison of natural shear and induced tensile fractures for caprock leakage assessment. Transp. Porous Media 153 (2), 29.
Edirisinghe, E.A.A.V., Perera, M.S.A., 2024. Review on the impact of fluid inertia effect on hydraulic fracturing and controlling factors in porous and fractured media. Acta Geotech. 19 (12), 7923–7965.
Elburg, M.A., Bons, P.D., Foden, J., Passchier, C.W., 2002. The origin of fibrous veins: constraints from geochemistry. Geol. Soc. London Spec. Publ. 200 (1), 103–118.
Engelder, T., 1985. Loading paths to joint propagation during a tectonic cycle: an example from the Appalachian Plateau, USA. J. Struct. Geol. 7 (3–4), 459–476.
Fall, A., Eichhubl, P., Bodnar, R.J., Laubach, S.E., Davis, J.S., 2015. Natural hydraulic fracturing of tight-gas sandstone reservoirs, Piceance Basin, Colorado. Geol. Soc. Am. Bull. 127 (1–2), 61–75.
Fan, M.-S., Ni, P., Pan, J.-Y., Wang, G.-G., Ding, J.-Y., Chu, S.-W., Li, W.-S., Huang, W.-Q., Zhu, R.-Z., Chi, Z., 2023. Rare disperse elements in epithermal deposit: Insights from LA–ICP–MS study of sphalerite at Dalingkou, South China. J. Geochem. Explor. 244, 107124.
Fan, C., Nie, S., Li, H., Radwan, A., Pan, Q., Shi, X., Li, J., Liu, Y., Guo, Y., 2024b. Quantitative prediction and spatial analysis of structural fractures in deep shale gas reservoirs within complex structural zones: a case study of the Longmaxi Formation in the Luzhou area, southern Sichuan Basin, China. J. Asian Earth Sci. 263, 106025.
Fan, Q., Liu, D., Du, W., et al., 2024a. In situ U-Pb dating of carbonate veins in Cambrian shales constrains fluid flow and hydrocarbon evolution at the southeastern margin of the Upper Yangtze platform, southwestern China. Geol. Soc. Am. Bull. 136 (7–8), 2875–2890.
Fan, S.L., He, M.C., Yao, S.Z., Ding, Z.J., 2012. Fluid inclusions and stable isotope geochemistry of Dongchuang gold deposit in western Henan: implications for genesis. Mineral. Deposita 31, 27–40.
Fang, X., Zhang, W.Q., Zhang, X.Y., Xing, Y.Z., Cheng, M.W., Tian, Y., 2016. Sedimentary facies controlled fracture quantitative interpretation of fractured carbonate gas reservoirs: a case study of the right bank of Amu Darya, Turkmenistan. Nat. Gas Geosci. 27 (8), 1549–1556.
Fanlo, I., Touray, J.C., Subías, I., Fernández-Nieto, C., 1998. Geochemical patterns of a sheared fluorite vein, Parzan, Spanish Central Pyrenees. Mineral. Deposita 33, 620–632.
Ferrill, D.A., Smart, K.J., McDonnell, S., Wyrick, D.Y., Warfel, J.R., Donahue, M.S., Morris, A.P., 2022. Contractional fold amplification through bed-parallel gypsum vein formation in the Boquillas (Eagle Ford equivalent), West Texas. J. Struct. Geol. 156, 105432.
Fisher, D.M., Brantley, S.L., 1992. Models of quartz overgrowth and vein formation: deformation and episodic fluid flow in an ancient subduction zone. J. Geophys. Res. Solid Earth 97 (B13), 20043–20061.
Forstner, S.R., Laubach, S.E., 2022. Scale-dependent fracture networks. J. Struct. Geol. 165, 104748.
Fossen, H., 2016. Structural Geology. Cambridge University Press, Cambridge, UK, pp. 480–481.
Fossen, H., Rotevatn, A., 2016. Fault linkage and relay structures in extensional settings—a review. Earth Sci. Rev. 154, 14–28.
Fu, G., Zhao, Q., Wang, G., Zou, C., Ren, Q., 2025. Integrated geomechanical modeling of multiscale fracture networks in the Longmaxi Shale Reservoir, Northern Luzhou Region, Sichuan Basin. Appl. Sci. 15 (17), 9528.
Fu, Q., Hu, Z.Q., Qin, T.T., Feng, D.J., Yang, B., Zhu, Z.W., Xing, L.L., 2023. Diagenesis and pore formation evolution of continental shale in the Da'anzhai lower Jurassic Section in the Sichuan Basin. Minerals 13 (4), 535.
Fusswinkel, T., Wagner, T., Wenzel, T., Wälle, M., Lorenz, J., 2014. Red bed and basement sourced fluids recorded in hydrothermal Mn-Fe-As veins, Sailauf (Germany): a LA-ICPMS fluid inclusion study. Chem. Geol. 363, 22–39.
Gaboury, D., Daigneault, R., 2000. Flat vein formation in a transitional crustal setting by self-induced fluid pressure equilibrium—an example from the Geant Dormant gold mine, Canada. Ore Geol. Rev. 17 (3), 155–178.
Gale, J.F., Reed, R.M., Holder, J., 2007. Natural fractures in the Barnett Shale and their importance for hydraulic fracture treatments. AAPG Bull. 91 (4), 603–622.
Gale, J.F., Laubach, S.E., Olson, J.E., Eichhubl, P., Fall, A., 2014. Natural fractures in shale: a review and new observations. AAPG Bull. 98 (11), 2165–2216.
Gale, J.F.W., Fall, A., Yurchenko, I.A., Ali, W.A., Laubach, S.E., Eichhubl, P., Bodnar, R. J., 2022. Opening-mode fracturing and cementation during hydrocarbon generation in shale: an example from the Barnett Shale, Delaware Basin, West Texas. AAPG Bull. 106 (10), 2103–2141.
Gao, J., Zhang, J., He, S., Zhao, J., He, Z., Wo, Y., Feng, Y., Li, W., 2019. Overpressure generation and evolution in lower Paleozoic gas shales of the Jiaoshiba region, China: implications for shale gas accumulation. Mar. Pet. Geol. 102, 844–859.
Gao, J., He, S., Zhao, J.X., He, Z., Wu, C., Feng, Y., Nguyen, A.D., Zhou, J., Yi, Z., 2020. Sm-Nd isochron dating and geochemical (rare earth elements, 87Sr/86Sr, δ18O, δ13C) characterization of calcite veins in the Jiaoshiba shale gas field, China: implications for the mechanisms of vein formation in shale gas systems. Geol. Soc. Am. Bull. 132 (7–8), 1722–1740.
Garum, M., Glover, P.W.J., Lorinczi, P., Drummond-Brydson, R., Hassanpour, A., 2020. Micro-and nano-scale pore structure in gas shale using Xμ-CT and FIB-SEM techniques. Energy Fuel 34 (10), 12340–12353.
Gasparrini, M., Sassi, W., Gale, J.F., 2014. Natural sealed fractures in mudrocks: a case study tied to burial history from the Barnett Shale, Fort Worth Basin, Texas, USA. Mar. Pet. Geol. 55, 122–141.
George, S.C., Ruble, T.E., Dutkiewicz, A., Eadington, P.J., 2001. Assessing the maturity of oil trapped in fluid inclusions using molecular geochemistry data and visually-determined fluorescence colours. Appl. Geochem. 16 (4), 451–473.
Gleeson, S.A., Yardley, B.D., Munz, I.A., Boyce, A.J., 2003. Infiltration of basinal fluids into high-grade basement, South Norway: sources and behaviour of waters and brines. Geofluids 3 (1), 33–48.
Gomes Jr., C.P., Santos, R.V., Vieira, L.C., Dantas, E.L., Taveira, I.P., Barbosa, P.F., Couto, D.C., Rasbury, T., Abbots, F., Bezerra, F.H., 2022. Fault zone fluid pathways in the carbonate Irecê basin, NE Brazil. Basin Res. 34 (6), 2189–2208.
Gong, L., Liu, G., Wang, R., Dong, S., Wu, Z., 2025. Editorial: distribution and development of faults and fractures in Shales. Minerals 15, 1154.
Gou, B., Wang, C., Yu, T., Wang, K., 2020. Fuzzy logic and grey clustering analysis hybrid intelligence model applied to candidate-well selection for hydraulic fracturing in hydrocarbon reservoir. Arab. J. Geosci. 13 (19), 975.
Grabezhev, A.I., 2010. The Gumeshevo skarn-porphyry copper deposits in the Central Urals, Russia: evolution of the ore-magmatic system as deduced from isotope geochemistry (Sr, Nd, C, O, H). Geol. Ore Deposits 52, 138–153.
Griffith, A.A., 1921. The phenomena of rupture and flow in solids. Philos. Trans. R. Soc. Lond. Ser. A 221 (582–593), 163–198.
Guo, J., Gurevich, B., 2020. Frequency-dependent P wave anisotropy due to wave-induced fluid flow and elastic scattering in a fluid-saturated porous medium with aligned fractures. J. Geophys. Res. Solid Earth 125 (8), e2020JB020320.
Gupta, I., Sondergeld, C., Rai, C., 2020. Fracture toughness in shales using nano-indentation. J. Pet. Sci. Eng. 191, 107222.
Hall, A.J., Banks, D., Fallick, A.E., Hamilton, P.J., 1989. An hydrothermal origin for copper-impregnated prehnite and analcime from Boylestone Quarry, Barrhead, Scotland. J. Geol. Soc. 146 (4), 701–713.
Haller, A., Tarantola, A., Mazurek, M., Spangenberg, J., 2010. Veins and related past fluid flow through the Mesozoic sedimentary cover in the Swiss Molasse Basin. Geol. Soc. Lond. Spec. Publ. 346–347.
Han, C., Lin, C., Lu, X., Tian, J., Ren, L., Ma, C., 2019. Petrological and geochemical constraints on fluid types and formation mechanisms of the Ordovician carbonate reservoirs in Tahe Oilfield, Tarim Basin, NW China. J. Pet. Sci. Eng. 178, 106–120.
He, J.H., Cao, H.X., Deng, H.C., Yin, C.H., Zhu, Y.P., Li, C., Li, Y., Yin, S., 2024. Nature fractures in shales of the Lianggaoshan Formation in northern Sichuan Basin: fracture development characteristics and fracture formation and evolution model. Earth Sci. Front. 31 (5), 017–034.
He, W., Wang, R., Lyu, Q., Liu, J., Wu, Y., 2022. Coupling relationship between densification characteristics and tight oil accumulation of the FGSR reservoir: a case study of the Chang 7 member of the Triassic Yanchang Formation in the Zhenyuan area of the Southwest Ordos Basin, Central China. Front. Earth Sci. 10, 855879.
He, Z., Duan, B., 2019. Dynamic modeling of bedding-plane slip during hydraulic fracturing. Geophysics 84 (3). KS95–KS104.
Henjes-Kunst, F., Prochaska, W., Niedermayr, A., Sullivan, N., Baxter, E., 2014. Sm-Nd dating of hydrothermal carbonate formation: an example from the Breitenau magnesite deposit (Styria, Austria). Chem. Geol. 387, 184–201.
Hilgers, C., Urai, J.L., 2002. Experimental study of syntaxial vein growth during lateral fluid flow in transmitted light: first results. J. Struct. Geol. 24 (6–7), 1029–1043.
Hilgers, C., Urai, J.L., Post, A.D., Bons, P.D., 1997. Fibrous vein microstructure: experimental and numerical simulation. Belgian Sympos. Struct. Geol. Tecton. 107–109.
Hoernle, K.A.J., 1998. Geochemistry of Jurassic oceanic crust beneath Gran Canaria (Canary Islands): implications for crustal recycling and assimilation. J. Petrol. 39 (5), 859–880.
Hooker, J.N., Laubach, S.E., 2023. Scale-dependent fracture networks. J. Struct. Geol. 165, 104748.
Hooker, J.N., Abu-Mahfouz, I.S., Meng, Q., Cartwright, J., 2019. Fractures in mudrocks: Advances in constraining timing and understanding mechanisms. J. Struct. Geol. 125, 166–173.
Hooker, J.N., Gomez, L.A., Laubach, S.E., Marrett, R.A., 2012. Effects of diagenesis (cement precipitation) during fracture opening on fracture aperture-size scaling in carbonate rocks. Geol. Soc. London Spec. Publ. 370, 187–206.
Hooker, J.N., Larson, T.E., Eakin, A., Laubach, S.E., Eichhubl, P., Fall, A., Marrett, R., 2015. Fracturing and fluid flow in a sub-décollement sandstone; or, a leak in the basement. J. Geol. Soc. Lond. 172 (4), 428–442.
Hooker, J.N., Abu-Mahfouz, I.S., Meng, Q., Cartwright, J., 2018. Fractures in mudrocks: advances in constraining timing and understanding mechanisms. J. Struct. Geol. 125, 166–173.
Horton, T.W., Blum, J.D., Craw, D., Koons, P.O., Chamberlain, C.P., 2003. Oxygen, carbon, and strontium isotopic constraints on timing and sources of crustal fluids in an active orogen: South Island, New Zealand. New Zealand J. Geol. Geophys. 46 (3), 457–471.

Hoyt, E.M., Hooker, J.N., 2020. Silica diagenesis-driven fracturing in limestone: an example from the Ordovician of Central Pennsylvania. Mar. Pet. Geol. 132, 105240.
Hurai, V., 2010. Fluid inclusion geobarometry: pressure corrections for immiscible H2O–CH4 and H2O–CO2 fluids. Chem. Geol. 278 (3–4), 201–211.
Imber, J., Armstrong, H., Clancy, S., Daniels, S., Herringshaw, L., McCaffrey, K., Rodrigues, J., Trabucho-Alexandre, J., Warren, C., 2014. Natural fractures in a United Kingdom shale reservoir analog, Cleveland Basin, Northeast England. AAPG Bull. 98 (11), 2411–2437.
Ismail, A., Radwan, A.A., Leila, M., Abdelmaksoud, A., Ali, M., 2023. Unsupervised machine learning and multi-seismic attributes for fault and fracture network interpretation in the Kerry Field, Taranaki Basin, New Zealand. Geomech. Geophys. Geo-Energy Geo-Resources 9 (1), 122.
Jia, Z.C., Jiang, L., Zhao, W., 2025. Research progress in the whole Petroleum System theory. Acta Pet. Sin. 46 (7), 1218–1307.
Jin, F., Hu, J., Yang, M., 2007. Vertical distribution of nonylphenol and nonylphenol ethoxylates in sedimentary core from the Beipaiming Channel, North China. J. Environ. Sci. 19 (3), 353–357.
Jin, J.D., Wang, L.J., Yan, Z.L., Li, G.F., Wang, J.X., 2024. Effects of strain rate and bedding on shale fracture mechanisms. Int. J. Mech. Sci. 277, 109398.
Jochum, J., Friedrich, G., Leythaeuser, D., Littke, R., Ropertz, B., 1995. Hydrocarbon-bearing fluid inclusions in calcite-filled horizontal fractures from mature Posidonia Shale (Hils Syncline, NW Germany). Ore Geol. Rev. 9 (5), 363–370.
de Jonge-Anderson, I., Ma, J., Wu, X., Stow, D.A.V., 2021. Determining reservoir intervals in the Bowland Shale using petrophysics and rock physics models. Geophys. J. Int. 228 (1), 39–54.
Katz, B.G., Bullen, T.D., 1996. The combined use of 87Sr/86Sr and carbon and water isotopes to study the hydrochemical interaction between groundwater and lakewater in mantled karst. Geochim. Cosmochim. Acta 60 (24), 5075–5087.
Lai, J., Wang, G., Wang, S., Cao, J., Li, M., Pang, X., Han, C., Fan, X., Yang, L., He, Z., Qin, Z., 2018a. A review on the applications of image logs in structural analysis and sedimentary characterization. Mar. Pet. Geol. 95, 139–166.
Lai, J., Wang, X., Qiu, J., Chen, J., Hu, Z., Wang, H., 2018b. Extreme deformation characteristics and countermeasures for a tunnel in difficult grounds in southern Shaanxi, China. Environ. Earth Sci. 77 (19), 706.
Lai, J., Liu, S., Xin, Y., Wang, S., Xiao, C., Song, Q., Chen, X., Yang, K., Wang, G., Ding, X., 2021. Geological-petrophysical insights in the deep Cambrian dolostone reservoirs in Tarim Basin, China. AAPG Bull. 105 (11), 2263–2296.
Kravchenko, O., Velighotskiy, D., Avramenko, A., Habibullin, R., 2014. An improved technology of a complex influence on productive layers of oil and gas wells. East.-Eur. J. Enterp. Technol. 6 (5), 4.
Lai, J., Liu, B.C., Li, H.B., Pang, X.J., Liu, S.C., Bao, M., Wang, G.W., 2022. Bedding parallel fractures in fine-grained sedimentary rocks: Recognition, formation mechanisms, and prediction using well log. Pet. Sci. 19 (2), 554–569.
Lander, R.H., Laubach, S.E., 2015. Insights into rates of fracture growth and sealing from a model for quartz cementation in fractured sandstones. Geol. Soc. Am. Bull. 127 (3–4), 516–538.
Laongsakul, P., Dürrast, G., 2011. Characterization of reservoir fractures using conventional geophysical logging. Songklanakarin J. Sci. Technol. 33 (2), 237–246.
Lash, G.G., Engelder, T., 2005. An analysis of horizontal microcracking during catagenesis: example from the Catskill delta complex. AAPG Bull. 89 (11), 1433–1449.
Laubach, S.E., Reed, R.M., Olson, J.E., Lander, R.H., Bonnell, L.M., 2004. Coevolution of crack-seal texture and fracture porosity in sedimentary rocks: cathodoluminescence observations of regional fractures. J. Struct. Geol. 26 (5), 967–982.
Laubach, S.E., Eichhubl, P., Hilgers, C., Lander, R.H., 2010. Structural diagenesis. J. Struct. Geol. 32 (12), 1866–1872.
Laubach, S.E., Lander, R.H., Criscenti, L.J., Anovitz, L.M., Urai, J.L., Pollyea, R.M., Hooker, J.N., Narr, W., Evans, M.A., Kerisit, S.N., Olson, J.E., Dewers, T., Fisher, D., Bodnar, R., Evans, B., Dove, P., Bonnell, M.L., Marder, M.P., Pyrak-Nolte, L., 2019. The role of chemistry in fracture pattern development and opportunities to advance interpretations of geological materials. Rev. Geophys. 57 (3), 1065–1111.
Laubach, S.E., Zeng, L.B., Hooker, J.N., Wang, Q.Q., Zhang, R.H., Wang, J.P., Ren, B., 2023. Deep and ultra-deep basin brittle deformation with focus on China. J. Struct. Geol. 175, 104938.
Lee, B., Olson, J.E., Holder, J., Gale, J.F.W., 2015. Interaction of propagating opening-mode fractures with calcite-filled veins in the Marcellus Shale. J. Geophys. Res. Solid Earth 120 (1), 169–185.
Li, H., 2022. Research progress on evaluation methods and factors influencing shale brittleness: a review. Energy Rep. 8, 4344–4358.
Li, H., Tang, H.M., Qin, Q.R., Zhou, J.L., Qin, Z.J., Fan, C.H., Su, P.D., Wang, Q., Zhong, C., 2019. Characteristics, formation periods and genetic mechanisms of tectonic fractures in the tight gas sandstones reservoir: a case study of Xujiahe Formation in YB area, Sichuan Basin, China. J. Pet. Sci. Eng. 178, 723–735.
Li, K., Xi, K.L., Cao, Y.C., Wang, Y.C., Lin, M.R., 2023b. Genesis of granular calcite in lacustrine fine-grained sedimentary rocks and its indication to volcanic-hydrothermal events: a case study of Permian Lucaogou Formation in Jimusar Sag, Junggar Basin, NW China. Pet. Explor. Dev. 50 (3), 541–552.
Li, S.H., Zhang, S.C., Zhang, X., Chen, M., Li, S.Z., Zou, Y.S., Guo, T.K., Zhou, T., Chen, Z. R., 2025b. Numerical study of hydraulic fracture propagation coupling frictional bedding planes in shale reservoirs. Comput. Geotech. 184, 107298.
Li, X., Du, W., Feng, X., Shi, F., Chen, Y., Wang, Y., Jiang, Z., Luo, Q., 2023a. Pressure evolution mechanism of marine shale reservoirs and shale gas accumulation model: evidence from fluid inclusions in the wufeng–longmaxi formation in the basin margin structural transition zone in northern Guizhou province, China. Minerals 13 (2), 241.
Li, Z., Xi, K., Niu, X., Wang, X., Ma, W., Hui, X., Liu, J., Fan, C., Lin, M., Liu, K., Cao, Y., 2025a. How bedding-parallel fractures affect fluid activity in a relatively closed lacustrine shales system: evidence from calcite veins. Mar. Pet. Geol. 173, 107276.
Li, Z.L., Fan, C.Y., Hui, X., Deng, X.Q., Sun, B., Han, X.J., Wang, A.G., Wang, G., 2024. Research progress and trend of bedding-parallel fractures in unconventional sedimentary reservoirs. J. Sediment. Res. 42 (4), 1150–1163.
Li, Z.N., 2018. The Relevant to the Interaction between Characteristic of Bedding Fracture and Oil Charging in Lucaogou Formation, Jimusar sag. China University of Petroleum (Beijing).
Liang, C., Liu, A., Luo, Q., et al., 2022. Differences in imbibition efficiency between bedding and tectonic fractures in the Lucaogou formation in the Jimusar Sag: evidence from simulation experiments. Front. Earth Sci. 10, 918244.
Lines, A., Thoeni, K., Buzzi, O., Giacomini, A., 2025. Characterising stiffness properties of bedding parallel fractures at high normal stresses for sedimentary rocks. Rock Mech. Rock. Eng. 1–20.
Liu, D., Dai, J., Xiao, X., Tian, H., Yang, C., Hu, A., Mi, J., Song, Z., 2009. High density methane inclusions in Puguang Gasfield: discovery and a TP genetic study. Chin. Sci. Bull. 54 (24), 4714–4723.
Liu, D., Ge, H., Shen, Y., Liu, H., Zhang, Y., 2021. Experimental investigation on imbibition characteristics of shale with highly developed bedding fractures. J. Nat. Gas Sci. Eng. 96, 104244.
Liu, D., Tian, H., Jia, C., Fan, Q., Lu, X., Xu, M., Song, Y., Zhang, C., 2024b. Calcite UPb dating and geochemical constraints on fracture opening in organic-rich shales. Int. J. Coal Geol. 294, 104621.
Liu, D.D., Zhang, C., Pan, Z.K., Huang, Z.X., Luo, Q., Song, Y., Jiang, Z.X., 2020. Natural fractures in carbonate-rich tight oil reservoirs from the Permian Lucaogou Formation, southern Junggar Basin, NW China: insights from fluid inclusion microthermometry and isotopic geochemistry. Mar. Pet. Geol. 119, 104500.
Liu, G., Shang, D., Zhao, Y., Du, X., 2024a. Characterisation of brittleness index of gas shale and its influence on favorable block exploitation in Southwest China. Front. Earth Sci. 12, 1389378.
Liu, G., Jin, Z., Zeng, L., Chen, X., Ostadhassan, M., Wang, Q., Lu, G., Du, X., 2025. Laminar controls on bedding-parallel fractures in Permian lacustrine shales, Junggar Basin, northwestern China. Geol. Soc. Am. Bull. 137 (7–8), 3512–3526.
Liu, H.P., Zhang, C.M., Zhang, L., Luo, Y., 2022. Bedding-parallel fractures in ultradeep tight sandstone reservoirs in Jurassic and cretaceous of Yongjin Oil Field, Junggar Basin, China. Front. Earth Sci. 16 (4), 975–988.
Liu, J., Ding, W., Wang, R., Yin, S., Yang, H., Gu, Y., 2017a. Simulation of paleotectonic stress fields and quantitative prediction of multi-period fractures in shale reservoirs: a case study of the Niutitang Formation in the lower Cambrian in the Cen'gong block, South China. Mar. Pet. Geol. 84, 289–310. https://doi.org/10.1016/j.marpetgeo.2017.04.004.
Liu, J., Li, Z., Cheng, L., Li, J., 2017b. Multiphase calcite cementation and fluids evolution of a deeply buried carbonate reservoir in the Upper Ordovician Lianglitag Formation, Tahe Oilfield, Tarim Basin, NW China. Geofluids 2017 (1), 4813235.
Liu, K.Q., Ostadhassan, M., 2017. Microstructural and geomechanical analysis of Bakken shale at nanoscale. J. Pet. Sci. Eng. 153, 133–144.
Loucks, R.G., Reed, R.M., Ruppel, S.C., Jarvie, D.M., 2009. Morphology, genesis, and distribution of nanometer-scale pores in siliceous mudstones of the Mississippian Barnett Shale. J. Sediment. Res. 79 (12), 848–861.
Louvel, M., Etschmann, B., Guan, Q., Testemale, D., Brugger, J., 2022. Carbonate complexation enhances hydrothermal transport of rare earth elements in alkaline fluids. Nat. Commun. 13 (1), 1456.
Lu, G.Q., Zeng, L.B., Liu, G.P., Chen, X.X., Ostadhassan, M., Du, X.Y., Chen, Y.K., 2024. Subsurface natural fracture identification using an integrated ensemble learning method. IEEE Trans. Geosci. Remote Sens. 63, 4700716.
Lu, J., Zhang, C., Zeng, J., Yuan, H., 2021. Research on the oil-bearing difference of bedding fractures: a case study of Lucaogou Formation in Jimsar Sag. Geofluids 2021 (1), 5567491.
Luo, T., Guo, X., Shu, Z., Bao, H., He, S., Qing, Z., Xiao, Z., 2021. Fluid source and formation time of fracture veins of Wufeng Formation and Longmaxi Formation in the south of Jiaoshiba area, Sichuan Basin. Acta Pet. Sin. 42 (5), 611–622. https://doi.org/10.7623/syxb202105005.
Lv, M.K., Guo, T.K., Chen, M., Liu, Y.Z., Yang, X., Qu, Z.Q., Dai, C.L., 2025. Review of proppant flowback after hydraulic fracturing: research, control, and prediction methods. Geoenergy Sci. Eng. 246, 213651.
Ma, Y., Hu, Q.H., Xu, J.B., Feng, B.H., Jiang, F.J., Wang, Y.S., Huang, H.P., 2025. Multidisciplinary characterization of migrated bitumen enrichment and pore network development in low-maturity Es4 shales of the Damintun Sag, East China. Mar. Pet. Geol. 182, 107559.
Ma, Z., Tan, J., Zheng, L., Shen, B., Wang, Z., Shahzad, A., Jan, I., Schulz, H., 2021. Evaluating gas generation and preservation of the Wufeng-Longmaxi Formation shale in southeastern Sichuan Basin, China: implications from semiclosed hydrous pyrolysis. Mar. Pet. Geol. 129, 105102.
Mangenot, X., Larmier, S., Girard, J.-P., Dyja-Person, V., 2023. Diagenetic history of calcite fractures in Vaca Muerta shales (Argentina) inferred from paired Δ47 and fluid inclusion geothermometry. Mar. Pet. Geol. 160 (21), 106630.
Meng, Q., Hao, F., Tian, J., 2021. Origins of non-tectonic fractures in shale. Earth Sci. Rev. 222, 103825.
Meng, Q.F., Hooker, J., Cartwright, J., 2018. Role of pressure solution in the formation of bedding-parallel calcite veins in an immature shale (cretaceous, southern UK). Geol. Mag. 156 (5), 918–934.
Mishra, A., Jyoti, A., Haese, R.R., 2022. Irida: a machine learning based code for the automated derivation of site-specific rock type logs and their properties using Kimeleon colourlith image logs. Appl. Comp. Geosci. 16, 100102.

Mohammad, N., Hossein, F., MiriHelge, H., 2018. Effect of CO_2 phase states and flow rate on salt precipitation in shale caprocks—A microfluidic study. Environ. Sci. Technol. 52 (10), 6050–6060.
Morishita, Y., Takeno, N., 2010. Nature of the ore-forming fluid at the Quaternary Noya gold deposit in Kyushu, Japan. Resour. Geol. 60 (4), 359–376.
Morley, C.K., Nelson, R.A., Patton, T.L., Munn, S.G., 1990. Transfer zones in the East African rift system and their relevance to hydrocarbon exploration in rifts. AAPG Bull. 74, 1234–1253. https://doi.org/10.1306/0C9B2475-1710-11D7-8645000102C1865D.
Morohashi, K., Okamoto, A., Satish-Kumar, M., Tsuchiya, N., 2008. Variations in stable isotope compositions (δ13C, δ18O) of calcite within exhumation-related veins from the Sanbagawa metamorphic belt. J. Mineral. Petrol. Sci. 103 (5), 361–364.
Moussa, N., Grassineau, N.V., Asael, D., Fouquet, Y., Le Gall, B., Rolet, J., Etoubleau, J., Delacourt, C., 2019. Mineralogy, fluid inclusions and stable isotope study of epithermal Au-Ag-Bi-Te mineralization from the SE Afar Rift (Djibouti). Ore Geol. Rev. 111, 102916.
Mozley, P., Hoernle, K., 1990. Geochemistry of carbonate cements in the Sag River and Shublik Formations (Triassic/Jurassic), North Slope, Alaska: implications for the geochemical evolution of formation waters. Sedimentology 37 (5), 817–836.
Nadeau, O., Stevenson, R., Jébrak, M., 2018. Interaction of mantle magmas and fluids with crustal fluids at the 1894 Ma Montviel alkaline-carbonatite complex, Canada: insights from metasomatic and hydrothermal carbonates. Lithos 296, 563–579.
Nandakumar, V., Shivapriya, S., Thankan, S., 2024. Utility of fluid inclusion paleo-temperature in petroleum system modelling: a case study from western offshore, India. Energy Geosci. 5 (2), 100256.
Nardini, N., Muñoz-López, D., Cruset, D., Cantarero, I., Martín-Martín, J.D., Benedicto, A., Gomez-Rivas, E., John, C.M., Travé, A., 2019. From early contraction to post-folding fluid evolution in the frontal part of the Bóixols thrust sheet (southern Pyrenees) as revealed by the texture and geochemistry of calcite cements. Minerals 9 (2), 117.
Nasim, M.Q., Maiti, T., Mosavat, N., Grech, P.V., Singh, T., Roy, P.N.S., 2025. Automated detection of geological features: leveraging deep learning for beddings and fractures identification in image logs. SPE J. 1–19.
Nelson, R.A., 2001. Geologic Analysis of Naturally Fractured Reservoirs, Second edition. Gulf Professional Publishing.
Nelson, R.A., Moldovanyi, E.P., Matcek, C.C., Azpiritxaga, I., Bueno, E., 2000. Production characteristics of the fractured reservoirs of the La Paz field, Maracaibo Basin, Venezuela. AAPG Bull. 84 (11), 1791–1809.
Nishiwaki, T., Lin, A.M., 2019. Fractures and subsidiary faults developed in the active strike-slip Nojima fault zone, Japan, and tectonic implications. Tectonics 38 (12), 4290–4300.
Niu, Y., Wang, E., Li, Z., Li, B., Gao, F., Liu, X., Zhang, Z., Deng, Q., Long, Z., Wang, M., Wang, J., Gao, L., Zhang, X., 2024. Study on electric potential response's spatial distribution characteristics to damaging localization evolution of gas-bearing coal under load. Bull. Eng. Geol. Environ. 83 (1), 40.
Oliver, N.H., Bons, P.D., 2001. Mechanisms of fluid flow and fluid–rock interaction in fossil metamorphic hydrothermal systems inferred from vein–wallrock patterns, geometry and microstructure. Geofluids 1 (2), 137–162.
Olson, J.E., Laubach, S.E., Lander, R.H., 2009. Natural fracture characterization in tight gas sandstones: Integrating mechanics and diagenesis. AAPG Bull. 93 (11), 1535–1549.
Osborne, M.J., Swarbrick, R.E., 1997. Mechanisms for generating overpressure in sedimentary basins: a reevaluation. AAPG Bull. 81 (6), 1023–1041.
Peacock, D.C.P., 1997. Bedding-plane slip in initial stages of fault-related folding. J. Struct. Geol. 19 (3–4), 567–581.
Peacock, D.C.P., Knipe, R.J., Sanderson, D.J., 2000. Glossary of normal faults. J. Struct. Geol. 22, 291–305. https://doi.org/10.1016/S0191-8141(00)80102-9.
Peyaud, J.B., Pagel, M., Cabrera, J., Pitsch, H., 2006. Mineralogical, chemical and isotopic perturbations induced in shale by fluid circulation in a fault at the Tournemire experimental site (Aveyron, France). J. Geochem. Explor. 90 (1–2), 9–23.
Phan, T.T., Gardiner, J.B., Capo, R.C., Stewart, B.W., 2018. Geochemical and multi-isotopic (87Sr/86Sr, 143Nd/144Nd, 238U/235U) perspectives of sediment sources, depositional conditions, and diagenesis of the Marcellus Shale, Appalachian Basin, USA. Geochim. Cosmochim. Acta 222, 187–211.
Ping, H., Chen, H., George, S.C., Li, C., Hu, S., 2019. Relationship between the fluorescence color of oil inclusions and thermal maturity in the Dongying Depression, Bohai Bay Basin, China: part 1. Fluorescence evolution of oil in the context of hydrous pyrolysis experiments with increasing maturity. Mar. Pet. Geol. 100, 1–19.
Prosser, D.J., Daws, J.A., Fallick, A.E., Williams, B.P.J., 1993. Geochemistry and diagenesis of stratabound calcite cement layers within the Rannoch Formation of the Brent Group, Murchison Field, North Viking Graben (northern North Sea). Sediment. Geol. 87 (3–4), 139–164.
Quandt, D., Micheuz, P., Kurz, W., Kluge, T., Boch, R., Hippler, D., Krenn, K., Hauzenberger, C.A., 2019. Geochemistry of vein calcites hosted in the Troodos Pillow Lavas and their implications for the timing and physicochemical environment of fracturing, fluid circulation, and vein mineral growth. Geochem. Geophys. Geosyst. 20 (12), 5913–5938.
Quandt, D., Kurz, W., Micheuz, P., 2021. Post-magmatic fracturing, fluid flow, and vein mineralization in supra-subduction zones: a comparative study on vein calcites from the Troodos ophiolite and the Izu–Bonin forearc and rear arc. Int. J. Earth Sci. 110 (2), 627–649.
Ramsay, J.G., 1980. The crack–seal mechanism of rock deformation. Nature 284 (5752), 135–139.
Ravier, E., Martinez, M., Pellenard, P., Zanella, A., Tupinier, L., 2020. The milankovitch fingerprint on the distribution and thickness of bedding-parallel veins (beef) in source rocks. Mar. Pet. Geol. 122, 104643.
Ren, M., Wang, Z., Jiang, Q., 2021. Origin and evolution of paleofluid of the Middle Permian Maokou Formation in Southern Sichuan Basin. In: 82nd EAGE Annual Conference & Exhibition, vol. 2021, No. 1. European Association of Geoscientists & Engineers, pp. 1–5.
Ren, Q., Jin, Q., Feng, J., Li, M., 2019. Simulation of stress fields and quantitative prediction of fractures distribution in upper Ordovician biological limestone formation within Hetianhe field, Tarim Basin, NW China. J. Pet. Sci. Eng. 173, 1236–1253. https://doi.org/10.1016/j.petrol.2018.10.081.
Rieger, P., Magnall, J.M., Gleeson, S.A., Oelze, M., Wilke, F.D., Lilly, R., 2022. Differentiating between hydrothermal and diagenetic carbonate using rare earth element and yttrium (REE+Y) geochemistry: a case study from the Paleoproterozoic George Fisher massive sulfide Zn deposit, Mount Isa, Australia. Mineral. Deposita 57 (2), 187–206.
Roberts, N.M., Walker, R.J., 2016. U-Pb geochronology of calcite-mineralized faults: absolute timing of rift-related fault events on the Northeast Atlantic margin. Geology 44 (7), 531–534.
Rodrigues, N., Cobbold, P.R., Loseth, H., Ruffet, G., 2009. Widespread bedding-parallel veins of fibrous calcite ('beef') in a mature source rock (Vaca Muerta Fm, Neuquén Basin, Argentina): evidence for overpressure and horizontal compression. J. Geol. Soc. Lond. 166 (4), 695–709.
Rybalcenko, K., 2017. Gas Flow Measurements in Shales: Laboratory, Field and Numerical Investigations. University of Leeds (PhD thesis).
Ryder, R.T., Crangle Jr., R.D., Trippi, M.H., Swezey, C.S., Lentz, E.E., Rowan, E.L., Hope, R.S., 2009. Geologic cross section D-D' through the Appalachian Basin from the Findlay Arch, Sandusky County, Ohio, to the Valley and Ridge Province, Hardy County, West Virginia. In: Scientific Investigations Map, 3067. U.S. Geological Survey, Reston, Virginia, pp. 52–pp.
Ryder, R.T., Swezey, C.S., Crangle, R.D., Trippi, M.H, 2008. Geologic cross section E-E' through the Appalachian Basin from the Findlay Arch, Wood County, Ohio, to the Valley and Ridge Province, Pendleton County, West Virginia. In: Scientific Investigations Map 2985. U.S. Geological Survey, Reston, Virginia.
Ryder, R.T., Trippi, M.H., Swezey, C.S., Crangle Jr., R.D., Hope, R.S., Rowan, E.L., Lentz, E.E., 2012. Geologic cross section C-C' through the Appalachian Basin from Erie County, north-central Ohio, to the Valley and Ridge Province, Bedford County, south-central Pennsylvania. In: Scientific Investigations Map, 3172. U.S. Geological Survey, Reston, Virginia.
Sahoo, J., Sahoo, P.R., Khan, I., Venkatesh, A.S., 2022. Insights into the metallogenesis of the felsic volcanic hosted Mundiyawas-Khera Cu deposit, Alwar Basin, Western India. Minerals 12 (3), 370.
Sanderson, D.J., Peacock, D.C.P., Nixon, C.W., 2024. Fracture sets and sequencing. Earth-Sci. Rev. 257, 104888.
Savelieva, G.N., Bortnikov, N.S., Bayanova, T.B., Ikorskii, S.V., Kamenskii, I.L., 2008. Sm-Nd and Rb-Sr isotopic systems and captured He and hydrocarbon gases as markers of melt sources and fluid regime under which the oceanic crust of the Mid-Atlantic Ridge was formed at 5°-6° N. Geochem. Int. 46, 745–758.
Schaltegger, U., Stille, P., Rais, N., Piqué, A., Clauer, N., 1994. Neodymium and strontium isotopic dating of diagenesis and low-grade metamorphism of argillaceous sediments. Geochim. Cosmochim. Acta 58 (5), 1471–1481.
Schneider, J., Boni, M., Lapponi, F., Bechstädt, T., 2002. Carbonate-hosted zinc-lead deposits in the lower Cambrian of Hunan, South China: a radiogenic (Pb, Sr) isotope study. Econ. Geol. 97 (8), 1815–1827.
Schwarzenbach, E.M., Vogel, M., Früh-Green, G.L., Boschi, C., 2021. Serpentinization, carbonation, and metasomatism of ultramafic sequences in the Northern Apennine Ophiolite (NW Italy). J. Geophys. Res. Solid Earth 126 (5), e2020JB020619.
Shang, X., Zhao, H., Long, S., Duan, T., 2021. A workflow for integrated geological modeling for shale gas reservoirs: a case study of the Fuling Shale Gas Reservoir in the Sichuan Basin, China. Geofluids 2021 (1), 6504831.
Slobodník, M., Muchez, P., Král, J., Keppens, E., 2006. Variscan veins: record of fluid circulation and Variscan tectonothermal events in Upper Palaeozoic limestones of the Moravian Karst, Czech Republic. Geol. Mag. 143 (4), 491–508.
Smith, A.P., Fischer, M.P., Evans, M.A., 2014. On the homogeneity of fluids forming bedding-parallel veins. Geofluids 14 (1), 45–57.
Song, K.H., 2019. Oil-Bearing Differences and Oil-Accumulating Models of Bedding Fractures of Lucaogou Formation in Jimsar Sag. China University of Petroleum (Beijing).
Su, A., Chen, H., Feng, Y.X., Zhao, J.X., Nguyen, A.D., 2022. Multistage fracturing history in the Paleocene lacustrine shale oil reservoirs of the Subei Basin, Eastern China. Mar. Pet. Geol. 144, 105835.
Su, X.C., Zhu, R.K., Zhang, J.Y., Liu, C., Gong, L., Jiang, X.H., Fu, X.F., Ostadhassan, Mehdi, 2025. Multi-scale characterization and control factors of bedding-parallel fractures in continental shale reservoirs: Insights from the Qingshankou Formation, Songliao Basin, China. Mar. Pet. Geol. 182, 107580.
Suchy, V., Dobes, P., Filip, J., Stejskal, M., Zeman, A., 2002. Conditions for veining in the Barrandian Basin (lower Palaeozoic), Czech Republic: evidence from fluid inclusion and apatite fission track analysis. Tectonophysics 348 (1–3), 25–50.
Sun, N., He, W., Zhong, J., Gao, J., Chen, T., Swennen, R., 2023. Widespread development of bedding-parallel calcite veins in medium–high maturity organic-rich lacustrine shales (Upper cretaceous Qingshankou Formation, Northern Songliao Basin, NE China):i for hydrocarbon generation and horizontal compression. Mar. Pet. Geol. 158, 106544.
Sun, Y.Z., Pang, S.C., Qiu, Z.H., Zhang, Y.A., 2025a. Efficient lithology classification from small-sample well logging data processed by wavelet thresholding algorithm:

integrating meta-learning with self-attention mechanism model. Geoenergy Sci. Eng. 246, 213629.
Sun, Z.Y., Xu, S.Y., Ma, C.F., Li, T., Zhang, J.C., Zeng, F.C., 2025b. Shale fracture prediction using integrated seismic methods. Mar. Pet. Geol. 179, 107439.
Taylor, H.P., 1974. The application of oxygen and hydrogen isotope studies to problems of hydrothermal alteration and ore deposition. Econ. Geol. 69 (6), 843–883.
Tingay, M.R.P., Morley, C.K., Laird, A., Limpornpipat, O., Krisadasima, K., Pabchanda, S., Macintyre, H.R., 2013. Evidence for overpressure generation by kerogen-to-gas maturation in the northern Malay Basin. AAPG Bull. 97 (4), 639–672.
Torres, M.F., Morales, A., Yu, W., Miao, J., 2021. Characterization of complex hydraulic fractures in Eagle Ford shale oil development through embedded discrete fracture modeling. Pet. Explor. Dev. 48 (3), 713–720.
Urai, J.L., Williams, P.F., Van Roermund, H.L.M., 1991. Kinematics of crystal growth in syntectonic fibrous veins. J. Struct. Geol. 13 (7), 823–836.
Uysal, I.T., Zhao, J.X., Golding, S.D., Lawrence, M.G., Glikson, M., Collerson, K.D., 2007. Sm-Nd dating and rare-earth element tracing of calcite: implications for fluid-flow events in the Bowen Basin, Australia. Chem. Geol. 238 (1–2), 63–71.
Veizer, J., 1989. Strontium isotopes in seawater through time. Annu. Rev. Earth Planet. Sci. 17, 141.
Virgo, S., Ankit, K., Nestler, B., Urai, J.L., 2016. Towards an integrated numerical simulator for crack-seal vein microstructure: Coupling phase-field with the Discrete Element Method. In: EGU General Assembly Conference Abstracts, pp. EPSC2016-8250.
Voicu, G., Bardoux, M., Stevenson, R., Jebrak, M., 2000. Nd and Sr isotope study of hydrothermal scheelite and host rocks at Omai, Guiana Shield: implications for ore fluid source and flow path during the formation of orogenic gold deposits. Mineral. Deposita 35, 302–314.
Wang, M., 2016. The Formation Mechanism of the Calcite Veins in Deep Hydrocarbon Source Rocks in the Dongying Depression and their Implications. China University of Petroleum (East China).
Wang, M., Chen, Y., Xu, X., Zhang, X., Han, Y., Wang, C., Cao, M., 2015. Progress on formation mechanism of the fibrous veins in mudstone and its implications to hydrocarbon migration. Adv. Earth Science 30 (10), 1107–1118.
Wang, Q., Gale, J.F.W., 2023. Aperture size distribution, length, and preferential location of bed-parallel veins in shale. J. Struct. Geol. 177, 104984.
Wang, Q.Q., Narr, W., Laubach, S.E., 2023. Quantitative characterization of fracture spatial arrangement and intensity in a reservoir anticline using horizontal wellbore image logs and an outcrop analogue. Mar. Pet. Geol. 152, 106238.
Wang, D., Wang, X., Ge, H., Sun, D., Yu, B., 2020. Insights into the effect of spontaneous fluid imbibition on the formation mechanism of fracture networks in brittle shale: An experimental investigation. ACS Omega 5 (15), 8847–8857.
Wang, S., Wang, G.W., Zeng, L.B., Liu, P., Huang, Y.Y., Li, S.Q., Wang, Z.S., Zhou, Y.L., 2025. New method for logging identification of natural fractures in shale reservoirs: the Fengcheng formation of the Mahu Sag, China. Mar. Pet. Geol. 176, 10457346.
Wang, X., Hu, W., Qiu, Y., Liu, Y., Jia, D., Cao, J., Liu, X., Li, Y., 2022. Fluid inclusion evidence for extreme overpressure induced by gas generation in sedimentary basins. Geology 50 (7), 765–770. https://doi.org/10.1130/G49848.1.
Wang, Y., Feng, W.K., Hu, R.L., Li, C.H., 2021. Fracture evolution and energy characteristics during marble failure under triaxial fatigue cyclic and confining pressure unloading (FC-CPU) conditions. Rock Mech. Rock. Eng. 54 (2), 799–818.
Warmada, I.W., Lehmann, B., Simandjuntak, M., Hemes, H.S., 2007. Fluid inclusion, rare-earth element and stable isotope study of carbonate minerals from the Pongkor epithermal gold-silver deposit, West Java, Indonesia. Resour. Geol. 57 (2), 124–135.
Wei, J., Zhang, A., Li, J., et al., 2023. Study on microscale pore structure and bedding fracture characteristics of shale oil reservoir. Energy 278, 127829.
Williams, R.T., Goodwin, L.B., Mozley, P.S., 2017. Diagenetic controls on the evolution of fault-zone architecture and permeability structure: implications for episodicity of fault-zone fluid transport in extensional basins. Geol. Soc. Am. Bull. 129 (3–4), 464–478.
Williams, P., Urai, J., 1989. Curved vein fibres: an alternative explanation. Tectonophysics 158 (1–4), 311–333.
Wiltschko, D.V., Morse, J.W., 2001. Crystallization pressure versus “crack seal” as the mechanism for banded veins. Geology 29 (1), 79–82.
Wind, S.C., Hannington, M.D., Schneider, D.A., Fietzke, J., Kilias, S.P., Bruce Gemmell, J., 2023. Origin of hydrothermal barite in polymetallic veins and carbonate-hosted deposits of the Cyclades Continental Back Arc. Econ. Geol. 118 (8), 1959–1994.
Wu, A., Cao, J., Zhang, J., 2021. Bedding-parallel calcite veins indicate hydrocarbon-water-rock interactions in the over-mature Longmaxi shales, Sichuan Basin. Mar. Pet. Geol. 133, 105303.
Wu, J.W., Zhang, J., Lyu, Y.M., 2025b. Characterization of natural fractures and in-situ stress in high-steep coal-bearing strata in the Midong area in Xinjiang and influence on engineering. Coal Science and Technology 53 (3), 226–237.
Wu, J., Fan, T., Gomez-Rivas, E., Travé, A., Cao, Q., Gao, Z., Wang, S., Kang, Z., 2022. Impact of diagenesis on the pore evolution and sealing capacity of carbonate cap rocks in the Tarim Basin, China. AAPG Bull 106 (12), 2471–2511.
Wu, X., Liu, W., Han, S., Zou, X., Zhang, M., Luo, Y., 2025a. Effect of alternating high-and low-viscosity fracturing fluids on fracture propagation in bedding-parallel wellbores under true triaxial stress. Rock Mech. Rock. Eng. 1–11.
Wu, Z., Wu, Y., Weng, L., Li, M., Wang, Z., Chu, Z., 2024. Machine learning approach to predicting the macro-mechanical properties of rock from the meso-mechanical parameters. Comput. Geotech. 166, 105933.
Yan, J.P., Luo, J.C., Shi, X.W., Zhong, G.H., Zheng, M.J., Huang, Y., Tang, H.M., Hu, Q. H., 2022. Fracture development models and significance of Ordovician Wufeng-Silurian Longmaxi shale in Luzhou area, southern Sichuan Basin. Lith. Res. 34 (6), 60–71.
Yang, X., He, S., He, Z., Wang, F., Li, T., 2013. Characteristics and pale-fluid activity implications of fluid-inclusion and isotope of calcite veins in Jingshan area. J. China Univ. Pet. 37 (1), 19–26.
Yu, X., Wang, C., Liu, C., Wang, J., Shen, L., 2023. Geochronology, geochemistry, fluid inclusion and C, O isotope compositions of calcite veins in the Paleogene of the Jiangling Basin, South China: Implications for fluid evolution and brine potash mineralization. Acta Geol. Sin. Engl. Ed. 97 (2), 513–525.
Yuan, Y., 2022. The Relationship between Fracture and Vein Characteristics and Hydrocarbon of Fengcheng Formation in Hashan Area. China University of Petroleum (East China).
Zahid, M.A., Chunmei, D., Lin, C., Gluyas, J., Jones, S., Zhang, X., Ma, C., 2016. Sequence stratigraphy, sedimentary facies and reservoir quality of Es4s, southern slope of Dongying Depression, Bohai Bay Basin, East China. Mar. Pet. Geol. 77, 448–470. https://doi.org/10.1016/j.marpetgeo.2016.06.026.
Zanella, A., Ruiz, R., Varela, A.N., Arregui, M.G., 2024. Trace fossils as mechanical discontinuities in shales, insight for the generation of bedding-parallel veins (BPV). Sci. Rep. 14, 12746.
Zeng, L., Gong, L., Guan, C., Zhang, B., Wang, Q., Zeng, Q., Lyu, W., 2022. Natural fractures and their contribution to tight gas conglomerate reservoirs: a case study in the northwestern Sichuan Basin, China. J. Pet. Sci. Eng. 210, 110028.
Zeng, L.B., Gong, L., Zhang, Y.Z., Dong, S.Q., Lyu, W.Y., 2023. A review of the genesis, evolution, and prediction of natural fractures in deep tight sandstones of China. AAPG Bull. 107 (10), 1687–1721.
Zhang, B., Yin, C., Gu, Z., Zhang, J., Yan, S., Wang, Y., 2015. New indicators from bedding-parallel beef veins for the fault valve mechanism. Sci. China Earth Sci. 58, 1320–1336.
Zhang, C., Wen, H., Wang, X., Wen, L., Shen, A., Zhou, G., Wang, Q., She, M., Ma, C., Qiao, Z., Liu, D., Ma, Y., 2024. Formational stages of natural fractures revealed by U-Pb dating and CO-Sr-Nd isotopes of dolomites in the Ediacaran Dengying Formation, Sichuan Basin, Southwest China. Geol. Soc. Am. Bull. 136 (11–12), 4671–4688.
Zhang, C., Kong, X., Wang, Q., She, M., Liang, F., Dong, Y., Xu, H., He, J., Chen, H., 2025. Mechanisms of bedding fracturing in the Junggar Basin, Northwest China: constraints from in situ U-Pb dating and CO-Nd isotopic analysis of calcite cements. Geol. Soc. Am. Bull. 137 (7–8), 3037–3054.
Zhang, J., Yu, Q., Li, Y., Pan, Z., Liu, B., 2023. Hydraulic fracture vertical propagation mechanism in interlayered brittle shale formations: an experimental investigation. Rock Mech. Rock. Eng. 56 (1), 199–220.
Zhang, Y., Zhang, S., Huang, B., Lu, Z., Ye, N., Zhu, B., Hou, X., Xie, F., Bai, X., Zhang, X., 2022. Fluid inclusion, isotopic, and elemental geochemistry studies of cave-filling calcite in the lower-middle Ordovician Yingshan formation of Tahe oilfield, NW China: implication for Karstification in non-exposed limestone. Front. Earth Sci. 10, 842386.
Zhao, B., Li, R., 2022. Formation mechanism of bedding-parallel antitaxial fibrous veins in shale: a review. J. Struct. Geol. 161, 104653.
Zhao, B., Li, R., Wu, X., Qin, X., Zhao, D., Khaled, A., Liu, F., 2020. Petrography and isotopic geochemistry of bedding-parallel fibrous gypsum veins in the Neogene Qingshuiying Formation of the Ningnan Basin, North China: insights for growth model of antitaxial fibrous veins. J. Struct. Geol. 132, 103973.
Zhao, S.X., Xia, Z.Q., Li, H., Wang, G.X., Qiu, Z., Liu, S.J., Zhang, C.L., Li, B., Yin, M.X., Yang, L.C., 2025. Quantitative evaluation and main controlling factors of natural fractures in a shale reservoir: a case study of the deep shale of the Wufeng Formation-Longmaxi Formation in Luzhou. Acta Sedimentol. Sin. 43 (1), 212–225.
Zhao, X.F., Zhou, M.F., Gao, J.F., Li, X.C., Li, J.W., 2015. In situ Sr isotope analysis of apatite by LA-MC-ICPMS: constraints on the evolution of ore fluids of the Yinachang Fe-Cu-REE deposit, Southwest China. Mineral. Deposita 50, 871–884.
Zhou, Q.S., Liu, J.Y., Ma, B., Li, C., 2024. Pyrite characteristics in lacustrine shale and implications for organic matter enrichment and shale oil: a case study from the Triassic Yanchang Formation in the Ordos Basin, NW China. ACS Omega 9 (4), 4605–4620.
Zoback, M.D., 2010. Reservoir Geomechanics. Cambridge University Press.
Zoback, M.D., Kohli, A.H., 2019. Unconventional Reservoir Geomechanics. Cambridge University Press.
Zou, C., Zhang, G., Yang, Z., Tao, S., Hou, L., Zhu, R., Yuan, X., Ran, Q., Li, D., Wang, Z., 2013. Concepts, characteristics, potential and technology of unconventional hydrocarbons: on unconventional petroleum geology. Pet. Explor. Dev. 40 (4), 413–428.